THESIS FOR THE DEGREE OF DOCTOR OF PHILOSOPHY

# Electric Machine Control for Energy Efficient Electric Drive Systems

ANDREAS ANDERSSON


Department of Electrical Engineering
Division of Electric Power Engineering
CHALMERS UNIVERSITY OF TECHNOLOGY
Gothenburg, Sweden 2018

Electric Machine Control for Energy Efficient Electric Drive Systems
ANDREAS ANDERSSON
ISBN 978-91-7597-792-8

© ANDREAS ANDERSSON, 2018.

Doktorsavhandlingar vid Chalmers Tekniska Högskola
Ny serie nr. 4473
ISSN 0346-718X

Department of Electrical Engineering
Division of Electric Power Engineering
Chalmers University of Technology
SE–412 96 Göteborg
Sweden
Telephone +46 (0)31–772 1000

Chalmers Bibliotek, Reproservice
Gothenburg, Sweden 2018

Electric Machine Control for Energy Efficient Electric Drive Systems
ANDREAS ANDERSSON
Department of Electrical Engineering
Chalmers University of Technology

# Abstract

Over the past decade, electric vehicles has increasingly become an area of attention for both academia and industry, much due to challenges such as emissions legislation and the environmental impact of the transportation sector [1]. The absence of the broadband noise from the internal combustion engine brings new acoustic challenges for electric propulsion applications. Magnetic noise from electrical machines is of particular interest in automotive applications. It is not only related to the geometrical design of the machine, but also to the selection of control approach and voltage modulation strategy.

This thesis focuses primarily on software-based electric drive system energy efficiency enhancements, supported by extensive experimental testing, incorporating aspects of dynamic performance and acoustic perspectives. The scientific contribution can be summarized in three parts. Firstly, the interdisciplinary research where efficiency enhancements are coupled to acoustic performance. Secondly, the cause and effect of electromagnetic forces as the link between machine design, controls, and perceived acoustic annoyance. Lastly, the findings from the research on optimization-based inverter control and motion sensorless operation.

It is proven that alternative modulation techniques can reduce the inverter losses with up to 15% without degradation of the perceived acoustic annoyance. Moreover, research on finite control set model predictive current control and moving horizon rotor position estimation is presented. It is shown that the proposed solutions are feasible, and that the associated optimization problems at hand can be solved in real-time while exploiting their respective attractive properties. Furthermore, excellent performance is obtained in comparison to state of the art alternatives, at the expense of increased computational complexity.

**Index Terms:** Energy efficiency, modulation techniques, noise assessment, permanent magnet synchronous machine (PMSM), inverter control.

# Acknowledgements

First and foremost, I would like to thank Professor Torbjörn Thiringer, my academic supervisor, examiner and mentor, for his continuous and consistent support during the work, and for making me say what I mean and mean what I say. I would also like to thank Dr. Stefan Lundberg, my academic co-supervisor, for his time and contributions, especially with the extensive support with the experimental work. A special thanks goes to Dr. Jonn Lantz at Volvo Car Group, my industrial supervisor, for his time and support as well as the industrial contributions. The work was founded by Volvo Car Group and the Swedish Energy Agency, both are gratefully acknowledged for the financial support.

Many people, both at Volvo Cars and at Chalmers, have been involved to varying degrees and have by their support, knowledge and helpfulness influenced the work. I would like to thank them all, especially my colleagues at the Division of Electric Power Engineering at Chalmers and the In-house SW group at Volvo Cars.

Andreas Andersson
Gothenburg, Sweden
Autumn, 2018

# Contents

# Part I

# Introductory chapters

# Introduction

## 1.1 Problem background

Over the past decade, electric drives have increasingly become an area of attention for both academia and industry. A typical application is within the field of automotive applications for electric- and hybrid-electric vehicle propulsion. An application, primarily dominated by the permanent magnet synchronous machine (PMSM) [2], characterized by its high energy efficiency and high power- and torque density capabilities [3, 4].

Globally, the market trend for electric vehicles (EV) is strong, with an annual market growth rate of 40 % in 2016 and continuously above 50 % year-on-year from 2010-2015 [5]. Furthermore, as for the Nordic countries, with Norway as the global leader on EV market penetration, the total annual EV sales went up 57 % in 2017, accounting for a full EV market share of roughly 10 % [6]. Furthermore, policy support mechanisms, such as financial incentives and regulations, combined with stricter tailpipe emission requirements, aims to increase the EV market penetration further. Research is an essential tool for achieving cost reductions and performance improvements, to further accelerate this transition from fossil fuels to electricity [5].

The pursuit of more high-performing and more energy efficient electric powertrains, with high driveability and redundancy, demands an ever-increasing need for research and development within the fields of controls, electromagnetic design, and system-level optimization. It is vital to maintaining high energy efficiency, while continuously meet remaining system requirements, such as requirements on driveability and acoustic performance - Two key areas in the automotive industry.

Noise and vibrations from electric drives have increasingly become an area of attention as well. For EV applications, the absence of the broadband noise from the internal combustion engine brings new noise, vibration and harshness (NVH) challenges. Electromagnetic noise is in literature designated as one of the main contributors to noise, usually perceived as very annoying due to its tonal appearance [7]. Electromagnetic noise is of particular interest in the automotive industry, its appearance is not only related to the physical design of the machine but also to the selection of machine control approach and voltage modulation - Two areas thoroughly elaborated and investigated in this work.

High-frequency noise from the electric propulsion system, originating from the inverter switching, has previously been investigated. Some interesting findings are presented in [8, 9, 10, 11, 12]. Different modulation techniques and switching frequency randomization are frequently researched areas as well. Although, usually evaluated from an electrical perspective [13, 14, 15, 16, 17]. In [13] and [14], focusing on harmonic spreading and efficiency, different random PWM techniques are investigated, concluding a significant decrease in harmonic intensity and advocates benefits from an EMI perspective. Most often, harmonic spread of inverter output current, power spectral density, and energy efficiency are considered, while noise emissions often are disregarded. Consequently, application-based or interdisciplinary evaluations are seldom seen.

In summary, missing in literature is more comprehensive analyses where additional adverse effects are incorporated, above all energy efficiency enhancements' influence on NVH. In addition, an understanding of the cause of effect of NVH-related issues is needed to understand the interlinked phenomena completely. Both of these constitute significant parts of this work. Furthermore, increased computational power allows for more advanced control systems. In this work, apart from what has previously been mentioned, motor control and parameter estimation are investigated as well, based on the framework of model predictive control and moving horizon control.

## 1.2 Purpose of the thesis and contributions

The purpose of the work presented in this thesis is to enhance the research on the topic of electric machine design, controls, energy efficiency enhancements, and NVH. Energy saving measures have been previously researched, both in the context of energy efficiency improvements for inverters as well as for electrical

machines. However, as previously discussed, missing in literature are comprehensive analyses and investigations of adverse effects and relations which usually are of an interdisciplinary nature, such as inverter switching influence on vibrations and radiated sound. The main contributions of the work can be summarized as

- The work presented has contributed to reducing the knowledge gap concerning the influence of inverter modulation strategies on energy saving and acoustic pleasantness. Different modulation techniques and randomized switching frequency have been investigated focusing on inverter energy efficiency and acoustic noise. A wide range of acoustic listening tests were used to evaluate how the acoustic noise from different solutions were perceived, with the purpose of quantifying differences and statistically ensure the findings validity.

- A promising current control solution, based on the framework of model predictive control was derived and investigated, where the computational complexity was reduced extensively compared to similar solution found in literature. Apart from the computational requirement aspects, the assessment focuses on current reference tracking abilities, inverter efficiency, phase current total demand distortion and acoustic performance. The proposed solution was experimentally evaluated against a standard double PI field-oriented current controller with pulse width modulation. In summary, it was concluded that the proposed solution yields excellent tracking abilities, while inverter efficiency was improved without deterioration of neither the phase current harmonics nor the acoustic performance.

- A motion sensorless control was developed based on finite horizon model predictive control, to explore the possibilities of controlling the machine without the need to measure the rotor position. It was experimentally tested and evaluated against a well-known active flux-based estimator. It is shown that the proposed solution is feasible, that the associated dynamic optimization problem can be solved in real-time while exploiting the attractiveness of the approach to obtain highly accurate estimates. Moreover, the absence of d-axis flux in the proposed solution is considered a significant strength. Conclusively, it turns the proposed solution into a universal solution for any synchronous motor, regardless of whether a PM-, PM-assisted or reluctance motor is used, non-dependent on the presence of magnetic saliency.

- Analytical expressions for the spatial and the time frequency content of the airgap flux density and force density were derived and verified with finite

element analysis (FEA). The purpose of this was to increase the understanding and the knowledge of how electromagnetic forces arise. Moreover, the knowledge is essential to grasp the impact of machine control and voltage modulation on the generation of electromagnetic forces and NVH-issues related to electromagnetic noise. The work is to a large extent based on more generic work found in literature, for instance in [7] and references therein. Where the contributions are within the tailored solutions for the investigated machine topology, as well as its usage to analytically complete the work related to electromagnetic forces and acoustics.

- FEA and extensive experimental testing have been conducted for the purposes of verifying the theory, studying phenomena that are either too complex or uncertain to investigate numerically and to increase the scientific value of the findings. Additionally, the experimental testing fulfills an educational purpose.

## 1.3 Thesis outline

The thesis is divided into a set of introductory chapters, followed by 7 peer-reviewed publications. The introductory chapters aim to describe the work, methods and processes, including only main results. For more detailed analyses and further conclusions, as well as results, the interested reader is referred to the scientific papers presented at the end of the thesis.

In Chapter 2, the basis for the experimental testing is presented. The methodology used is presented along with technical descriptions of the equipment used. The investigated machine is described, and experimental testing is used to validate the FE-model.

Chapter 3 covers electric machine design and FE-modelling aspects. Sensitivity analyses to mesh size and time step resolution are given in the first part. The second part of the chapter describes the methodology used to perform voltage excited FEM-simulations with a switched voltage source.

Chapter 4, and Appendix A are assigned to electromagnetic forces in the machine. The spatial and temporal content of both airgap flux density and force density are explained and analytically expressed. Necessary theory to incorporate electromagnetic quantities with NVH-related issues is discussed.

In Chapter 5, different modulation techniques are investigated, primarily

from energy efficiency and acoustic perspectives. The perceived annoyance for different modulation techniques is investigated. Listening tests are presented completing the chain from energy efficiency enhancements to perceived acoustic sensation for persons subjected to the emitted noise from the machine. Lastly, in Chapter 6, the work associated with machine control and sensorless operation is presented.

## 1.4 List of publications

This thesis is based on the work contained in the following papers, referred to by Roman numerals in the text:

I. Andersson, A. Thiringer, T. *An analysis of inverter switching loss minimization based on discontinuous PWM for a salient-pole PMSM.* Published in *16th European Conference on Power Electronics and Applications* (EPE'14-ECCE Europe), August 26-28, 2014.

II. Andersson, A. Thiringer, T. *Inverter losses minimization using variable switching frequency based on multi-objective optimization.* Published in *International Conference on Electrical Machines (ICEM)*, September 2-5, 2014.

III. Andersson, A. Lennström, D. Nykänen, A. *Influence of inverter modulation strategy on electric drive efficiency and perceived sound quality.* Published 1 January 2016 in *IEEE Transactions on Transportation Electrification* (Volume: 2, Issue: 1).

IV. Andersson, A. Thiringer, T. *Electrical Machine Acoustic Noise Reduction Based on Rotor Surface Modifications.* Published in *IEEE Energy Conversion Congress and Exposition (ECCE)*, September 18-22, 2016.

V. Andersson, A. Thiringer, T. *Experimental Determination of Inverter Losses and Sound Consequences of Using DPWM in an HEV.* Published in *32nd IEEE Applied Power Electronics Conference and Exposition (APEC)*, March 26-30, 2017.

VI. Andersson, A. Thiringer, T. *Motion Sensorless IPMSM Control Using Linear Moving Horizon Estimation With Luenberger Observer State Feedback.* Published 8 January 2018 in *IEEE Transactions on Transportation Electrification* (Volume: PP, Issue: 99)

VII. Andersson, A. Thiringer, T. *Finite Control Set Model Predictive Current Control For An Automotive Permanent Magnet Synchronous Machine.* In review process for publication in *IEEE Transactions on Vehicular Technology.*

# Case setup

The work presented in this thesis is in its entirety based on one machine, and all experimental testing was conducted using the same experimental setup, both described in the first part of this chapter. In the second part, the 2D finite element model (FEM) used for FE-calculations is compared to experimental data for validation purposes. In this comparison, the dq-flux linkage maps where estimated based on measurements and compared to data from FE-calculations.

## 2.1 Experimental setup

An electrical rear axle drive (ERAD) unit was used in the experimental testing. The ERAD consists of a three-phase PMSM incorporated with a speed reducer, differential and clutch. The electric drive unit is presented in Fig. 2.1 and the units subsystems are illustrated in Fig. 2.2. In the center picture of Fig. 2.1, a cross section of the machine's 45 slotted stator is seen, also showing the connector interface for accessing the rotor position sensor and the end-windings' temperature sensors, the three-phase connector, and the surrounding cooling jacket. As shown in Fig. 2.2, a (thyristor controlled) DC-machine was used as brake on one of the output shafts, whereas the second shaft was locked in the machine bed.

The ERAD was mounted in a subframe which was rigidly attached to the machine bed. In the intended application, the subframe is mounted underneath the chassis of the vehicle. The attachment of the machine to the subframe was not altered and was therefore identical with the solution for the intended application - An important note, considering the acoustic investigations that have been done.

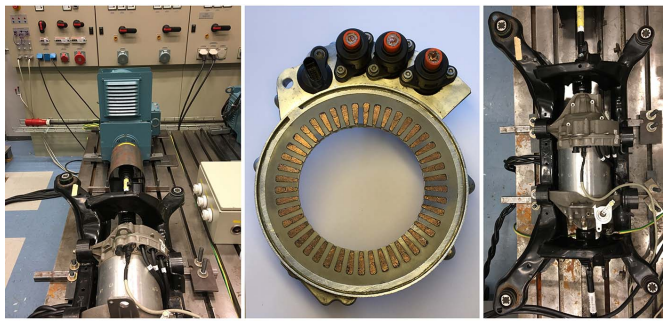

Figure 2.1: Picture of experimental setup (left and right) and cross section of the investigated machine (middle).

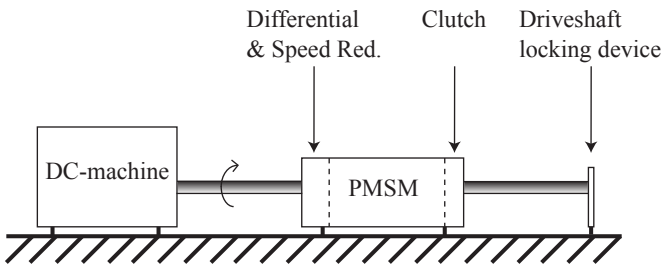


Figure 2.2: Illustration of the electrical rear axle drive unit installation

### 2.1.1 Inverter and electrical machine

A three-phase two-level inverter was constructed. It was fed by a 220 V DC voltage supply and controlled using a dSpace ds1006 real-time control system with a 2.8 GHz multi-core processor. The dSpace extension *AC Motor Control Solution* (DS5202 FPGA Base Board) was used with FPGA-based I/O. It was controlled via a real-time interface, allowing for complete access and control of the machine and the load at all times. The technical data of the PMSM and the IGBT-module is presented in Table 2.1. The geometrical data of the machine is obtained by measurements of the dismantled machine shown in the center of Fig. 2.1. This data is also the basis for the 2D FEM model.

A DC-link voltage of 220 V was used in the experimental testing, which is lower than in the intended application. The usage of a lower DC-link voltage was due to performance limitations of the brake-machine. Hence a reduction was necessary to obtain a sufficiently large field weakening region, and thereby enabling proper evaluations in field-weakening operation. During experimental testing, the

machine was operated up to 8000 r/min, with a peak output torque of roughly 60 Nm, with a base-speed of roughly 3700 r/min.

Table 2.1: Technical data for the PMSM and the IGBT module used in the experimental testing (SKM800GA125D)

| Variable | Value | Unit |
|---|---|---|
| Number of pole pairs | 5 | n |
| Number of slots | 45 | n |
| Number of parallel branches | 5 | n |
| Yoke outer radius | 90.0 | mm |
| Stator inner radius | 59.0 | mm |
| Rotor outer radius | 58.2 | mm |
| Airgap length | 0.8 | mm |
| Active length | 140 | mm |
| PM material coercivity[1] | 820 | kA/m |
| Iron material[2] | M270-35A | - |
| Winding type | Double layer | - |
| DC-voltage[3] | 220 | V |
| Peak phase current[3] | 150 | A |
| Base speed[4] | 3700 | r/min |
| Peak torque[4] | 61 | Nm |
| $E_{on}$ [5] | 88 | $mJ$ |
| $E_{off}$ [5] | 48 | $mJ$ |
| $E_{rr}$ [5] | 28 | $mJ$ |
| $R_{on,IGBT}$ | 3.83 | $m\Omega$ |
| $R_{on,diode}$ | 1.7 | $m\Omega$ |
| $V_{f,IGBT}$ | 1.7 | $V$ |
| $V_{f,diode}$ | 0.85 | $V$ |

[1] Tuned based on back-emf measurements
[2] Used in the FE-modelling
[3] Values used in this work
[4] With $V_{dc} = 220V$ and $i_{ph,peak} = 150A$
[5] @ 600V, 600A

### 2.1.2 Acoustic noise and vibration measurements

For the noise measurements, eight 0.5" microphones with a nominal sensitivity of 50 mV/Pa were evenly distributed in the space surrounding the machine, to obtain a robust global measure of the radiated sound around the PMSM drive. The distance between the surface of the electric drive unit to each of the microphones ensured avoidance of measuring in the acoustic near-field for the frequency range of interest, which is in the region from 0 Hz to roughly 16 kHz. For the vibrational measurements, nine 5-gram uniaxial accelerometers were glued, with a thin layer of cyanoacrylate to reduce the influence of the accelerometer-adhesive resonance, evenly along the axial center line on the upper arch of the cooling jacket of the stator. The placement of the microphones and accelerometers can be seen in Fig. 2.5. Further details about the acoustic setup is given in Paper III.

To reduce the impact of background noise, an acoustic box, seen in Fig. 2.3, with sides consisting of a 22 mm medium density fiberboard (MDF) in combination with 30 mm foam was constructed. A similar box was also constructed for the brake machine. As Fig. 2.4 reveals, the spectrum contains less noise up to about 10 kHz with the acoustic box applied. Note that the x-axis is in a logarithmic scale. Hence the orders are curved instead of straight as would have been the case with a linear x-axis.

Figure 2.3: Acoustic box made of 22 mm MDF for background noise reduction, positioned around the test object.

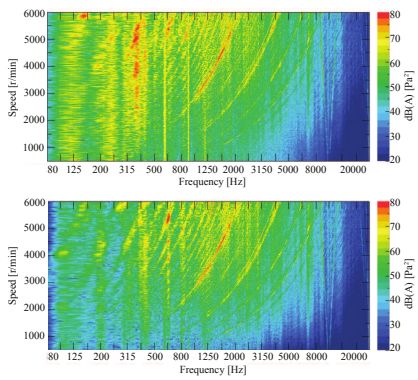


Figure 2.4: Autopower noise spectrum without (upper) and with (lower) acoustic box.

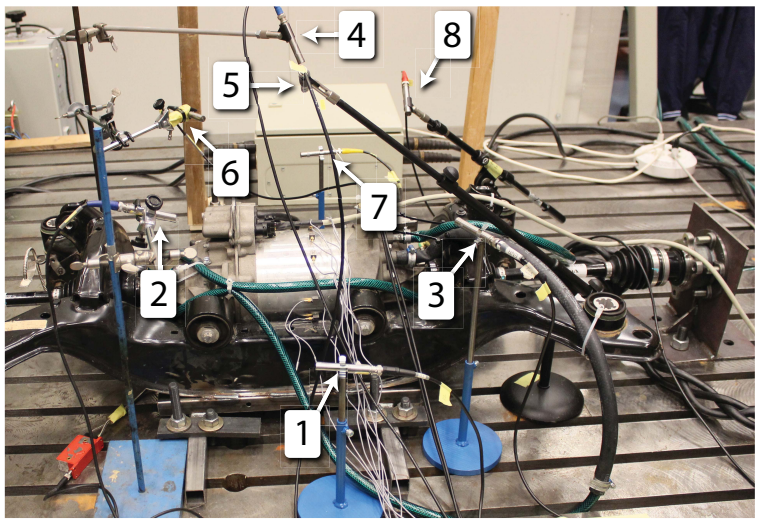


Figure 2.5: Experimental setup with PMSM and instrumentation for sound and vibration measurements. The PMSM is mounted in the subframe and attached to the load machine to the left.

### 2.1.3 Instrumentation

The instrumentation that was used in the experimental testing is presented in Table 2.2. A 40-channel data acquisition system was used primarily for the acquisition of noise and vibration data whereas the Lecroy oscilloscope with AP011 probes was used only for current measurements. Two different types of accelerometers were used. The uniaxial ones were mounted on the stator cooling jacket measuring radial accelerations, whereas the triaxial accelerometers were installed on the subframe to measure blocked forces.

### 2.1.4 Test procedures

Both steady state and transient analyses was done. Steady state analysis is suitable for data collection of electrical quantities, such as phase current, whereas transient analysis is suitable for noise and vibration measurements. During the transient studies, the rotational speed was swept from 500 to 7500 r/min over a period of 60 seconds. The data collection was done in parallel with separate analog to digital conversion for each of the 40 channels of the LMS Scadas acquisition system with a sampling frequency of 22 kHz.

Table 2.2: Instrumentation used in experimental testing

| Item | Instrument | Comment |
|---|---|---|
| 1 | LMS Scadas Mobile 40 channel acquisition system | Used for NVH measurements |
| 2 | Lecroy Wavesurfer 24MXs-B | Used for current measurements |
| 3 | 0.5 inch B&K G.R.A.S microphones | - |
| 4 | Uniaxial B&K 4507B accelerometers | Mounted on stator housing |
| 5 | Triaxial 4524B accelerometers | Mounted on subframe |
| 6 | Lecroy AP011 Current probe | Current measurement probe |
| 7 | Lecroy AP032 Differential probe | Voltage differential measurement probe |
| 8 | dSpace RTI1006 | Control system |
| 9 | Yokogawa WT3000 | Power Analyzer |

## 2.2 Validation of FEM-model

In this section, the FEM-model used is validated using experimental testing. A set of tests where undertaken to measure and validate

- Winding resistance
- Magnetic model
- Permanent magnets' field strength
- Thermal coefficients of stator windings and iron

Some of the items listed are not measurable on a system level, such as the magnets' field strength. Others are not possible to obtain in transient 2D electromagnetic FEM, such as the thermal coefficients. However, combined it provides an understanding of the machine and the accuracy of the FEM-model which results in a comprehensive understanding of the machine.

### 2.2.1 Validation of magnetic model

The objective of this validation is to estimate the dq-flux linkage and to compare these with the FEM results. The reason is two-fold. It is primarily motivated by the necessity of validating the 2D FEM-model, but it is also done for educational

purposes. Direct measurements of the output torque of the machine was unfeasible, due to imitations in the experimental setup. Hence only voltages and currents were used. Instead of measuring the (switched) three-phase voltage with a power analyzer, with potential problems of synchronizing measurements in time, the reference dq-voltages from the controller was used. Clearly, this approach is tainted with some uncertainties. Primarily the correctness of the magnitude due to voltage drops and other non-idealities in the inverter. However, previous to this evaluation, measurements and compensation of inverter non-idealities, such as the voltage drop across the power devices and the dead-time, where undertaken. In summary, the approach used to estimate the dq-flux linkage maps was based solely on the phase current measurement and the control system voltage references. The phase current measurements were expedited using the dSpace control system, ensuring a unified time stamping for all measurements.

The equivalent circuit model of a PMSM, and the modeling approach in the dq-reference frame is in detailed described in Section 6.1. Hence it is only briefly summarized here. The stator equations can be written as,

$$L_d \frac{di_d}{dt} = u_d - R_s i_d + \omega_e L_q i_q \tag{2.1}$$

$$L_q \frac{di_q}{dt} = u_q - R_s i_q - \omega_e \left( L_d i_d + \Psi_m \right) \tag{2.2}$$

and the dq-flux linkage can be expressed using the dq-inductances, currents and the PM flux constant, as

$$\Psi_d = L_d i_d + \Psi_m \tag{2.3}$$

$$\Psi_q = L_q i_q \tag{2.4}$$

At steady state, with current derivatives equals to zero, the stator equations (2.1) and (2.2) can be simplified as

$$u_d = R_s i_d - \omega_e L_q i_q = R_s i_d - \omega_e \Psi_q \tag{2.5}$$

$$u_q = R_s i_q + \omega_e \left( L_d i_d + \Psi_m \right) = R_s i_d + \omega_e \Psi_d \tag{2.6}$$

Given a pair of dq-currents and voltages, as well as the rotational speed of the machine, the dq-flux linkage can be obtained as,

$$\Psi_d = \frac{u_q - Rsi_q}{\omega_e} \tag{2.7}$$

$$\Psi_q = -\frac{u_d - Rsi_d}{\omega_e} \tag{2.8}$$

A sequence of motor-generator-motor operation was used to estimate the flux linkage at each operation point. The two motor operations were identical and aimed at cancelling temperature related phenomena, such as increased stator resistance as the machine is heated during load. The generator mode was run with the same current as for the motor mode, but with a reversed sign on the q-current. In Fig. 2.6, the time series of the dq-current and voltage are presented, and the trigger signal indicates where measurements were taken. Note that each measurement sequence is equivalent to an integer number of mechanical rotations to cancel non-idealities such as potential eccentricity and gearbox effects. Transients occurring from the change of operating point needs to settle before each measurement, hence the delay time from reaching the operating point to the start of the measurements.

Figure 2.7 shows the operating points evaluated. The numbers indicate the sequential order of the evaluation. Note that the sequence, which might appear random, is structured in sets of two. All 64 operating points were combined in sets of two, where the selection of pairs was based on keeping the cumulative RMS-current constant. This approach aims to maintain a constant RMS-current throughout all operating points and hence to minimize the temperature drift between the measurements. In Fig. 2.8, the RMS-current for each combination is shown. As can be seen, it was kept fairly constant between all combinations.

From each operating point measurement, three groups of measurements were obtained,

- $v_{d1}$, $v_{d2}$, $v_{d3}$, $v_{q1}$, $v_{q2}$, $v_{q3}$
- $i_{d1}$, $i_{d2}$, $i_{d3}$, $i_{q1}$, $i_{q2}$, $i_{q3}$
- $\omega_{e1}$, $\omega_{e2}$, $\omega_{e3}$

If the iron losses are neglected, which is a reasonable assumption if the machine was operated with low rotational speed, the dq-flux linkage is complex

conjugates between motor and generator operation, as

$$\Psi_{d1} = \Psi_{d2} = \Psi_{d3} \tag{2.9}$$

$$\Psi_{q1} = -\Psi_{q2} = \Psi_{q3} \tag{2.10}$$

and the mean flux linkage for the operating point can be computed as

$$\Psi_d = \frac{1}{2}\frac{v_{q2} + \frac{v_{q1}+v_{q3}}{2}}{\omega_e} \tag{2.11}$$

$$\Psi_q = \frac{1}{2}\frac{v_{d2} - \frac{v_{d1}+v_{d3}}{2}}{\omega_e} \tag{2.12}$$

where $\omega_e$ is the averaged value between the three measurements.

To further minimize problems with thermal drift during the measurement session, a machine warm-up procedure was undertaken prior to the measurements. A procedure aiming to bring the machine into a thermal steady state with the RMS-current applicable during the succeeding flux linkage measurements.

The approach used was to run the machine with a constant load, and every 25 seconds remove the load and do back-emf measurements. The back-emf measurements where then used to estimate the flux linkage constant $\Psi_m$. As the magnitude of the back-emf (and the flux linkage constant) stabilizes after a period of time, a thermal steady state was considered to have been reached. The stator winding temperature was measured directly with sensors in the end-windings of the machine.

In Fig. 2.9, the repeating sequence and time evolution of the dq-current and voltage are given for the warm-up sequence, as well as an indication of where the back-emf measurement and winding temperature measurement were done. In Fig. 2.14 and 2.15, the stator winding temperature and the estimated flux linkage constant are presented as functions of time, respectively. The data show the propagation for three different rotational speeds, where the higher speeds rise quicker in temperature. Naturally, higher rotational speeds induce more iron losses which would increase the temperature.

In Fig. 2.10 and 2.11 the dq-flux linkage maps obtained from the experiments are presented. In Fig. 2.12 and 2.13 the percentage difference are given with respect to data obtained from FEM, calculated as

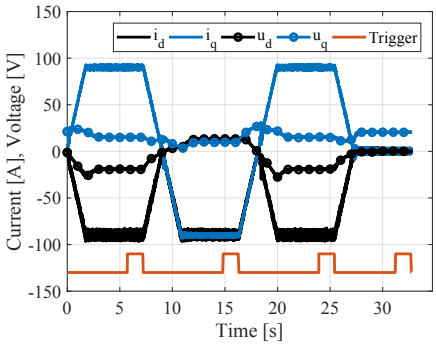


Figure 2.6: Measurement sequence for dq-flux estimation

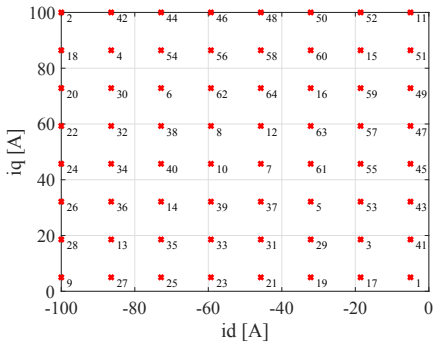


Figure 2.7: Mapping sequence of the different operating points

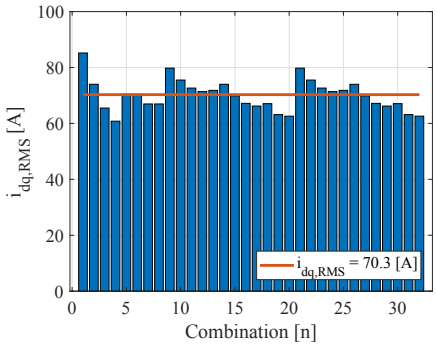


Figure 2.8: RMS current of the combinations of sequences shown in Fig. 2.7

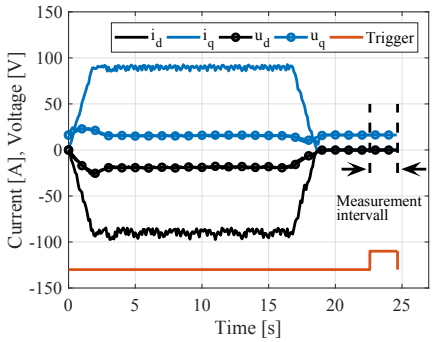


Figure 2.9: Machine warming sequence

$$\Delta\Psi = 100 \times \frac{\Psi_{est} - \Psi_{FEM}}{\Psi_{FEM}}. \tag{2.13}$$

As can be seen, the conformity is good. The most substantial differences occur for the d-axis flux linkage, where it increases with increased negative d-axis current. While for the q-axis flux, the error is consistently around 1-2 percent. As for the d-axis flux linkage, the field strength of the magnets can be tuned to obtain an increased correspondence. In summary, it is concluded that the approach is feasible, and that the conformity is sufficient to declare the FEM-model as valid.

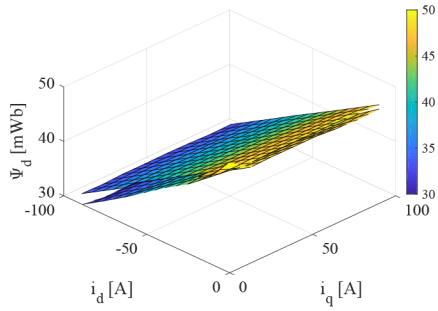


Figure 2.10: Estimated d-axis flux (lower) and d-axis flux obtained from FEM (upper)

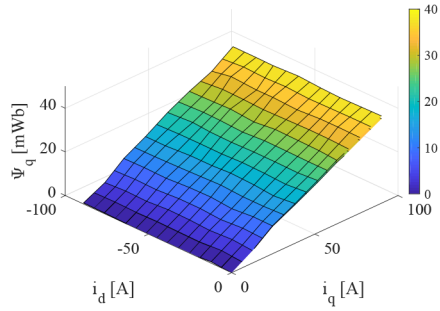


Figure 2.11: Estimated q-axis flux (lower) and q-axis flux obtained from FEM (upper)

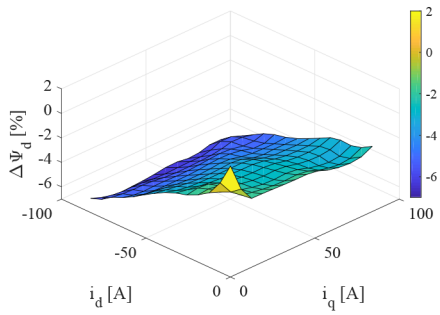


Figure 2.12: Difference in d-axis flux linkage between measurements and FEM, calculated using (2.13)

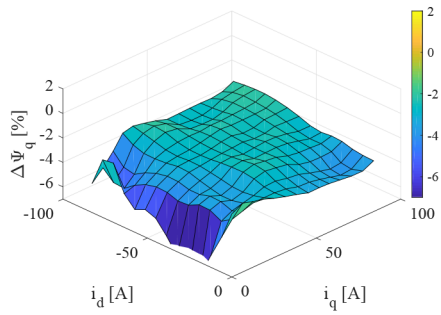


Figure 2.13: Difference in q-axis flux linkage between measurements and FEM, calculated using (2.13)

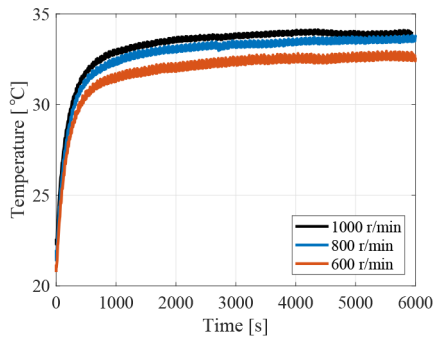


Figure 2.14: End winding temperature during machine warm-up procedure measured in the end-winding

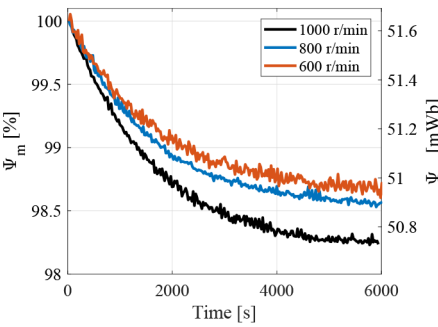


Figure 2.15: Permanent magnet flux linkage during machine warm-up procedure

# Electric Machine Design

## 3.1 Finite element modelling

Finite element modeling (FEM) is used to solve complex electromagnetic boundary value problems, i.e., problems defined by differential equations subjected to constraints. As a numerical method, the obtained solutions are approximate and to a certain level erroneous. Apart from material data, the discrepancy between measurements and calculations originates from both geometrical detailing and deviations, as well as from solver prerequisites, such as resolution in time and space [18].

It is of interest to evaluate the FE-model and the modeling approach to explore the level of model uncertainty and sensitivity. Primarily, to increase the modeling accuracy and to add confidence to the generated results. Evaluations of FEM-calculations is two-parted and can be summarized with one part covering the correctness of the geometrical model and material properties, and a second part comprising the discretization sensitivity. The former was covered in Section 2.2.1, where the magnetic model was validated with experimental testing, and the latter is covered in Section 3.2 of this chapter.

The sensitivity of the FEM-model, concerning the discretization, can be summarized as sensitivity towards resolution in time and space. Considerations that are of importance due to their significant impact on the computational time. Hence motivating the efforts of performing the analysis. That is to say, instead of consistently maximizing the computational time, by refining the mesh and the simulation time stepping. A more prominent engineering method would be to study each variable's influence and select a setup generating an accuracy

that is in line with what is required for the targeted investigation. Doing so, a sufficiently adequate result will be obtained while the simulation time is kept to a minimum. Combined, it is a motivator for the sensitivity analyses presented in this chapter. Note that this sensitivity analysis only reveals the uncertainties tied to the computational resolution, it does not remedy erroneous results due to the geometrical detailing of material data-imperfections.

To sum up, this chapter covers FEM specific discretization aspects. The finite element modeling is described, and the resolution is studied by the use of zero cell size extrapolation. Further, an approach to enable voltage excited finite element modeling is presented. The simulation software used is ANSYS with the engineering suite Maxwell.

## 3.2 2D model sensitivity anaysis

In this section, the sensitivity of mesh size and time step resolutions are investigated. The aim is to gain an understanding of how these resolutions affect the results and to motivate the selection used in the following analyses properly. A single operating point was used in the evaluation, with an RMS-current of 150 A and a rotational speed of 4800 r/min.

The first sensitivity analysis, covering the mesh resolution, is focused around the radial forces acting on the stator as well as the electromagnetic torque. The selection of the forces was due to the connection to the following acoustic analysis and the work presented in Paper III and IV. The second sensitivity analysis, covering the time step resolution, is focused on the induced voltage and the core losses, two parameters strongly linked to the time resolution.

The method used in the sensitivity analyses was zero cell size extrapolation, which is a method used to explore the characteristics of discretized models as if an infinite resolution was used. The benefits of zero cell size extrapolation can be described by considering the fictive case of performing a FEM-simulation with infinite mesh resolution, i.e., zero mesh cell size. With result from such a case, one could subsequently quantify deviations resulting from any finite mesh size and thereby quantifying modeling errors as a function of resolution. For obvious reasons, zero cell size results can only be achieved by extrapolation of results based on finite mesh-sized simulations. Equivalently, zero-time step results can be obtained by extrapolation of finite time step results. The extrapolation

methodology used is further presented in Section 3.2.1.

### 3.2.1 Extrapolation to zero cell size

The method used for extrapolation studies is to analytically describe a parameters dependency of either mesh cell size or time step size, using Taylor expansion. With the assumption that two terms in the expansion are sufficient to describe a variables dependency, the following analytical expression have been used

$$f(h_i) = f_0 + f_1 h_i^p \tag{3.1}$$

where $f(h_i)$ is the results based on the mesh size $h_i$, $f_1$ is a scaling factor and $p$ is the order of convergence. In this representation, $f_0$ equals the value at zero cell size. Hence the second term goes to zero as $h$ turns towards zero. If the assumed decomposition is not representative enough, it can be extended with more components to achieve a more accurate representation.

Based on a series of simulations with a uniform cell size relation, chosen according to,

$$\frac{h_i}{h_{i+1}} = \frac{h_{i+1}}{h_{i+2}} \tag{3.2}$$

where $h_i$, $h_{i+1}$ and $h_{i+2}$ are the cell sizes for simulation $i$, $i+1$ and $i+2$, the order of convergence can be estimated as

$$p = \frac{ln\left(\frac{I(h_i)-I(h_{i+1})}{I(h_{i+1})-I(h_{i+2})}\right)}{ln\left(\frac{h_i}{h_{i+1}}\right)} \tag{3.3}$$

where $I(h_i)$ is the outcome from the FEM-simulation and $h_i$ is the cell size of that simulation [18].

Using a simulation series of minimum three different cell sizes the unknown coefficients $f_0$ and $f_1$ can be calculated by defining the problem as

$$\begin{bmatrix} f(h_1) \\ f(h_2) \\ \vdots \\ f(h_n) \end{bmatrix} = \begin{bmatrix} 1 & h_1^p \\ 1 & h_2^p \\ \vdots & \vdots \\ 1 & h_n^p \end{bmatrix} \begin{bmatrix} f_0 \\ f_1 \end{bmatrix} \tag{3.4}$$

and solved for $[f_0 \ f_1]^T$ by matrix algebra using the pre-calculated convergence, according to (3.3). Note that it is not evident that convergence can be established based on the methodology presented. A prerequisite is that there exists a correlation to be explored. For instance, for a parameter that is not correlated with the variables that are investigated, it is implausible that a convergence can be established.

### 3.2.2 Sensitivity analysis of mesh element size resolution

The mesh element size analysis is focused on the elements in, and in the vicinity of, the airgap and the stator teeth tips. The remaining of the mesh is kept fixed throughout all cases. The mesh is shown in Fig. 3.1, where the refinement is seen from left to right. As can be seen, the mesh is identical for each of the three cases, except for the region in and around the airgap and the stator teeth tips - the area which is of consideration in this analysis.

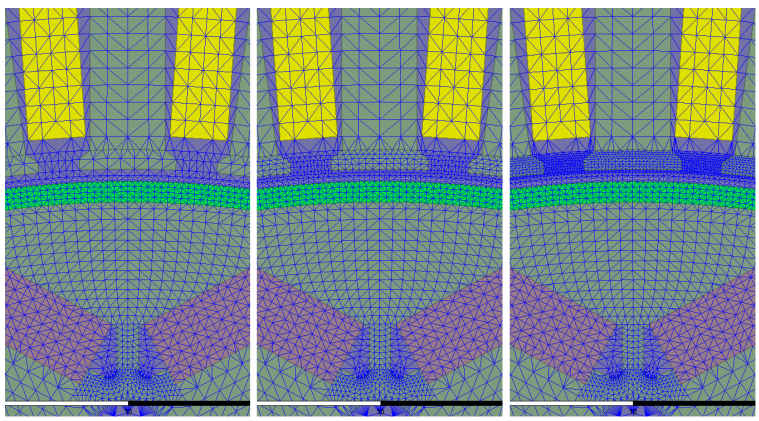

Figure 3.1: Comparison of the three mesh resolutions used in the analysis of the mesh size resolutions impact. The refinement occurs from left to right, where the rightmost figure shows the finest mesh resolution.

Figure 3.2 and 3.3 show the extrapolation of selections of the most essential harmonics in the airgap force density, and the fundamental component as well as harmonics in the electromagnetic torque, respectively. The circles indicate the results from the FEM-simulations and the dashed lines represents the extrapolation, based on the zero-cell size extrapolation method described in Section 3.2.1. The errors are given in percent, defined as

$$e(h) = 100 \times \frac{|x_0 - \hat{x}_0|}{x_0} \tag{3.5}$$

where $x_0$ is the final value of the extrapolation, denoted $f_0$ in (3.1), and $\hat{x}_0$ is the extrapolation as a function of $h$, denoted $f(h_i)$ in (3.1).

From the data, a few important conclusions can be drawn. Firstly, the harmonics presented are correlated with the mesh refinements undertaken. Secondly, the proposed Taylor expansion presented in (3.1) is sufficient to express their trajectory. Moreover, the error for all data shown in the two figures is within 2 percent for the three mesh refinement cases, which is considered small. To achieve significant improvements in absolute values, the additional mesh size refinements required would be substantial. To conclude, the coarsest of the three cases are considered refined enough to generate sufficiently adequate results.

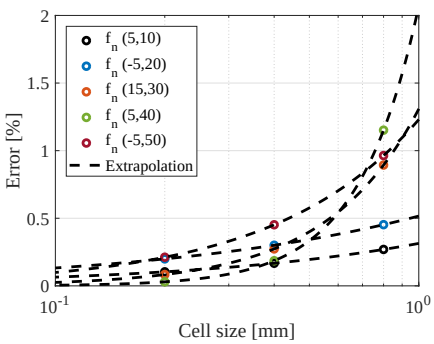


Figure 3.2: Extrapolation towards zero mesh cell size of a selection of the most significant airgap force density harmonics at 4800 r/min and rated torque.

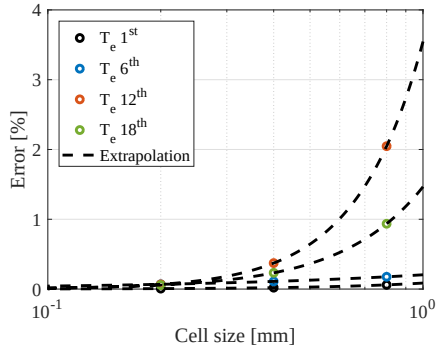


Figure 3.3: Extrapolation towards zero mesh cell size of the fundamental component and harmonics in the electromagnetic torque at 4800 r/min and rated torque.

### 3.2.3 Sensitivity analysis of time step resolution

For the time step sensitivity analysis, four cases were studied. The step sizes selected are given in Table 3.1, all in conjunction with the interrelations presented in (3.2). *Samples per electric period* is based on a rotational speed of 4800 r/min, corresponding to a fundamental frequency of 400 Hz.

In Fig. 3.4 and 3.5 the extrapolations related to the induced voltage and the core losses are given, respectively. As can be seen, the fundamental component

Table 3.1: Time step sizes used for the zero time step size analysis

| Case | Time step [$\mu$s] | Samples per electric period [$n$] |
|---|---|---|
| 1 | 12.5 | 20 |
| 2 | 6.25 | 40 |
| 3 | 3.125 | 80 |
| 4 | 1.5625 | 160 |

of the induced voltage is correctly observed even for large step sizes. However, the harmonics are subjected to substantial errors as the time resolution coarsened, both considering the induced voltage as well as the losses. Hence the time step resolution should be considered in analyzes incorporating those results.

Considering the induced voltage, this might seem contradictory to the Nyquist sampling theorem. However, since the induced voltage is derived using the backward Euler derivative discretization method, it is evident that the time resolution has an impact on the result. It does affect not only the magnitude but also the phase. As for the core losses, which is based on the Bertotti equation, similar reasoning can conclude the drastic underestimation that occurs as the time resolution is too coarse. Since the losses are based, cumulatively, on contributions from each of the harmonics in the magnetic field, the sum depends on the underlying frequency data. The errors in both the induced voltage as well as the losses are substantial for the coarsest time step used in the analysis. The time resolution used in this work never exceeds the second to the largest seen in this evaluation.

## 3.3 Voltage excited FE-modelling

A methodology, enabling switched voltage source fed FEM-simulations, is developed to investigate high-frequency harmonics in the airgap flux density and force density originating from the pulse width modulation. The objective is to investigate different modulation techniques influence and to verify differences in vibrations and radiated noise from the experimental testing. Typically, computational time restricts transient FEM analyses to cover only a few electrical periods in time. Minor errors in the initialization of such a simulation is likely to cause offsets that are unlikely to decay during the simulation time. Consequently, a method to overcome the issue with initialization errors in voltage excited FEM-simulations is needed. In principle, the method is based on a series of four simulations where

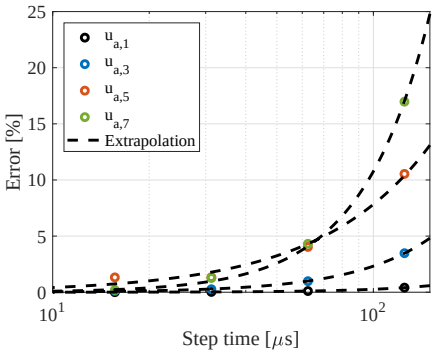


Figure 3.4: Extrapolation towards zero time step size of the fundamental component and harmonics of the induced voltage at 4800 r/min and rated torque.

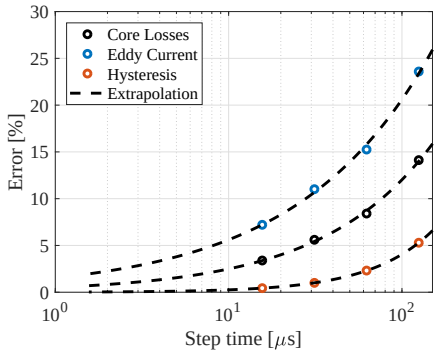


Figure 3.5: Extrapolation towards zero time step size of core losses at 4800 r/min and rated torque.

the relatively long settling time of transients, occurring due to initialization errors, is taken advantage of for detection and compensation.

In the case of voltage excited FEM-calculations, the initialization is a critical part. Hence a couple of items needs to be addressed to obtain adequate results. The items of high importance are:

1. Derivation of the induced voltage
2. Derivation of stator winding resistance and its usage
3. Elimination of initialization error in the phase current.

These three parts are described in the same order in the following sections. The PWM is implemented by deriving the switching patterns offline, and the FEM-simulations are executed in an open-loop fashion. Alternatively, a co-simulation with for instance ANSYS Simplorer can be used.

### 3.3.1 Derivation of induced voltage

The induced voltage is needed when defining the voltage vectors to be applied in the voltage excited simulations. The applied voltage for phase A can be expressed as

$$u_a = R_s i_a + \frac{d\Psi_a}{dt} \tag{3.6}$$

where the derivative of the flux linkage equals the induced voltage [19]. Accordingly, the data obtained from the sinusoidally current excited FEM-simulation is the phase currents and the flux linkage, or the induced voltage. The time derivative definition used by ANSYS Maxwell is the s.c. backward stepping [20], defined as

$$\frac{dx^{k+1}}{dt} = \frac{x^{k+1} - x^k}{\Delta t}. \tag{3.7}$$

Deriving the induced voltage with this definition introduces a phase error in the induced voltage, supplied by the FEM-program, that is proportional to the time step size. The phase error in electrical degrees can be expressed as

$$\tilde{\theta} = 180\frac{\Delta t}{t_0} \tag{3.8}$$

where $\Delta t$ is the time step size and $t_0$ is the inverse of the fundamental frequency. Whether or not the induced voltage supplied by Maxwell is used, or if it is manually derived from the flux linkage, one should compensate for the phase error introduced by the derivative function for more accurate phase information.

Because of the use of the backward stepping time derivative function, the initial induced voltage values in the FEM-calculation will be zero. Without further consideration, the phase current derivatives between the first simulation time ($t = 0$) and the second ($t = \Delta t$) will be erroneous. In effect, the phase current will be subjected to an error. This can be explained by the stator equation, expressing the dynamics in the voltage and current as

$$\Delta t \begin{bmatrix} u_a - e_a \\ u_b - e_b \\ u_c - e_c \end{bmatrix} = \begin{bmatrix} L_{aa} & L_{ab} & L_{ac} \\ L_{ba} & L_{bb} & L_{bc} \\ L_{ca} & L_{cb} & L_{cc} \end{bmatrix} \begin{bmatrix} \Delta i_a \\ \Delta i_b \\ \Delta i_c \end{bmatrix} + R_s \begin{bmatrix} i_a \\ i_b \\ i_c \end{bmatrix} \tag{3.9}$$

or, equivalently

$$\begin{bmatrix} \Delta i_a \\ \Delta i_b \\ \Delta i_c \end{bmatrix} = \begin{bmatrix} L_{aa} & L_{ab} & L_{ac} \\ L_{ba} & L_{bb} & L_{bc} \\ L_{ca} & L_{cb} & L_{cc} \end{bmatrix}^{-1} \left( \Delta t \begin{bmatrix} u_a - e_a \\ u_b - e_b \\ u_c - e_c \end{bmatrix} - R_s \begin{bmatrix} i_a \\ i_b \\ i_c \end{bmatrix} \right). \tag{3.10}$$

As can be seen in (3.10), if the induced voltage at time step $t = 0$ is zero, the current derivatives will be severely enlarged. The result from this is phase currents that are erroneous in magnitude and possibly phase shifted. Either or, the airgap flux distribution will also be erroneous with consequences such as incorrect electromagnetic torque production.

Both issues with the phase shift due to time derivatives and due to zero induced voltage at the initial sampling point are linearly proportional to the sampling time step. Consequently, the error introduced by both is decreased with a decreased sampling time step. However, an understanding of the issue and the use of suitable counter actions are more time efficient than decreasing the sampling time.

### 3.3.2 Stator winding resistance handling

The stator winding resistance is derived based on the copper losses as

$$R_s = \frac{P_{cu}}{3i_{rms}^2}. \tag{3.11}$$

For the voltage excited simulations, the resistive losses are not calculated as in the current excited simulations. The $i^2 \times R_s$ method is used, instead of integrating the current density and using the conductivity of the material. Consequently, the value of the stator winding resistance should be applied in the simulation settings to achieve power loss balance when using voltage excitation.

### 3.3.3 Initial settings for AC-current

When the simulations with different excitation are to be compared it is vital that the fundamental components are comparable in magnitude and phase. If not, the simulations represent different operational points and a comparison would not be representative. When selecting initialization values for the phase currents in voltage excited simulations, it is reasonable to base these values on the fundamental component of the current. However, due to harmonics, the fundamental values are unlikely to be an option that is correct in the sense that no transient behavior arise. The correct values to be used as initial values for the phase current can be obtained in different ways.

One option is to make use of the fact that the transients have a long settling time. If the fundamental current component is used as initialization, one can then study the outcome of this (transient) simulation. The unwanted transient component in the current can be detected using Fourier analysis, and a correction term can be added to the initialization to cancel it out. A drawback is that two simulations are required - One simulation is required to detect the transients that are to be canceled and one simulation, using the correction obtained from the first simulation, is required to obtain the actual results. Yet, this solution is proposed due to its inherent simplicity and satisfying results.

### 3.3.4 Proposed simulation sequence in ANSYS Maxwell

The proposed simulation sequence used in this work can be seen in Table 3.2 and described more in detail in the following subsections. In all of the four steps, two electrical periods are simulated.

Table 3.2: Simulation sequence used in ANSYS Maxwell

| Simulation step | Description |
|---|---|
| 1 | Current excitation (Sine) |
| 2 | Voltage excitation (Sine) |
| 3 | Voltage excitation (SPWM or DPWM) |
| 4* | Voltage excitation (SPWM or DPWM, corrected) |

* Correction is based on FEM-calculations of simulation # 3.

#### Step 1

Initially, a sinusoidal current excited simulation is performed at the operational point of interest. The phase current, flux linkage, rotor position and copper losses are extracted and used further on.

#### Step 2

Based on the data obtained from step 1, the first of the voltage excitation-based simulations is defined. The magnitude of the fundamental component of the induced voltage is used, as well as the added resistive voltage drop, to determine

the voltage references. The phase error due to the time derivative of the flux linkage is compensated for, as previously discussed in Section 3.3.1. The phase current from step 1 is used to determine the initial phase current values required in this step. Note that in this step the voltage excitation is not switched but purely sinusoidal.

In Fig. 3.6 the induced voltage is presented for sinusoidal current and voltage excitation (step 1 and 2). As can be seen, the induced voltage for neither of the cases is sinusoidal. The harmonics are partly due to space harmonics in the permeance as consequence of the variations in the airgap reluctance and the distribution of the windings in the stator. Accordingly, using only the fundamental component (as in this case) the initialization will most likely be erroneous with transients in the current and torque as a result. However, this is taken advantage of and compensated for in step 4.

**Step 3**

From the previous simulation, the phase current, rotor position, and flux linkage are used to define a new set of sinusoidal phase voltage reference vectors. This new set of sinusoidal references is modulated with a triangular wave to obtain the PWM patterns used in this step, being the first step with PWM input. The transients from step 2, which do not decay during the two electrical periods, will naturally be seen in the outcome of this step too - Which is why the fourth step is required.

**Step 4**

Lastly, the obtained phase current, rotor position and flux linkage from step 3 are used to once again defining a new set of phase voltages to be applied. The new set of references is once again modulated with a triangular wave to obtain the PWM vectors used in this step. Additionally, the phase currents from step 3 are studied in the dq-reference frame and harmonics of interest are simply removed, by decomposing the data into its frequency components. From the adjusted phase currents (with unwanted harmonics removed) the very last samples are extracted and used as initialization values in this fourth simulation. Note that a prerequisite for this to work is that the harmonics do not decay in step 3. However, if they do, the third step only needs to be extended with an additional electrical period to obtain satisfying results.

In Fig. 3.7 the results of the initial current correction in this step can be seen. The data that is without correction is from step 3, and the data with correction is from this step, step 4. In the case without correction, one can see a slowly varying component with a frequency equal to the fundamental frequency.

In all the cases studied in this work, only the fundamental frequency has been removed from the dq-current. Furthermore, in Fig. 3.8 and 3.9 the electromagnetic torque is presented with and without this correction. A fundamental frequency component can be seen in the non-compensated cases (step 3), which is due to the error in phase current initialization.

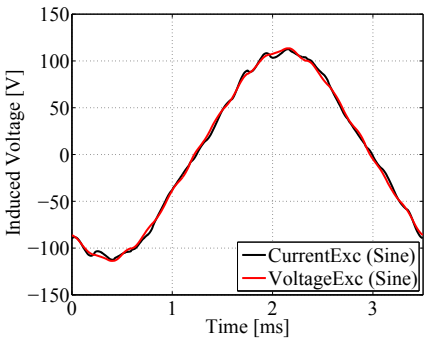


Figure 3.6: Comparison of induced voltage for phase A for sinusoidal current and voltage excitation. The x-axis corresponds to one electrical period.

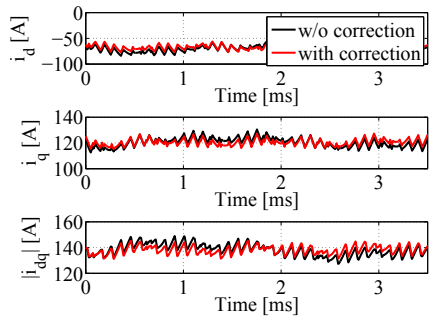


Figure 3.7: Comparison of dq-current between FEM-calculations with and without initial current value correction (step 3 in Table 3.2) for DPWM. The x-axis corresponds to one electrical period.

**Remarks**

The reason for the intermediate step (step 2) is to guarantee steady state in the operational point of interest. When step 2 is neglected, occasionally the initialization is too corrupted generating data that are beyond correction possibilities in the fourth step.

The simulation setup in ANSYS Maxwell is partly tabulated in Table 3.3. Note that the simulation time is not fixed when PWM is used. An underlying time step size of 2 $\mu s$ is used. However, whenever a switching of one of the phases occurs, two additional calculations are performed in the vicinity of the switching

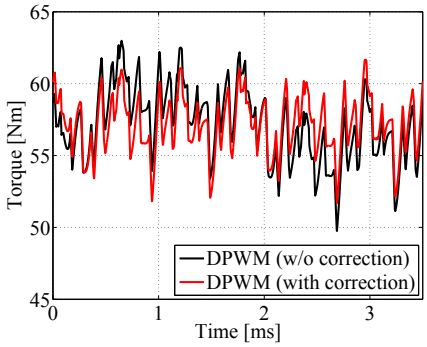


Figure 3.8: Electromagnetic torque over one electrical period visualizing the effects of the initial current correction for DPWM voltage excitation.

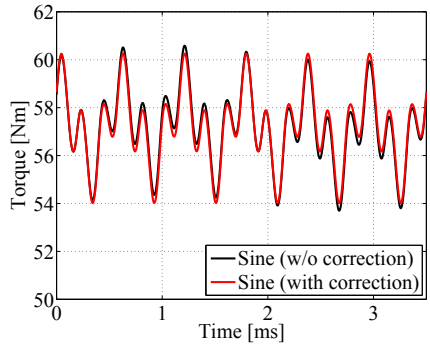


Figure 3.9: Electromagnetic torque over one electrical period visualizing the effects of the initial current correction for sinusoidal voltage excitation.

event. This is used to increase the accuracy and suppress errors that are due to a sparse simulation time stepping. Practically, this is done by controlling the time stepping in the simulation. An alternative solution would have been to use a fixed, but very refined, time step. However, such a case would require far more computational time.

Additionally, the simulation time and rotational speed of the machine are defined to coincide in an odd number of switching periods per fundamental period, to eliminate subharmonics in the phase current due to asynchronous PWM [21].

Table 3.3: ANSYS Maxwell Simulation Setup

| Parameter | Value | Unit |
|---|---|---|
| $f_0$ | $0.0035^{-1}$ | $Hz$ |
| $T_{start}$ | 0 | $\mu s$ |
| $T_{step}$* | 2 | $\mu s$ |
| $T_{step,2}$** | 10 | $ns$ |
| $T_{stop}$ | 7000 | $\mu s$ |
| Mesh nodes | 52738 | - |

* Smaller time steps are taken in the vicinity of the switching events.

** Time step used in the vicinity of switching events.

This method has been used in Paper III and V, to calculate losses in the machine using voltage excitation (both sinusoidal and PWM). As discussed in Paper III, an eddy current loss increase in the range of 50-75 % was obtained for different operating points, when the excitation was changed from sinusoidal current-based to voltage-based. As the voltage was modulated, only minor differences were seen compared to sinusoidal voltage excitation. To conclude, the voltage excitation generates higher losses, which is further discussed in Paper III.

# Electromagnetic forces and e-machine acoustic noise

Over the past decade, noise and vibrations from electric drives have increasingly become areas of attention for both academia and industry. The absence of the broadband noise from the internal combustion engine brings new noise, vibration and harshness (NVH) challenge for hybrid/electric vehicle applications.

Noise and vibrations from an electrical drive unit can be categorized based on origin as either electromagnetic, mechanic or aerodynamic. Mechanical noise arises due to mechanical interaction in for example bearings and speed reducers whereas aerodynamic noise is a result of air flow due to mechanical movement [7]. Electromagnetic noise from electrical machines is of particular interest in automotive applications and focused upon in this thesis. It is not only related to the geometrical design of the electrical machine, but also to the choice of control approach and voltage modulation strategy, which is discussed more in detail in Paper III and IV.

The forces acting on the stator can be decomposed into airgap forces and magnetostrictive forces. Magnetostrictive force is caused by the magnetic fields ability to stress the iron in the field direction and thereby cause the mechanical structure to deform. Radial and tangential airgap forces are orthogonal to each other and can be explained as attraction and repulsion between the stator and rotor in radial and tangential direction, respectively [22].

Furthermore, the radial component of the air gap forces can be viewed as a byproduct due to lack of contribution to the rotational movement, which is solely a result of the tangential force component. However, radial forces can contribute

significantly to mechanical displacements of the stator yoke which results in emitted noise due to vibrations. Additionally, the tangential component acting on the stator teeth tips creates bending in the stator teeth causing local deformation influencing the over-all stator deformation. Besides the electromagnetic noise, primarily mechanical noise is a significant contributor to the total noise from the drive unit. However, in this work, only electromagnetic noise is covered.

The relation between airgap flux density and force density can be expressed with Maxwell's stress tensor as

$$f_n = \frac{1}{2\mu_0}\left(B_n^2 - B_t^2\right) \tag{4.1}$$

$$f_t = \frac{1}{\mu_0}\left(B_n B_t\right) \tag{4.2}$$

where $f_n$, $f_t$, $B_n$, $B_t$ and $\mu_0$ are radial and tangential force densities, radial and tangential flux densities and absolute permeability, respectively [23, 24, 25, 26]. From the tangential force, the electromagnetic torque can be estimated as

$$T_e = \oint_S \overrightarrow{r} \times \overrightarrow{f_t}\, dS \tag{4.3}$$

In Fig. 4.1, a comparison is given between the electromagnetic torque obtain directly from the FEM-program and the estimated torque based on (4.2). As can be seen, the data correlates well.

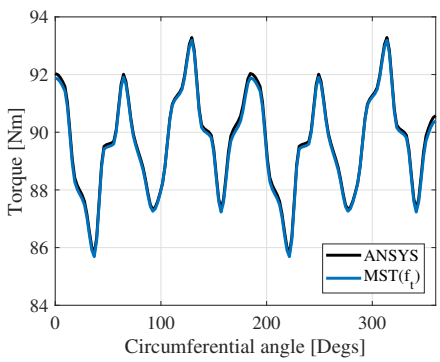


Figure 4.1: Comparison of electromagnetic torque calculation form ANSYS Maxwell and the estimate based on the surface integral of the tangential force obtained from the Maxwell Stress Tensor calculation from (4.2).

In relation to electromagnetic force calculations, and subsequent multi-physical structural and acoustic calculations, there is a number of interesting and important aspects to consider. As discussed by Chang et. al [25] and Zhu et. al [26], the Maxwell Stress Tensor method is a commonly used, and straightforward method of calculating the forces. However, local errors due to coarseness in the model discretization and selection of integration contour are areas of concern.

## 4.1 Coupled multi-physics simulations in ANSYS

The ANSYS Workbench platform was used to perform coupled multiphysics simulations. The problem at hand was divided into the three domains of electromagnetics, structural mechanics, and acoustics.

From the 2D electromagnetic solution, the force densities acting on the tips of the stator teeth was obtained as lumped forces for each tooth. In the second step, these forces were mapped onto the structural mesh of the teeth surface facing the rotor, feeding the structural response analysis of the stator. At this stage, the velocity of the yoke deformation is obtained over the outer surface and fed to the acoustic domain. In the acoustic domain, the yoke surface velocity was mapped onto its equivalent surface driving the acoustic harmonics analysis of a sphere surrounding the machine. This process is illustrated in Fig. 4.2.

The solution approach used was to sequentially solve the coupled problem one domain at the time, using a weak coupling without feedback between the different domains. The weak coupling is assumed to be sufficiently accurate, motivated by the relatively small stator deformations in relation to the airgap size. In the following investigations, the deformations of the stator are in the micrometer range, which is about 2-3 orders of magnitude less than the airgap size. A significant mesh refinement would be required in the 2D electromagnetic solver to catch the influence of such small deformations. Hence these are neglected.

As one can expect, the material properties are of high importance in the structural analysis part. The stator laminations are represented using Young's modulus, Poisson's ratio and the density of the material, given in Table 4.1. The Young's modulus, also known as Elastic modulus measured in pressure [Pa], is the ratio between stress and strain. The Poisson's ratio is used to define material behavior when exposed to stress - If an object is compressed in one dimension, it tends to expand in other dimensions, which is quantified by the Poisson's ratio.

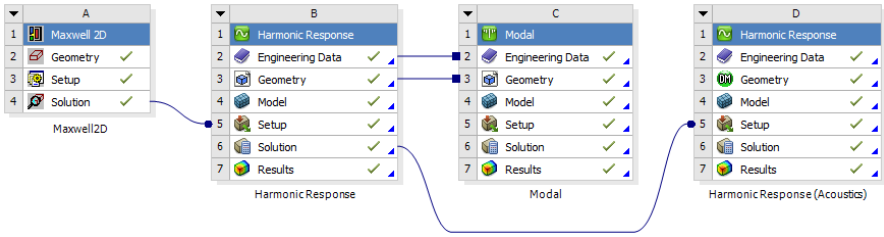


Figure 4.2: Illustration of the sequentially solved problem setup in ANSYS workbench.

Table 4.1: Material properties for stator laminates

| Variable | Value | Unit |
|---|---|---|
| Young's Modulus | $1.85 \times 10^5$ | $[MPa]$ |
| Poisson's ratio | 0.3 | $[-]$ |
| Density | 7650 | $[kg/m^3]$ |

## 4.2 Analysis of airgap flux density and electromagnetic forces

This section aim to describing the appearance of airgap flux and forces acting on the stator teeth. In Appendix A, the mathematical details are elaborated. Hence in the following sections, only abbreviated versions are given.

### 4.2.1 Appearance of airgap flux density

The magnetic field appearing in the airgap can be categorized based on its origin. By superposition, the airgap flux density can be decomposed into origin from armature and PM (rotor). In the remaining of this section, the analytical expressions for the airgap flux density are presented and the influence of the stator slots are discussed.

#### Rotor generated flux contribution

The radial component of the rotor flux, originating from the permanent magnets, can be expressed as [7, 27, 28],

$$B_{n,m} = \sum_{u=2k-1} B_{m,u} cos\left(up\omega t - up\theta\right) \tag{4.4}$$

where $k = 1, 2, 3...$, $p$ is the pole-pair number, $\omega t$ is the mechanical frequency, and $\theta$ is the mechanical circumferential angle stretching along the airgap. The subscript $n$ indicates the normal direction and the subscript $m$ indicates origin from permanent magnets. As shown in (4.4) the harmonic content of the rotor harmonics consists of pure circumferential orders, indicated by the same orders of both frequency and mode number [7, 27]. Note that all harmonics rotate synchronously with the rotational speed of the machine due to the inherent synchronicity in the machine, which would not be the case for an induction machine.

In Fig. 4.3 the radial flux density is presented during no-load operation. In the y-direction, marked *Position* ($\omega t$), the time dependency can be seen. In the x-direction, marked *Position* ($\theta$), the space dependency can be seen. In Fig. 4.4 the corresponding 2D-FFT of the time and space domain data is presented in a frequency/wave-diagram. Space and time dependencies are described with mechanical references by the x-axis and the y-axis, respectively. Each of the harmonics consists of a vibrational/circumferential mode that rotates with a certain frequency. As previously described, and explained by (4.4), the harmonics are synchronous with the rotational speed of the machine. This can be seen as the harmonics on the diagonal passing through circumferential order n=0. The data is presented with logarithmic z-axis to illustrate the harmonic content clearly. As can be seen, there are some outliers at vibrational orders $-50$ and 40 which is not represented in (4.4), caused by the slotting of the stator. The influence of the stator slots is further discussed in Section 4.2.1.

**Stator generated flux contribution**

Consider an ideal stator with a three-phase winding where the phases are evenly distributed, spatially shifted by $\pm 120$ electrical degrees, distributed in a fictitious manner without slots nor discrete winding distribution. Exciting this fictive three-phase winding with a fixed (non-varying) three-phase current, the resulting flux-density at any time instance being observed in the airgap along the span of the stator can be expressed as

$$B_{n,s} \propto cos\left(p\theta\right) \tag{4.5}$$

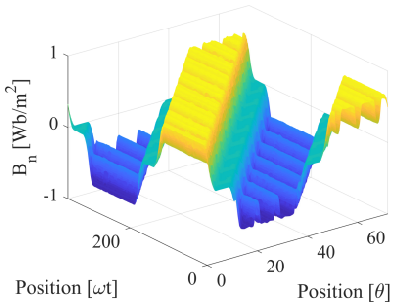


Figure 4.3: Radial airgap flux density as a function of both time ($\omega t$) and space ($\theta$) during no-load operation.

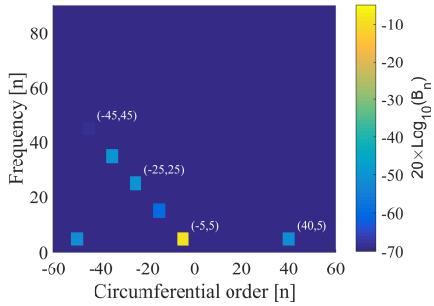


Figure 4.4: Frequency and mode number of the radial airgap flux density during no-load operation, derived by 2D-FFT and normalized with the number of pole-pairs.

where $B_{n,s}$ is the armature flux density in the radial direction where the subscript $s$ indicated the origin from the stator excitation, $p$ is the pole-pair number, and $\theta$ is the mechanical circumferential angle. Clearly, at any time instance, the flux would appear sinusoidal in space. If the stator excitation is changed to a sinusoidally varying current with electrical frequency $p\omega t$, the flux density can instead be studied as a function of time at a single point, geometrically, where it now would appear sinusoidal too. This can be seen by studying Fig. 4.3. At the geometric position $\theta = 0$, the fundamental frequency component of the flux density can be seen propagating along the axis marked *Position ($\omega t$)*. Likewise, at time instance $\omega t$=0, one can see the propagation in space along the axis marked *Position ($\theta$)* where the fundamental component is clearly seen. Considering only the fundamental component, this can mathematically be expressed as

$$B_{ns} \propto cos(p\omega t)cos(p\theta) = \frac{1}{2}\left[cos\left(p\omega t - p\theta\right) + cos\left(p\omega t + p\theta\right)\right] \tag{4.6}$$

using the trigonometric identity $cos(\alpha)cos(\beta) = 0.5\left[cos(\alpha - \beta) + cos(\alpha + \beta)\right]$. The first term on the right hand side of (4.6) rotates backwards whereas the second term rotates forward, visualizing the concept of backward and forward rotating fields [19]. As can be seen, the flux propagates both in space and time.

With analogy to circuit theory, the magnetic flux follows the path of least reluctance, where reluctance is similar to resistance in an electric circuit. As the reluctance in the airgap by far exceeds the reluctance in the iron material, the

intensity of the magnetic field in the airgap is very high. The armature excitation and the flux density can be linked by Hopkinson's law, where reluctance equals the magnetomotive force divided by the flux. Consequently, the flux density is proportional to the magnetomotive force divided with the airgap reluctance. When currents flow in the stator windings, a magnetomotive force (MMF) arise in the airgap, expressed in ampere-turns. With the use of MMF, the armature excitation and the flux can be linked as

$$B(\theta, t) = \mathcal{F}(\theta, t)\Lambda(\theta). \tag{4.7}$$

Focusing only on the harmonic content, the following MMF waves originating from the three phases are obtained at a given time

$$\mathcal{F}_{s,a} \propto \sum_{v=1,3,5,\ldots} i_a cos\left(vp\theta\right) \tag{4.8}$$

$$\mathcal{F}_{s,b} \propto \sum_{v=1,3,5,\ldots} i_b cos\left[vp\left(\theta - \frac{2\pi}{3}\right)\right] \tag{4.9}$$

$$\mathcal{F}_{s,c} \propto \sum_{v=1,3,5,\ldots} i_c cos\left[vp\left(\theta - \frac{4\pi}{3}\right)\right] \tag{4.10}$$

where $i_a$, $i_b$ and $i_c$ are the momentary phase currents in the given time instance. The amplitude of the MMF depends on various scaling factors defined by the machine design such as the number of turns in the stator, distribution factor, etc.

Spatially, the MMF wave produced by each winding is of a square wave characteristic hence the appearance of only odd harmonics. The appearance of a square wave is due to the discretization which is a result of the winding distribution and the stator slots. This is seen in Fig. 4.3. Multi-layer winding configurations can be used to smoothen the characteristics, which will change the magnitude of spatial harmonics. Note that the third harmonic is spatially in phase for all three phases and will not be present when the three phases are summed up, due to the three-phase symmetry in the machine.

Adding the influence of time to the magnetomotive force of the three phases, the following expression is obtained

$$\mathcal{F}_{s,a} \propto \sum_{v=1,3,5,...} cos\left(p\omega t\right) cos\left(vp\theta\right) \tag{4.11}$$

$$= \frac{1}{2} \sum_{v=1,3,5,...} \left[cos\left(p\omega t - vp\theta\right) + cos\left(p\omega t + vp\theta\right)\right]$$

$$\mathcal{F}_{s,b} \propto \sum_{v=1,3,5,...} cos\left(p\omega t - \frac{2\pi}{3}\right) cos\left(v\left(p\theta - \frac{2\pi}{3}\right)\right) \tag{4.12}$$

$$= \frac{1}{2} \sum_{v=1,3,5,...} cos\left[p\omega t - vp\theta + \left(v-1\right)\frac{2\pi}{3}\right] +$$

$$\frac{1}{2} \sum_{v=1,3,5,...} cos\left[p\omega t + vp\theta - \left(v+1\right)\frac{2\pi}{3}\right] \tag{4.13}$$

$$\mathcal{F}_{s,c} \propto \sum_{v=1,3,5,...} cos\left(\omega t - \frac{4\pi}{3}\right) cos\left(v\left(p\theta - \frac{4\pi}{3}\right)\right) \tag{4.14}$$

$$= \frac{1}{2} \sum_{v=1,3,5,...} cos\left[p\omega t - vp\theta + 2\left(v-1\right)\frac{2\pi}{3}\right] +$$

$$\frac{1}{2} \sum_{v=1,3,5,...} cos\left[p\omega t + vp\theta - 2\left(v+1\right)\frac{2\pi}{3}\right] \tag{4.15}$$

The total MMF from the stator excitation $\mathcal{F}_s$ and the flux density can be expressed as

$$\mathcal{F}_s = \mathcal{F}_{s,a} + \mathcal{F}_{s,b} + \mathcal{F}_{s,c} \propto \sum_{v=6k\pm1} cos\left(p\omega t \mp vp\theta\right) \tag{4.16}$$

$$B_{n,s} = \Lambda\mathcal{F}_s \propto \Lambda \sum_{v=6k\pm1} cos\left(p\omega t \mp vp\theta\right) \tag{4.17}$$

where $k = 0, 1, 2, ...$ and $\Lambda$ is the airgap permeance [7, 27]. Of the spatial harmonics, $v = 1, 5, 11, 17...$ rotate forwards (indicated by the negative sign before the second term in the cosine function) whereas the harmonics $v = 7, 13, 19, ...$ rotate backwards. Note that the harmonics only consists of forward and backward rotating fields, all with a frequency equal to the fundamental electrical frequency. The harmonics $v = 3, 9, 15, ...$ are shifted in space by 0, -120 and -240 electrical degrees for the three phases and are therefore not appearing in the summation of the contribution from all three phases, as previously discussed.

In Fig. 4.5 the radial flux density is presented for a case with only armature excitation, the data is obtained with a solid rotor without any magnets or flux barriers to remove the influence of rotor flux and reluctance variations in the rotor. In the y-direction, mark *Position* ($\omega t$), the time dependency can be seen. In the x-direction, marked *Position* ($\theta$), the space dependency can be seen. In Fig. 4.6 the corresponding 2D-FFT of the time and space domain data is presented in a frequency/wave-diagram. As can be seen, the strongest circumferential orders are $-p = -5$, which is in line with theory obtained by $k = 0$ in (4.17). It is clearly seen that the harmonics present are focused at the frequency $p\omega t$. Additionally, harmonics appear at the orders $n = 40$ which is not consistent with (4.17). As for the rotor flux distribution, this is a result of the slotting in the stator, which is discussed in the following section. Comparing Fig. 4.5 to Fig. 4.3, it is seen that the flux has more sinusoidal characteristics in both time and space which is a result of the sinusoidal current exciting the stator windings. The influence of the stator slots can be seen in both figures.

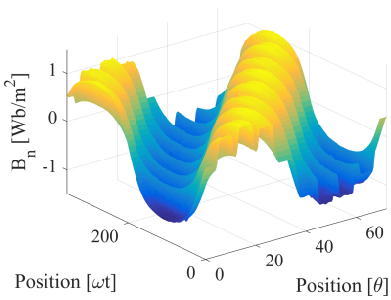


Figure 4.5: Radial airgap flux density as a function of both time ($\omega t$) and space ($\theta$) with only stator excitation.

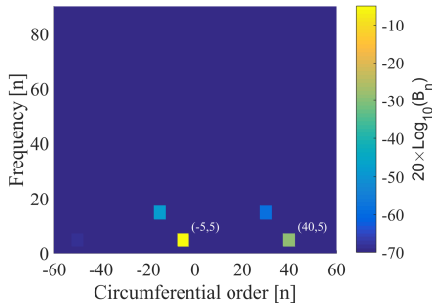


Figure 4.6: Frequency and mode number of the radial flux density from stator excitation derived by 2D-FFT.

### Effects of stator slots

When slots are introduced in the stator, a variation occurs in the airgap reluctance and hence the permeance. As previously discussed, the flux can be expressed by the product of magnetomotive force $\mathcal{F}(\theta, t)$ and permeance $\Lambda(\theta)$, as $B(\theta, t) = \mathcal{F}(\theta, t)\Lambda(\theta)$. A part of the rotor outer arc that is aligned with a stator tooth is in a preferred position experiencing minimum reluctance. Hence, the magnetic field is at its peak. Likewise, when a part of the rotor outer arc is aligned with

a stator slot, the resulting magnetic field is at its minimum due to the increased reluctance. When the rotor position is changed the pulsating magnitude difference in the magnetic field creates a force density which peaks during the alignment with the teeth and vice versa during alignment with the slots.

The influence of the variable permeance is seen in both the armature field and the rotor field. The previously derived equations for the MMF and the flux densities can be multiplied with a set of cosine functions representing the variations in the permeance, to include its influence on the harmonic content. The permeance can be expressed as a set of cosine functions with a periodicity defined by an integer multiplier of the number of slots as

$$\Lambda = \Lambda_{g0}\left[1 + \sum_{x=1,3,5,\ldots} A_x cos(xN_s\theta)\right] \simeq \sum_{x=0,1,3,5,\ldots} A_x cos(xN_s\theta) \tag{4.18}$$

where $N_s$ is the number of stator slots and $A_x$ is the magnitude of the $x^{th}$ harmonic [7]. Assuming that the permeance can be represented with a square wave, the harmonics appearing are all odd. Multiplying the obtained MMF in (4.16) with the variable permeance, the following expression is obtained for the armature flux density,

$$B_{n,s} \propto \sum_{v=6k\pm1} \sum_{x} cos\left(p\omega t \mp vp\theta \pm xN_s\theta\right) \tag{4.19}$$

where $k, x = 0, 1, 3, 5, \ldots$. As the equation unveils, additional space harmonics arise whereas the time frequency content is unchanged.

As can be seen in (4.19) with $k = 0$ and $x = 1$, the vibrational order $n = (-p + N_s) = 40$ arise. This harmonic is clearly seen in Fig. 4.6, rotating with a frequency of $p\omega t$.

In a similar manner, the PM flux density can be multiplied with the same permeance function resulting in the following expression

$$B_{n,m} \propto \sum_{u=2k-1} \sum_{x} B_{m,u} cos\left(up\omega t - \left(up \pm xN_s\right)\theta\right). \tag{4.20}$$

As can be seen in (4.20) with $k = 1$ and $x = 1$, the vibrational orders $n = -50$ and $n = 40$ arise. These two are clearly seen in Fig. 4.4, rotating with the frequency $p\omega t$.

### 4.2.2 Electromagnetic forces

In this section the derivation of the radial force density acting on the stator is presented. For this analysis the Maxwell Stress Tensor presented in (4.2) was used and simplified accordingly,

$$\begin{aligned} f_n(\theta,t) &= \frac{1}{2\mu_0}\left[B_n(\theta,t)^2 - B_t(\theta,t)^2\right] \\ &\simeq \frac{1}{2\mu_0}B_n(\theta,t)^2 \\ &= \frac{1}{2\mu_0}\left(B_{nm}(\theta,t) + B_{ns}(\theta,t)\right)^2 \end{aligned} \tag{4.21}$$

where subscripts $n$ and $t$ indicates radial and tangential components, respectively. As previously, $m$ and $s$ indicate origin from permanent magnets or stator excitation, respectively. Three parts are obtained if the equation is further evolved, contributions from the armature field only, permanent magnets only and a contribution from the interaction of both fields.

If for simplicity, no cross-coupling of harmonics are considered nor any stator slot influence, the three force density components can be expressed as

$$\begin{aligned} f_{n,s} &\propto \left[\sum_v cos\left(p\omega t \mp vp\theta\right)\right]^2 \\ &= \sum_v cos\left(2p\omega t \mp 2vp\theta\right) \end{aligned} \tag{4.22}$$

$$\begin{aligned} f_{n,m} &\propto \left[\sum_u cos\left(up\omega t - up\theta\right)\right]^2 \\ &= \sum_u cos\left(2up\omega t - 2up\theta\right) \end{aligned} \tag{4.23}$$

$$\begin{aligned} f_{n,sm} &\propto \sum_v \sum_u cos\left(p\omega t \mp vp\theta\right) cos\left(up\omega t - up\theta\right) \\ &= \sum_v \sum_u cos\left[(1 \mp u)p\omega t \pm (u \mp v)p\theta\right] \end{aligned} \tag{4.24}$$

where $v = 6k \pm 1$ and $u = 2k - 1$. Mathematically, the square of a sum results in a function of two summations. However, neglecting the interaction of different harmonics, i.e. cross-coupling between harmonics, the above expressions are obtained. In Fig. 4.7, 4.9 and 4.11 the force density are presented in time/space for PM excitation only, stator excitation only and normal operation, respectively.

In Fig. 4.8, 4.10, and 4.12 the force density for the three cases are presented with frequency/wave diagrams obtained from 2D FFT. Comparing the data with (4.23), (4.24) and (4.25) it is clear that the harmonics present are the expected ones. Additionally, when the rotor and armature fields interact, the harmonic content is rich. The pure circumferential modes, located on the line crossing the zero point, is the most dominating. As of before, the harmonics seen at $n = \pm 45$ with a frequency of $\omega t = 0$ result from interaction with the stator slots. Also, harmonics are not only concentrated to the diagonal (crossing circumferential order $n = 0$), but also to the diagonals crossing the circumferential orders $n = \pm 45$. These are also a result of the interaction with the stator slots.

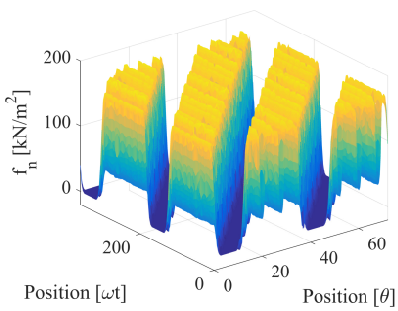


Figure 4.7: Radial force density as a function of both time ($\omega t$) and space ($\theta$) with only PM excitation.

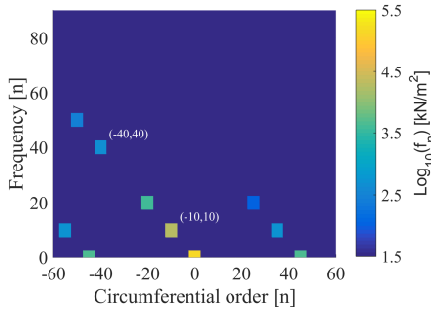


Figure 4.8: Frequency and mode number of the radial force density from PM excitation derived by 2D-FFT.

The harmonic content in both the stator and the rotor is affecting the torque production in the machine. If modes in the MMF originated from the stator are of the same order as those from the rotor, torque will be produced. If two modes have the same frequency components a smooth and steady torque will be produced. However, if the frequencies of the modes with the same mode numbers differ, the torque generation will pulsate. This is a result of the difference in relative speed of which the modes propagate in time.

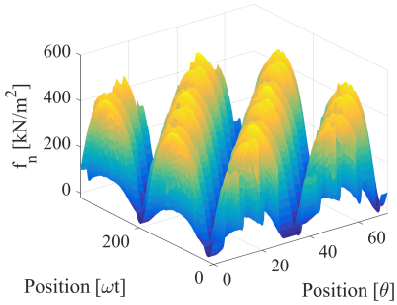


Figure 4.9: Radial force density density as a function of both time ($\omega t$) and space ($\theta$) with only stator excitation.

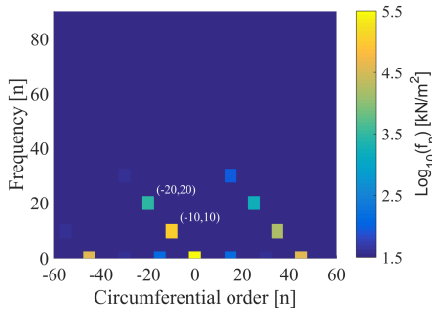


Figure 4.10: Frequency and mode number of the radial force density from stator excitation derived by 2D-FFT.

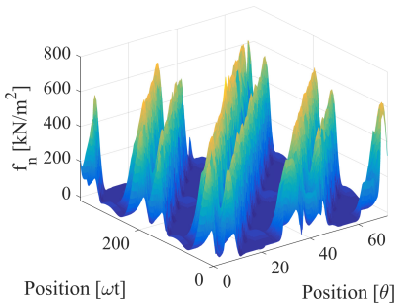


Figure 4.11: Radial force density density as a function of both time ($\omega t$) and space ($\theta$) with at normal load operation.

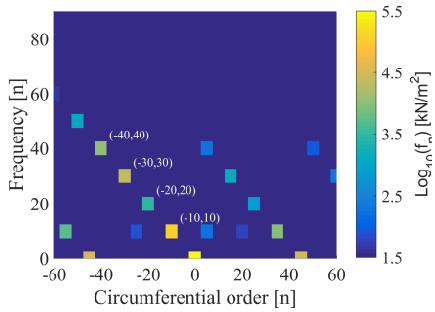


Figure 4.12: Frequency and mode number of the radial force density during normal load operation derived by 2D-FFT.

### 4.2.3 Radial and tangential components

In literature, usually, the tangential component is neglected in the context of force density calculations for simplification purposes [7, 22, 29]. Neglecting the tangential component is only valid if the difference in magnitude between the two components is sufficiently large. If the permeability is significantly higher in the ferromagnetic core than in the airgap, the tangential component of the flux density across the boundary at the stator teeth is strongly suppressed.

Assuming zero surface current on the stator teeth, the tangential component of the magnetic field on both sides of the boundary where the airgap meets the

teeth are the same since the surface current can be expressed as

$$J_s = H_{1t} - H_{2t} \tag{4.25}$$

where $H_{1t}$ and $H_{2t}$ is magnetic field in tangential direction at the two sides of the boundary, and $J_s$ is the surface current on the boundary. As a result, the tangential component of the flux density inside the stator teeth is significantly larger than in the airgap, due to the higher relative permeability. This can be explained as

$$H_{1t} = H_{2t} \rightarrow \frac{B_{1t}}{\mu_1} = \frac{B_{2t}}{\mu_2}. \tag{4.26}$$

Consequently, if the permeability is higher in the ferromagnetic material than in the airgap, so will the tangential component of the flux density also be. Additionally, Maxwell's equations and Gauss's theorem tells that the normal component of the flux density must be continuous across the boundary as a consequence of the law of conservation [22], [29]. With this in mind, it is understandable that the tangential component of the flux density is significantly lower than the normal component in the airgap at the boundary between airgap and stator teeth, which motivates the validity of ignoring the tangential component.

However, even zero tangential component at the boundary does not necessarily comply with flux density in the airgap consisting only of radial components, which might seem contradictory. However, even though the transition of flux through the boundary at a tooth consists only of a radial component, flux does not only flow through surfaces at teeth facing the rotor but also through surfaces facing adjacent teeth. Some of this flux is leakage and will not contribute to force density harmonics, but some will flow to or from the rotor. Consequently, the flux density across the air gap will consist of both tangential components as well as radial components, even though there are no tangential components at the boundary.

Consider a case, starting at the centerline of a stator tooth. For the flux density, it is reasonable that the radial component at the centerline of the tooth by far exceeds the tangential component, since the transition of flux from or to the tooth is of pure radial nature due to that the tooth and rotor are facing each other. However, as the angular position is changed from the centerline of a tooth towards a stator slot, conditions change, and the magnitude of the tangential component is increased whereas the radial component is significantly decreased.

This is partly a result of that the normal to the stator tooth is no longer facing the rotor, but instead the next stator tooth, giving a normal direction which is now parallel to the tangential direction of the rotor surface. Consequently, the radial and tangential flux density components suffer from irregularities occurring during every transition from stator tooth to stator slot or vice versa, seen from the angular position in the airgap [30].

In figure 4.13 the radial and tangential components of the flux density are presented, the data is obtained from FEM-simulations without stator excitation and is solely a result of the magnetization from the PMs. It is obtained geometrically in the center of the airgap. The location in the airgap at which the flux density is observed is of interest as it influences the characteristics of especially the tangential component. Closer to the stator the tangential component has more distinct peaks with a higher magnitude and less duration. In the figure, one can see discontinuities in both the radial and tangential components, as previously discussed. The irregularities are initialized as the stator contour facing the rotor are changed from stator tooth to stator slot.

Studying Fig. 4.14, illustrating a time instance of the same FEM-simulation, showing a region around the airgap and the flux lines, one can see the curvature of the flux lines and the concentration of flux in the stator teeth. In the airgap in the centerline of the figure, both the radial and tangential components of the flux density are zero correlating to an angular position of 100 electrical degrees in Fig. 4.13. In the tooth, to the left and the right of the centerline, the flux flows from the rotor to the stator, and from the stator to the rotor, respectively, indicated by the black arrows pointing in the direction of the flow.

In the figure, a majority of the flux is exciting the tooth to the right of the centerline in the lower rightmost corner, corresponding to an angular position of roughly 65 degrees in figure 4.13, where the tangential component is strongly negative. In the same way, a majority of the flux is entering the tooth to the left of the centerline in the lower leftmost corner, corresponding to an angular position of roughly 135 degrees in figure 4.13, where the tangential component, as well, is strongly negative.

With analogy to circuit theory, the magnetic flux follows the path of least reluctance, as previously discussed. Changes to the reluctance as a consequence of the mechanical rotation of the rotor or magnetic saturation will affect the flux density and hence the resulting forces acting on the stator. From Fig. 4.13 and 4.14 it is also reasonable to assume that the teeth dimensioning significantly

influence the magnitude of the harmonics in the airgap flux density.

To conclude, the accuracy of the simplification of neglecting the tangential component depends to a large extent on the objectives of the study and the point of data collection, i.e., the location in the airgap where the data is collected (in FEM-simulations). If the data is collected in the vicinity of the stator, in opposition to collecting the data close to the rotor surface, the tangential component might not be negligible. In the presented data obtained from FEM-simulations in the continuation of the thesis, both the radial and tangential components are included. However, in Section 4.2.2 only the radial component is considered for simplification purpose when the analytical expressions are derived for the force density harmonics.

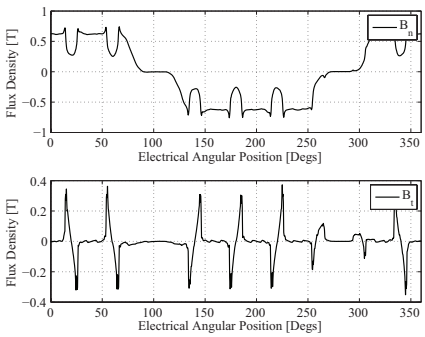


Figure 4.13: Radial and tangential flux densities as functions of electrical angular position in the airgap. The data is obtained from generator-mode FEM-simulations.

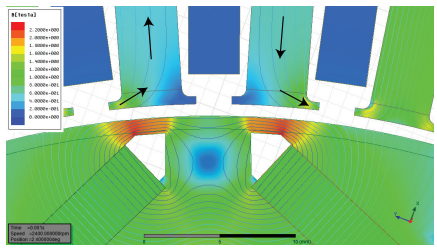

Figure 4.14: Flux linkage distribution and flux lines without stator excitation.

## 4.3 Basics of resonance, forced excitation and stator dynamic response

In this section, the space-frequency content of the excitation and the modal characteristics of the stator are investigated. Vibrational issues can be quantified as either resonance or a forced vibration. Resonances, with typically significant vibration and acoustic levels, occurs if the excitation frequency in both time and space coincides with that of a particular eigenmode of the structure. Whereas acoustic issues due to forced excitation is a result of the characteristics of the

excitation frequency content and the dynamics of the structure in general, rather than specific eigenmodes. Typically, a much larger force is required for a forced excitation to obtain a similar structural deformation as if resonance occurs.

The force excitation, acting on the stator, is given by the time evolution of the airgap flux density, of which the force excitation is obtained using Maxwell's Stress Tensor. With 2D Fourier analysis, the time-space excitation matrix can be decomposed into a frequency-based matrix of frequency and circumferential (spatial) content, respectively. Circumferential modes are hereafter expressed in pairs of $f(x, y)$, where $x$ is the spatial order and $y$ is the mode frequency (normalized to the fundamental mechanical frequency of the machine). The sign of $x$ indicates the rotational direction of the mode, which can be both positive and negative. A positive number indicated a clockwise rotation and a negative number indicates a counter clock-wise rotation.

### 4.3.1 Eigenmode assessment

The first five circumferential eigenmodes of the investigated machine are presented in Fig. 4.15-4.19. Although no general conclusions can be drawn from studying a specific machine, it is of importance to investigate the essential eigenmodes. As an important part of the nonlinear coupling between excitation and deformations, the eigenmodes can be of importance to motivate particular events. In essence, significant deformations with only a minor excitation force can only be achieved at a resonance. Henceforth, in such a case if no resonance occurs the validity of the result would be questionable.

As can be seen in the figures, the mode frequency of the lowest circumferential modes is in the span of a few hundred Hz up to several kHz. As discussed below, this matches the expected frequency content of the excitation during normal operation.

### 4.3.2 Dynamic response due to forced excitation

This section aims to describe the electromagnetic force excitation, dynamic stator response and deformation patterns, and the acoustic response of the investigated machine. For simplicity, a single operating point was used to exemplify and investigate its complex nature. All data was obtained from finite element modeling at a rotational speed of 4800 r/min, corresponding to a fundamental mechanical

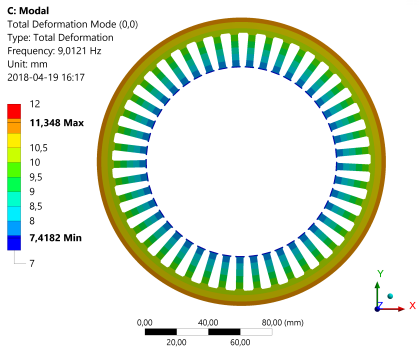


Figure 4.15: Vibrational mode (0,0) at resonance frequency 9 Hz.

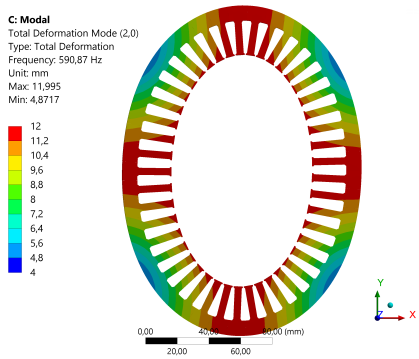


Figure 4.16: Vibrational mode (2,0) at resonance frequency 591 Hz.

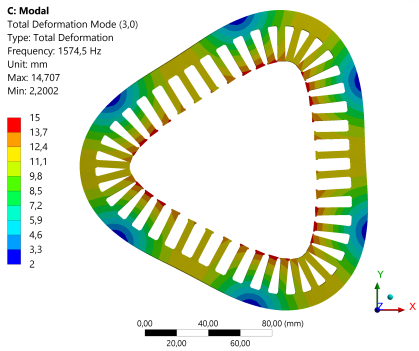


Figure 4.17: Vibrational mode (3,0) at resonance frequency 1575 Hz.

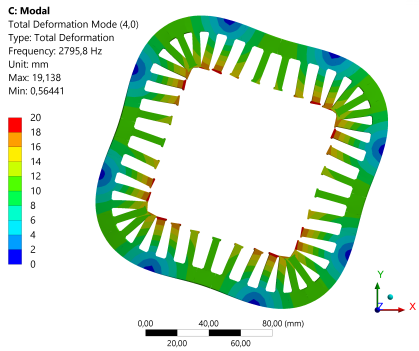


Figure 4.18: Vibrational mode (4,0) at resonance frequency 2796 Hz.

frequency of 80 Hz. The machine was loaded with an RMS current of 150 A and a dq-current angle of 135 degrees.

In Fig. 4.20, the frequency content of the radial airgap force is presented for the given operating point. The most prominent harmonics are highlighted with magnitude, spatial order and mode frequency, e.g. (-10,10) for spatial order -10 and mode frequency 10. As can be seen, in the frequency domain the excitation is limited to a set of contributors (eight of which are considered the most dominant ones). Henceforth, the excitation be categorized by a set of frequencies and spatial orders. These rotating forces cause the stator to deform, generating a dynamic response. This response can be either due to resonance or forced excitation. For the given operating point and the window of succeeding analyses provided hereafter,

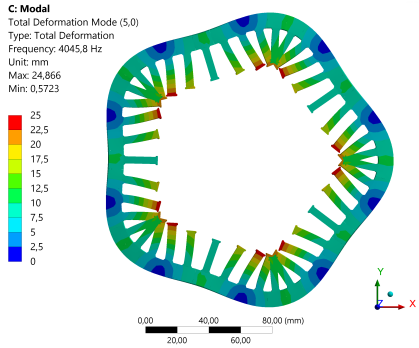


Figure 4.19: Vibrational mode (5,0) at resonance frequency 4046 Hz.

no resonances are excited, and the responses presented are thereby exclusively due to forced excitation.

Based on the excitation presented in Fig. 4.20, one can expect the dynamic response of the stator to show significant deformations at frequencies of integer multiples of 10 times the fundamental mechanical frequency. Likewise, significant radiated acoustic noise can be expected at these frequencies. The complexity of the nature of acoustic e-machine noise is much related to the fundamental understanding of the underlying excitation and its frequencies and spatial orders - A seemingly harmless, and in magnitude insignificant, excitation contribution can cause significant deformations and acoustic noise, even without the appearance of structural resonance.

At mode frequency 10 and 20 times the fundamental mechanical frequency (i.e., 800 and 1600 Hz), three spatial orders are dominating each frequency, whereas, for 30 and 40 times the fundamental mechanical frequency (i.e., 2400 and 3200 Hz), only one spatial order is dominating each frequency. For each of these frequencies, the resulting spatial orders that can be expected in the deformation of the stator is the circumferential orders given at each frequency.

In Fig. 4.22, 4.23, 4.24 and 4.25, the stator deflection is presented for each of the four frequencies (800, 1600, 2400 and 3200 Hz), respectively. Note that the coloring scaling differs to accurately accumulate the deflection range.

At 800 Hz (mode frequency 10), the spatial orders -10, 5 and 20 are predominant; this is seen in the force harmonics excitation data presented in Fig. 4.20. Studying the stator deflection, shown in Fig 4.22 and more detailed in

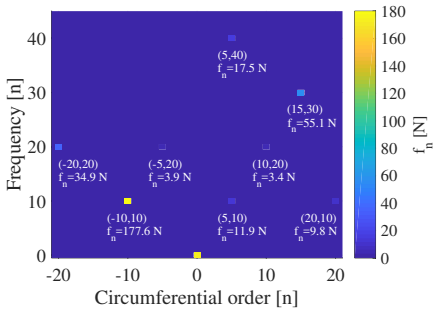


Figure 4.20: Radial force harmonics at 4800 r/min in the frequency range of 0-45 times the fundamental mechanical frequency (corresponding to 0-3600 Hz).

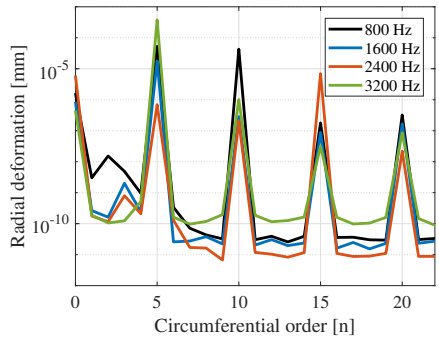


Figure 4.21: Spatial frequency content of the average (in z-direction) radial deformation in the circumferential direction at 800-1600 Hz.

Fig. 4.21, it can be seen that the most predominant force harmonics yields the most significant deformations. However, the magnitude of the deflections does not depend linearly with the excitation. Comparing the excitation of spatial modes -10 and 5, the excitation force is roughly 15 times higher for spatial mode -10, whereas the $10^{th}$ deformation mode is only roughly 80 % of the $5^{th}$ deformation mode. This demonstrates the non-linearities that act within the system. Hence only minor conclusions can be drawn based on the excitation. Furthermore, this is potentially a problematic frequency, both considering vibrations, and radiation noise, due to the significant deformation of the $5^{th}$ circular mode, in relation to its comparatively high radiation efficiency.

At 2400 Hz (mode frequency 30), the spatial order 15 is dominating. As can be seen in Fig. 4.21, the $15^{th}$ circumferential mode yields the highest deformation of all circumferential modes at that frequency. However, due to the high mode number, this is not likely to cause any significant issues considering radiated acoustic noise. Moreover, the magnitude of the deformation itself is low hence vibrational issues are unlikely, as well.

At 3200 Hz (mode frequency 40), the spatial order 5 is dominating. Despite the moderate force, it causes a significant deformation, which is seen in Fig. 4.25. As can be seen in Fig. 4.21, it causes the most severe deformation of all, considering the four frequencies presented. The high radiation efficiency associated with low circumferential orders, as well as the significant deformation (more than 10 times

the deformation at both 1600 Hz and 2400 Hz), characterizes this deformation to be the most critical one. Moreover, the high frequency (40 times the fundamental frequency), causes further issues. If the rotational speed was increased by only 25 %, to 6000 $r/min$, this harmonic in the excitation would coincide with the resonance of the $5^{th}$ mode shape.

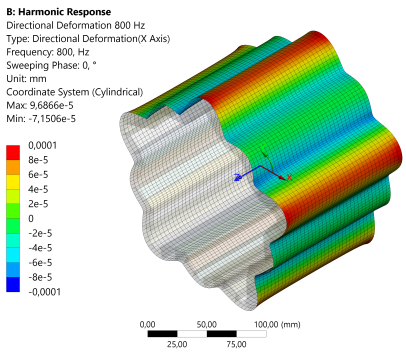


Figure 4.22: Radial deformation of the stator yoke surface at 800 Hz.

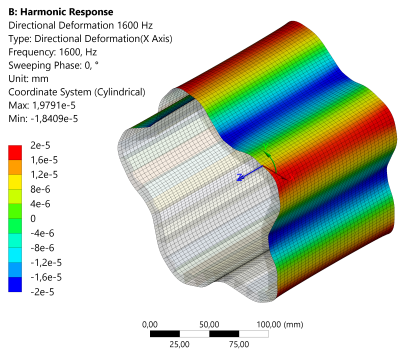


Figure 4.23: Radial deformation of the stator yoke surface at 1600 Hz.

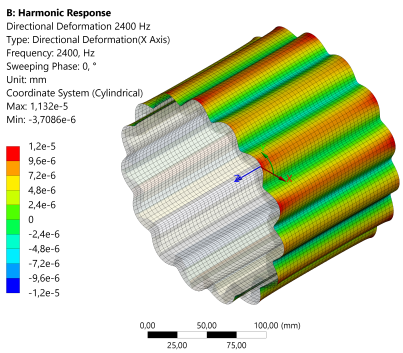


Figure 4.24: Radial deformation of the stator yoke surface at 2400 Hz.

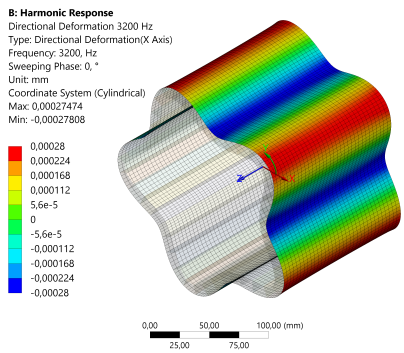


Figure 4.25: Radial deformation of the stator yoke surface at 3200 Hz.

In Fig. 4.26, 4.27, 4.28 and 4.29, the corresponding acoustic pressure at a time instance is given. In Fig. 4.30, 4.31, 4.32 and 4.33, the sound pressure level (SPL) is given for the corresponding frequencies. As can be seen, the $4^{th}$ frequency component (3200 Hz) yields the highest SPL.

Returning to Fig. 4.20, one can conclude that minor harmonic components have the ability to cause significant acoustic noise. This is clearly demonstrated

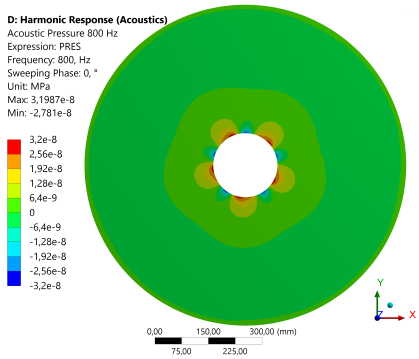


Figure 4.26: Acoustic pressure at 800 Hz.

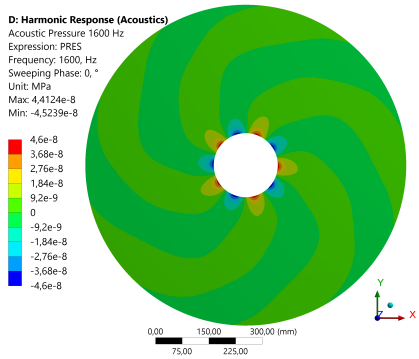


Figure 4.27: Acoustic pressure at 1600 Hz.

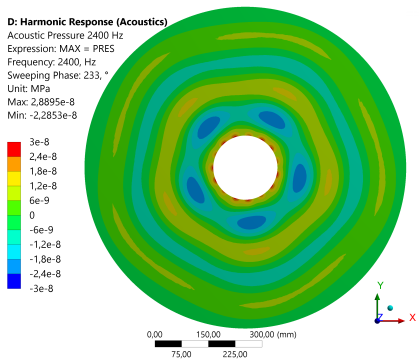


Figure 4.28: Acoustic pressure at 2400 Hz.

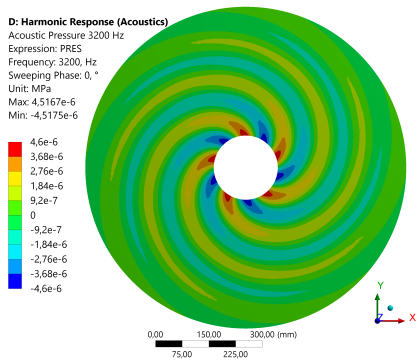


Figure 4.29: Acoustic pressure at 3200 Hz.

for most of the low spatial harmonics.

In Paper IV, a study on a non-cylindrical rotor surface is presented. The study is based on the consequences of dynamic response from forced excitation. The aim of the study was to reduce specific harmonics, by geometrically altering the outer part of the rotor. The harmonics in focus was the low circumferential ones in the frequency range from 10 to 50 times the fundamental mechanical frequency. Despite the novelty of the approach and a single operating point analysis, it demonstrates the necessity of basic understanding of the concept of force creation and frequency contributions in both time and space. Moreover, a significant acoustic noise reduction (between 6 and 6.8 dB) was achieved for the most prominent harmonics, while the reduction of average torque was less than

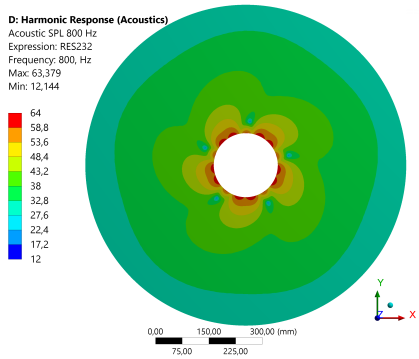


Figure 4.30: Sound pressure level at 800 Hz.

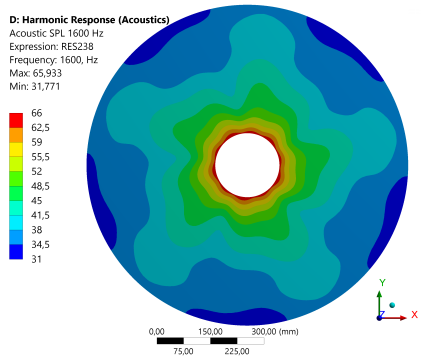


Figure 4.31: Sound pressure level at 1600 Hz.

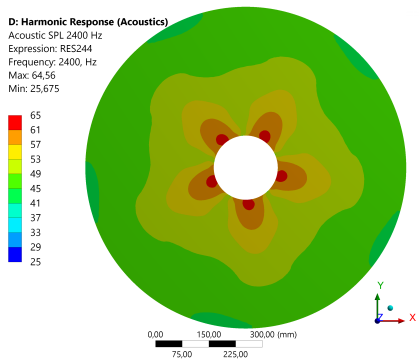


Figure 4.32: Sound pressure level at 2400 Hz.

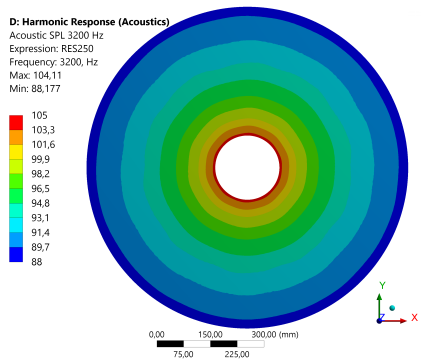


Figure 4.33: Sound pressure level at 3200 Hz.

2.7 %. Additionally, a core loss reduction of roughly 8 % was also achieved for the same solution. Altogether, argumentation for any significant energy efficiency improvements cannot be fully supported. On the contrary, the proposed method does not indicate any adverse effects on the efficiency at the investigated operational point.

# Inverter Control

The inverter used in this work is a two-level IGBT-based three-phase inverter, described more in detail in Section 5.1. Technical specifications are given in Section 2.1. In Section 5.2, different modulation techniques and randomized switching frequency is covered. In Section 5.3, evaluations are given considering both electrical and acoustic quantities. For more details and further assessments, the interested reader is referred to Paper I, II and III, where the two foremost covers the aspects of inverter energy efficiency and harmonics, whereas the later also incorporates acoustic noise emissions.

## 5.1 Three-phase voltage source inverter

A voltage source inverter can be used to control voltage magnitude and frequency, to allow for variable speed drive operation. A typical topology used in industrial applications is the two-level inverter, illustrated in Fig. 5.1. Besides the two-level inverter, there are additional topologies such as variations of multi-level inverters and the neutral point clamped inverter (NPC-inverter). Both have recently been of increasing interest targeting automotive use [31, 32, 33]. Although, it is not evident which inverter topology to favor. The research presented in [31, 32, 33] indicates that multi-level inverters are likely to operate with higher inverter efficiency than a two-level inverter. On the other hand, commonly highlighted drawbacks are the increased number of discrete components, such as switches and gate drivers, and more complex control and modulation strategies. Additionally, due to the different current harmonic content, losses in for example the battery might increase when using a multi-level inverter instead of a two-level inverter [31, 32].

Each of the three phases ($v_a$, $v_b$, $v_c$) can be connected to either $\pm V_{dc}/2$, independently of each other. Consequently, $2^3 = 8$ voltage vectors can be created where six of them are active, and two are zero vectors, illustrated in Fig. 5.2. Note that voltage vector $u_{111}$ and $u_{000}$ are the so-called zero vectors implying that all three phases simultaneously are connected to either $\pm V_{dc}/2$. During operation, the vectors are combined to achieve an average voltage corresponding to the references for each phase.

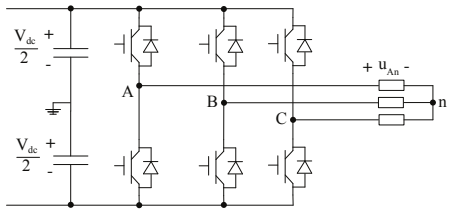


Figure 5.1: Illustration of a three-phase voltage source inverter.

In the stationary reference frame ($\alpha\beta$-reference frame) the output vector $v_{\alpha\beta}$ are limited to [34]

$$v_\alpha = \left(0,\ \pm\frac{V_{dc}}{2},\ \pm\frac{2V_{dc}}{3}\right) \tag{5.1}$$

$$v_\beta = \left(0,\ \pm\frac{2V_{dc}}{\sqrt{3}}\right), \tag{5.2}$$

which is a result of the amplitude invariant $\alpha\beta$-transformation according to

$$\begin{bmatrix} v_\alpha \\ v_\beta \end{bmatrix} = \begin{bmatrix} \frac{2}{3} & -\frac{1}{3} & -\frac{1}{3} \\ 0 & \frac{1}{\sqrt{3}} & -\frac{1}{\sqrt{3}} \end{bmatrix} \begin{bmatrix} v_a \\ v_b \\ v_c \end{bmatrix} = \frac{V_{dc}}{2} \begin{bmatrix} \frac{2}{3} & -\frac{1}{3} & -\frac{1}{3} \\ 0 & \frac{1}{\sqrt{3}} & -\frac{1}{\sqrt{3}} \end{bmatrix} \begin{bmatrix} s_a \\ s_b \\ s_c \end{bmatrix}.$$

The largest voltage magnitude that momentarily can be created is

$$|v_{\alpha\beta}|_{max} = \frac{2V_{dc}}{3}, \tag{5.3}$$

whereas the limit for linear modulation is

$$|v_{\alpha\beta}| = \frac{V_{dc}}{\sqrt{3}}. \tag{5.4}$$

In Fig. 5.2 this can be seen as the largest circle that can be created inside of the hexagon, illustrated by the dashed circle.

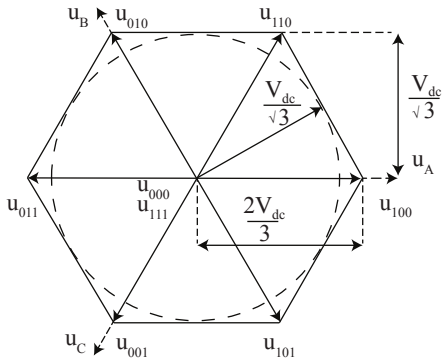


Figure 5.2: Illustration of voltage vectors for a two-level VSI.

## 5.2 Pulse width modulation techniques

Pulse width modulation (PWM) is essential for the operation of voltage source inverters and variable speed drives. In principle, each of the three legs of the inverter is alternately connected to either $\pm V_{dc}/2$ to, over a given time, obtain a specific average voltage level. A voltage corresponding to a reference determined by the control system. What differentiates modulation techniques is the composition of active- and zero voltage vectors building the average voltage each switching period. Without loss of generality, any of the six active, and the two zero-voltage vectors, can be combined to obtain an arbitrary average voltage (while adhering to the physical constraints of the inverter). Naturally, some combinations and sequences are more favorable than others, considering for instance inverter losses and harmonic content of the modulated voltage [34].

For industrial applications, such as electrification of propulsion systems in the automotive industry, sideband harmonics around the switching frequency usually is in the hearable frequency range due to switching frequency in the region of 5-10 kHz. Apparently, the switching frequency can be increased beyond the range of the human ear, and thereby suppress issues related to noise and vibrations. However, this would be a sub-optimal solution, where the inverter efficiency would be overridden in favor of acoustic performance. A fact which is also true in the wake of emerging switch topologies, such as Silicon carbide and Gallium nitride-based

switches - Despite the effectiveness and capabilities of the power devices used, switching faster than what is necessary is sub-optimal. Alternative modulation techniques and switching frequency randomization can lower that limit of what is necessary.

Based on this hypothesis, the effects of randomization of the switching frequency are of interest to investigate, primarily from a noise perspective. The technique is simple and seems like a yet effective measure to decrease the switching noise from electric drive units. Simply by the smearing out the harmonic components and thereby decrease the tonality. However, it is not evident that this will have any positive effects on the experienced noise and its perception, which at first thought might seem contradictory. The reason for this is that tonality is not by any means the only sound quality metrics. Alongside tonality, measures such as overall sound pressure level might be more influential on the perceived annoyance. Although, the technique is simple and seems like a yet effective measure to decrease the switching noise from electric drive units. Another area of interest is the combination of for example DPWM and randomization of the switching frequency to harvest the benefits of DPWM while at the same time partly suppress its drawbacks.

Different modulation techniques and switching frequency randomization have frequently been researched and evaluated from an electrical perspective [35, 13, 14, 15, 16, 17]. In [35] different discontinuous PWM (DPWM) methods are investigated focusing on inverter energy efficiency. The authors conclude that DPWM is the modulation technique of choice due to a substantial decrease in losses as a result of the decreased number of switching events, i.e., number of commutations.

In [13] and [14], focusing on harmonic spreading and efficiency, different random PWM techniques are investigated. The authors observed a significant decrease in harmonic intensity and advocate benefits from an EMI perspective. Most often the harmonic spread of inverter output current, power spectral density, and energy efficiency are considered while potential drawbacks such as noise emissions often are disregarded.

Moreover, modulation techniques' influence on magnetic noise have been investigated by several researchers as well [8, 9, 10, 11, 12, 36, 37, 38, 39, 40]. Specifically, [8, 9, 10, 11, 12] covers permanent magnet synchronous machines. Random switching frequency PWM has been pointed out as the main technique, besides increasing the switching frequency, for improving the acoustic sensation

[9, 12, 36, 37, 38, 39] thanks to the non-tonal spectrum around the switching frequency and its multiples. However, apart of utilization of suggested sound quality metrics for quantification of the acoustic exposure as by Ma and Zuo [11], Sarrazin et al. [12] and Cho et al. [37], investigations on the perception due to modulation techniques have not been found in available literature.

The modulation techniques investigated in this work is based on carrier wave comparison. In Fig. 5.3, the carrier wave comparison is illustrated. The times located on the x-axis illustrates a total time equal to the switching period. As can be seen, the switching period is divided into 7 sections marked with the times $t_0$, $t_1$, $t_2$ and $t_7$. Of these ones, $t_0$ and $t_7$ are zero vectors whereas $t_1$ and $t_2$ are active vectors. The voltage references are obtained from the control system and averaged over one switching period. Hence the output average equals the reference value for each phase.

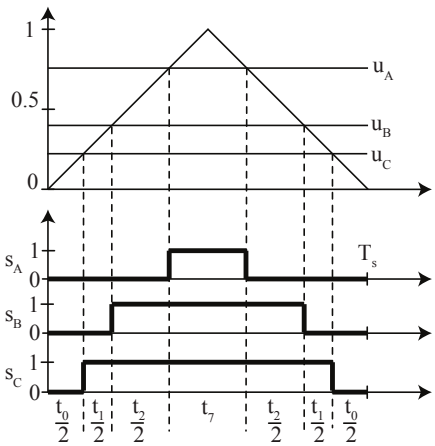


Figure 5.3: Carrier wave comparison example.

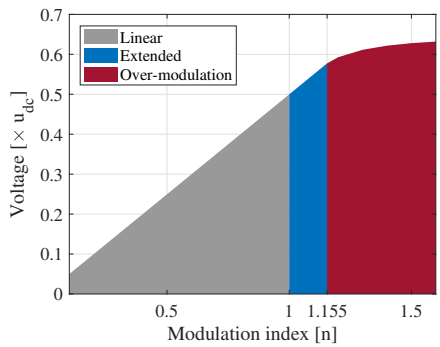


Figure 5.4: Inverter output voltage characteristics.

### 5.2.1 SPWM with third harmonic injection

As previously discussed in Section 5.1, the theoretical upper limit for linear modulation is $|v_{\alpha\beta}|_{max} = V_{dc}/\sqrt{3}$. The regions of linear modulation, extended linear modulation and over-modulation are shown in Fig. 5.4, where the output peak voltage is given as function of modulation index, $m_a$. The figure also demonstrates the problem of over-modulation, namely the non-linear relation between modulation index and output voltage. If the inverter is controlled to

operate in the over-modulation region, the loss of linearity requires additional attention [41].

The limit of extended linear modulation ($m_a$=1.1547 in Fig. 5.4) can not be reached with SPWM without any form of reference alterations. For example, if a voltage reference of $v_{\alpha\beta} = V_{dc}/\sqrt{3} + j0$ is to be realized, the average values of the switching states required during a switching period are $\left[2/\sqrt{3},\ -1/\sqrt{3},\ -1/\sqrt{3}\right]$ (according to the amplitude invariant transformation presented in (5.1)). Note that $s_a = 2/\sqrt{3} > 1$ which will cause over-modulation. Consequently, the maximum output voltage magnitude possible without any alterations of the three-phase voltage references is

$$|v_{\alpha\beta}|_{max} = \frac{\sqrt{3}}{2}\frac{V_{dc}}{\sqrt{3}} = \frac{V_{dc}}{2} \tag{5.5}$$

resulting in average switching states of $[1,\ -1/2,\ -1/2]$, which is achievable in the linear modulation region (corresponding to modulation index $m_a$=1).

To overcome the previously explained issue with the limitation of not being able to utilize the entire hexagon, presented in Fig. 5.2, zero-sequence injection was used. In accordance with the three-phase theory of wye-connected machines, a zero-sequence component of arbitrary magnitude can be added to all three phases without in any way affecting the resulting three-phase system. A prerequisite is that the load is symmetrical, which is a reasonable assumption for electrical machines. The technique used here to maximize the utilization of the hexagon is the symmetrical sub-oscillation method. The zero sequence component, $\Delta$, to be added to the three references is calculated based on the instantaneous values of the three phases according to [34]

$$\Delta = \frac{max\left(u_a,\ u_b,\ u_c\right) + min\left(u_a,\ u_b,\ u_c\right)}{2}. \tag{5.6}$$

In practice, the method creates a continuous symmetry between the maximum and minimum values of the phase voltage references and thereby enabling higher output voltage without the use of over-modulation control. In Fig. 5.5 and 5.6 the concept is illustrated. In Fig. 5.5 the zero sequence component can be seen. With the proposed method it has the shape of a triangular wave. In Fig. 5.6 the results of adding the zero-sequence to the sinusoidal references are seen.

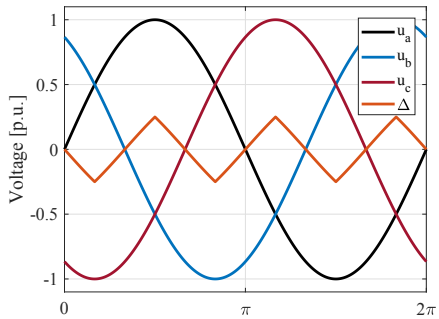


Figure 5.5: Sine phase potential references and the zero sequence component based on the symmetrical sub-oscillation method.

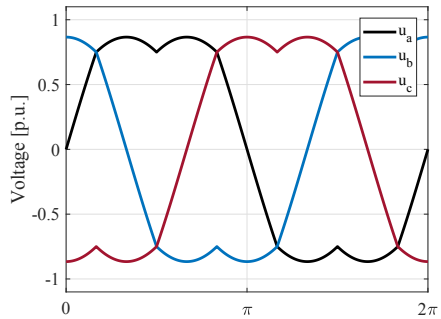


Figure 5.6: Resulting phase potential references obtained by addition the zero sequence component to all three phases.

### 5.2.2 Discontinuous PWM

Discontinuous PWM (DPWM) is a category of modulation techniques where the common objective is to clamp phase voltages to either $\pm V_{dc}/2$ to reduce the number of commutations and thereby the inverter losses. Several approaches, with the aim to increase energy efficiency, are presented in literature [42, 43], and references therein. In [42] space-vector based synchronized DPWM for applications with large ratios between the switching frequency and fundamental frequency is evaluated. The work focuses on switching losses and total harmonic distortion (THD) of both the voltage and the phase current, using a three-level inverter. Four DPWM strategies (DPWM I-IV) are investigated. The author differentiates among these based on when the clamping occurs and the angular spread of the clamping, i.e., the number of electrical degrees one phase is clamped. The paper concludes several benefits using DPWM in general, such as decreased switching losses and unsurprisingly even a decrease in phase current THD for the given load case.

Hadj [43] investigates DPWM using a fixed clamping interval of 60 electrical degrees. The author concludes that the method reduces the inverter switching losses for the given load case. However, results for operational points other than the one covered as well as the impact on electromagnetic torque characteristics are not treated.

Thus, lacking in available literature are analyzes covering adverse effects on electromagnetic torque ripple, more comprehensive energy efficiency investigations

and the results on machine losses and radiated noise and vibrations.

In this work, a few DPWM methods are considered, closely related to what is described as DPWM II and III by Beig et al. [42]. DPWMMIN and DPWMMAX are two methods that are conceptually the same but operates as the inverse to each other. When using DPWMMAX, the objective is to clamp the phase with the highest reference voltage to $+V_{dc}/2$ whereas the DPWMMIN method clamps the phase with the lowest reference voltage to $-V_{dc}/2$. The objective is to decrease the number of commutations and lower the inverter losses. As for the aforementioned techniques, third harmonic injection is utilized by adding additional signal content to the three phases, as discussed in the previous section.

Mathematically, DPWMMIN and DPWMMAX are expressed as

$$u_0 = \begin{cases} -\frac{V_{dc}}{2} + max\left(u_a, u_b, u_c\right) & \text{DPWMMAX} \\ \frac{V_{dc}}{2} + min\left(u_a, u_b, u_c\right) & \text{DPWMMIN} \end{cases}$$

where $u_0$ is the zero sequence component to be subtracted from the phase voltage references. The two methods are combined to alternately clamp the highest or lowest phase to the positive or negative dc-link, respectively, as the voltage reference propagates in the $\alpha\beta$ - reference frame. In Fig. 5.7, the phase voltage references and the calculated zero sequence components are presented. In Fig. 5.8, the resulting phase voltage when the zero sequence component is subtracted.

As can be seen, the method clamp one phase at the time to either $\pm V_{dc}/2$ during a total of 120 electrical degrees. Considering the consequences of this technique, it is evident that in total, one of the phases remains clamped throughout each switching period reducing the number of commutations by 1/3. The attentive reader questions the reason for centering the clamping period over the peak voltage when it would decrease the losses even further if it is phase shifted to clamp during a period when the transmitted power is at its peak. There are a few options in how to place the clamping region. This study is limited to clamping around the peak voltage as an initialization to DPWM methods.

### 5.2.3 Random PWM

Randomization of the switching frequency can be used to decrease the tonality in the emitted noise from the machine. As previously discussed and further evaluated in Paper IV, the tonality of the emitted noise is thought to be a variable of importance for the perception of noise hence motivating the need for the

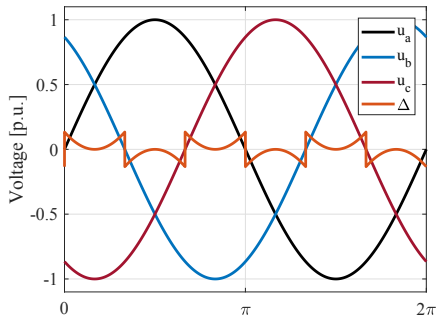


Figure 5.7: DPWM: Three-phase voltage reference and zero sequence component.

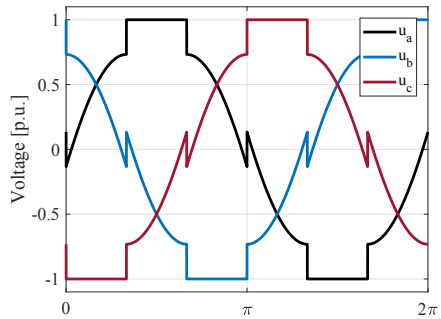


Figure 5.8: DPWM: Resulting phase potential references.

investigation. In this work, the randomization was based on a given distribution with an expected value and a variance. Both Uniform and Gaussian distributions have been considered, implemented and evaluated.

Implementation of variable switching frequency can be done in different ways. In the chosen configuration, the switching frequency defines the data sampling and the update frequency of the control system. The phase current sampling is synchronous with the trigger wave for the PWM and data was sampled at the center of each switching period. Subsequently, the second half of the switching period was intended for the control system to calculate the next reference values to be supplied to the PWM modulator at the start of the next switching period.

When the switching frequency was changed, the delay from sampling to execution needs to be supervised and known to a high certainty for proper compensation to be possible. Moreover, the integrators in the controllers need to be considered when the update frequency is changed in the control system, to assure that errors are not introduced. Collectively, scheduling and timing are of importance when randomization of the switching frequency is used.

### 5.2.4 Voltage harmonics analysis

In Fig. 5.9 and 5.10, low frequency phase voltage harmonics are presented for the two modulation techniques (SPWM and DPWM), respectively. The fundamental component of both methods is in accordance with the data presented in Fig. 5.4, showing the linear modulation followed by the over-modulation regions, as the

modulation index is increased above 1.1547. For the remaining harmonics, the characteristics differ between the two. As can be seen around modulation index 1, the DPWM yields a less significant magnitude for the $3^{rd}$. In Fig. 5.11 and 5.12, the most prominent harmonics around the switching frequency ($f_s$) is presented for the two methods as function of modulation index. Interestingly, a significant difference exists.

Combined, the low-frequency harmonics and the harmonics around the switching frequency show on optimization possibilities. Despite the deteriorated characteristics for DPWM at low modulation indices, the area around $m_a = 1$ is interesting to study. The hypothesis in the work related to modulation techniques was that the discontinuity in DPWM could be utilized without suffering from its drawbacks. The aim was to increase the inverter efficiency without deteriorating the acoustic performance of the drive system. Further details on this topic is given in Paper I, III and V as well as in Section 5.3.

## 5.3 Evaluation of modulation techniques

### 5.3.1 Energy efficiency analysis

#### Calculation of inverter losses

The inverter losses were calculated based on linear scaling of the energy loss data for the IGBT module, with respect to the conducted phase current and the dc-link voltage. The switching losses for the each of the IGBT modules and the diodes were calculated as

$$P_{sw,IGBT} = \frac{1}{T_s}\left[(E_{on} + E_{off})\,\frac{i_{ph}}{I_{ref}}\frac{u_{dc}}{U_{ref}}\right] \tag{5.7}$$

$$P_{rr,diode} = \frac{1}{T_s}\left[E_{rr}\frac{i_{ph}}{I_{ref}}\frac{u_{dc}}{U_{ref}}\right] \tag{5.8}$$

where $T_s$ is the switching period time and $E_{on}$, $E_{off}$ and $E_{rr}$ are the energy loss constants during turn-on, turn-off and diode reverse recovery, obtained from the supplier of the IGBT module.

It is worth noting that the proposed method for inverter losses estimation is tainted with uncertainties. The energy loss for a switching event is, for instance,

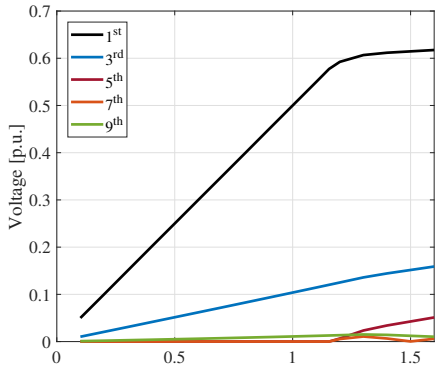


Figure 5.9: SPWM: Low frequency harmonics.

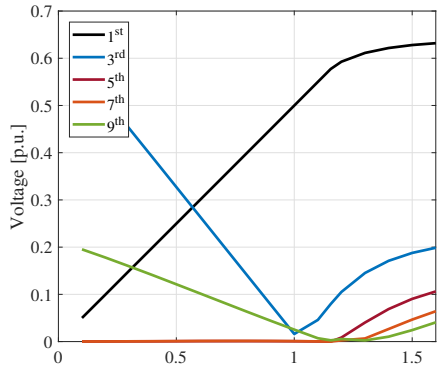


Figure 5.10: DPWM: Low frequency harmonics.

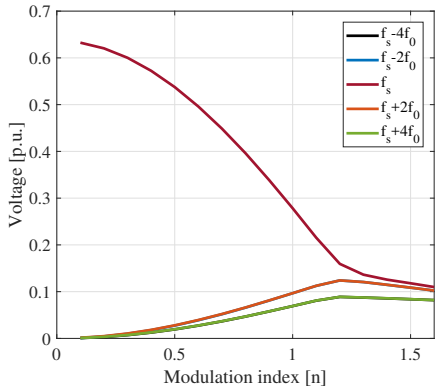


Figure 5.11: SPWM: Most prominent switching frequency harmonics.

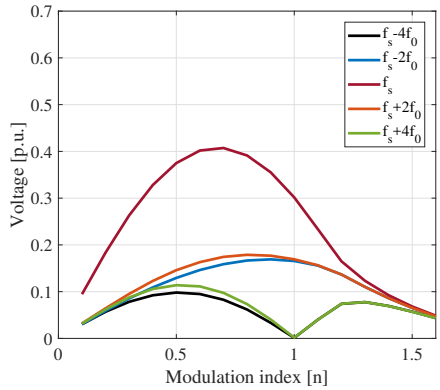


Figure 5.12: DPWM: Most prominent switching frequency harmonics.

dependent on the characteristics of the gate pulse and the gate drive circuit characteristics, as well as the inductance in the commutation circuit. Clearly, in the application, if these deviate from what was used in the setup where the energy loss constants, $E_{on}$, $E_{off}$ and $E_{rr}$, were determined, it is likely that the results to some extent will be erroneous. Additionally, the losses are assumed to be linearly dependent on the conducted current and the voltage across the device, which is a simplification that might add to the error.

The conduction losses for each discrete component in the inverter were calculated as the sum of the conduction current times the forward voltage drop, occurring as a result of the PN-junction, and the resistive conduction losses as,

$$P_{cond} = v_f i_{ph} + R_{on} i_{ph}^2 \tag{5.9}$$

where both the forward voltage drop $v_f$, and the resistance $R_{on}$ differs between the IGBT switch and diode.

### Comparison between SPWM and DPWM

In Fig. 5.15 and 5.16 the percentage difference in total inverter losses between the two modulation techniques are presented, in Fig. 5.15 based on simulations and in Fig. 5.16 based on measurements. The percentage difference was calculated as

$$\Delta P = \frac{P_{DPWM} - P_{SPWM}}{P_{DPWM}} \times 100\% \tag{5.10}$$

Firstly, the results show a rather significant decrease in the inverter losses for the entire operational area. As approximately one-third of the switching events are canceled when DPWM is used, the switching losses are expected to decrease with roughly the same order, assuming that the load is inductive, and the phase current is slightly lagging the voltage.

A question that can be asked about the validity of the results and the influence of the specific IGBT module is: *Are the results general, in the sense that they hold for other modules as well or are they module type specific?* The results are for obvious reasons not unanimous for all IGBT modules. However, simulations with a second IGBT module of similar specifications (Infineon FS400R07A1E3) show very similar results when comparing the difference in losses for the two modulation techniques. Which indicates that the results presented in this thesis are showing a typical behavior. The difference in loss decrease between the two IGBT modules, based on simulations, where less than two percentage points.

As previously discussed, the losses occurring in the IGBT modules depends on the stray inductance, the gate current, etc. Therefore, it is likely that the simulation results, based on the aforementioned equations presented in Section 5.3.1, are subjected to errors which are a result of the simplified approach of calculating the losses. In Fig. 5.13 and 5.14, the absolute values of the inverter losses are presented for simulations and measurements, respectively. As can be seen, the simulations over-estimates the losses slightly.

Furthermore, despite the drawbacks of the selected approach of inverter loss calculations, comparatively the method gives good results, which can be seen

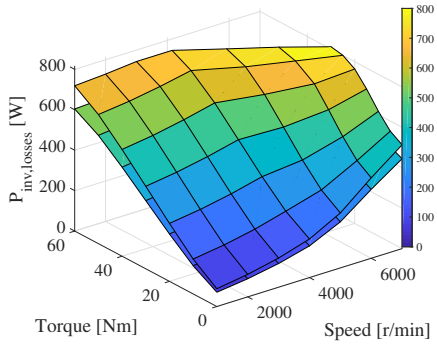


Figure 5.13: Total inverter losses for SPWM (upper surface) and DPWM (lower surface) based on simulations.

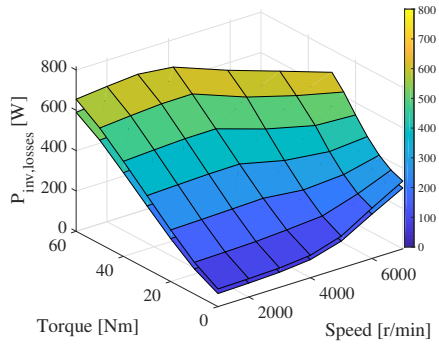


Figure 5.14: Total inverter losses for SPWM (upper surface) and DPWM (lower surface) based on measurements.

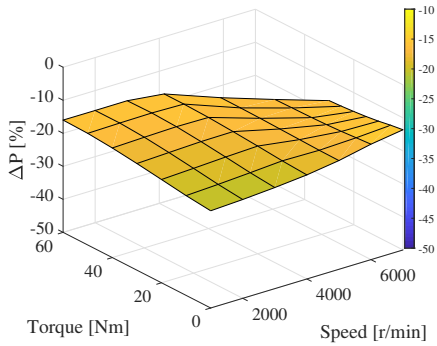


Figure 5.15: Difference in percent of total inverter losses between SPWM and DPWM based on simulations.

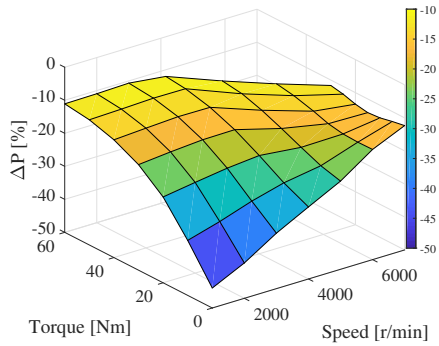


Figure 5.16: Difference in percent of total inverter losses between SPWM and DPWM based on measurements.

by comparing Fig. 5.15 and 5.16, where the percentage difference between the two modulations techniques are presented based on simulations and measurements, respectively. The same characteristics can be seen in both the measurements and the simulations, although the dynamics in the measurements are enlarged in absolute terms. At high rotational speeds, with low torque, the difference in losses is less significant, which clearly can be seen in Fig. 5.16. This is a result of the low power factor. In this area, mostly reactive power is fed to the machine to counteract the PM flux and thereby the induced voltage. Consequently, the power transfer is shifted from the switches to the diodes, hence the inverter switching has less influence.

### Core losses

When the modulation technique is changed, so are the harmonic spectra of the phase current [44]. As a consequence, it is reasonable to also assume changes in the core losses in the electrical machine. Three load cases were investigated numerically with finite element analysis, with the voltage excited FEM method proposed in Section 3.3. At the three different load cases, the machine was operated at 3500 r/min, with a load torque of 15, 35 and 55 Nm.

The Bertotti equation was used to evaluate the core losses for the three load cases, expressed as

$$P_{fe} = k_h f B^2 + k_c \left(fB\right)^2 + k_e \left(fB\right)^{1.5} \tag{5.11}$$

where the first and second parts constitute hysteresis losses and eddy current losses, respectively, and the third part covers the excess losses. $k_h$, $k_c$, and $k_e$ are material specific parameters whereas $B$, and $f$ are the peak value of the flux density and the flux density frequency, respectively [19].

In Table 5.1, a loss matrix is presented where the two PWM methods are compared with the third case of purely sinusoidal phase current excitation. As previously explained, the core losses were obtained from FE analysis. In the left-most column, the excitation of the FE-modelling is presented and the three columns to the right list the losses in Watt for the three different load cases. The table is divided to show hysteresis losses, eddy current losses, copper losses and inverter losses individually.

As can be seen, the differences in core losses and conduction losses between SPWM and DPWM are small. However, compared to purely sinusoidal excitation, especially the eddy current losses are increased significantly. Furthermore, in [45] the Bertotti-formula and its limitations are investigated for different materials and frequencies. The findings indicate that the accuracy of the formula is questionable, with estimation errors for the material used in this thesis (M270-35A) reaching above 30 percent. However, comparatively, the obtained data is considered representative. Consequently, an increase in core losses when using DPWM cannot be concluded based on the FEM-analysis alone.

Table 5.1: Comparison of core losses and VSI losses for different excitations and load torque obtained from FEM-calculations at 3500 r/min

| | Hysteresis Losses [W] | | |
|---|---|---|---|
| Excitation | 15 Nm | 35 Nm | 55 Nm |
| Current | 104.3 | 131.0 | 145.8 |
| SPWM | 104.7 (+0.5 %) | 131.6 (+0.5 %) | 147.7 (+1.3 %) |
| DPWM | 105.3 (+1.0 %) | 132.2 (+0.9 %) | 149.2 (+2.3 %) |

| | Eddy Current Losses [W] | | |
|---|---|---|---|
| Excitation | 15 Nm | 35 Nm | 55 Nm |
| Current | 57.2 | 70.8 | 84.3 |
| SPWM | 100.1 (+75.0 %) | 114.0 (+61.0 %) | 126.3 (+49.7 %) |
| DPWM | 99.1 (+73.2 %) | 113.5 (+60.3 %) | 126.2 (+49.6 %) |

| | Copper Losses [W] | | |
|---|---|---|---|
| Excitation | 15 Nm | 35 Nm | 55 Nm |
| Current | 19.5 | 85.7 | 189.2 |
| SPWM | 20.0 (+2.4 %) | 85.7 (+0.0 %) | 186.9 (-1.2 %) |
| DPWM | 20.0 (+2.4 %) | 85.6 (-0.1 %) | 187.1 (-1.1 %) |

| | VSI Losses [W] | | |
|---|---|---|---|
| Excitation | 15 Nm | 35 Nm | 55 Nm |
| Current | - | - | - |
| SPWM | 103.5 (± 0 %) | 245.9 (± 0 %) | 373.8 (± 0 %) |
| DPWM | 86.1 (-16.8 %) | 207.6 (-15.6 %) | 321.2 (-14.1 %) |

### 5.3.2 Phase current and acoustic frequency analysis

As a consequence of changing the modulation pattern, the harmonic content of the phase current will be affected. The frequency range of interest is in the vicinity of the switching frequency, covering the most significant switching frequency sideband harmonics. For an automotive application, this frequency range is within the hearable frequency range of the human ear and is usually perceived as disturbing, as discussed by Chai et al. [46]. Moreover, harmonics around twice the switching frequency are affected as well. Although, these do not contribute as significantly to sound quality issues hence improving these by lower their magnitude are of secondary importance.

In Fig. 5.17 and 5.18, the frequency content of the stator vibrations and the radiated acoustic noise are presented, respectively. The data was obtained

experimentally at 3500 r/min with 55 Nm load torque, averaged over the nine accelerometers and the eight microphones. As can be seen, the harmonic content around the switching frequency is magnified as DPWM is used, compared to SPWM. In Table 5.2, the percentage difference of the most significant harmonics, around the switching frequency ($f_s$), in the acoustic noise ($\Delta P$) and the stator accelerations ($\Delta a$) are presented.

Table 5.2: Harmonic analysis of stator acceleration and radiated acoustic noise, comparing SPWM and DPWM at 3500 r/min and $T_e = 55Nm$.

| Harmonic | $\Delta a$ [%] | $\Delta P$ [%] |
|---|---|---|
| $f_s - 5f_0$ | +62.80 | +44.08 |
| $f_s - 3f_0$ | +38.43 | +45.11 |
| $f_s - f_0$ | +49.88 | +50.17 |
| $f_s + f_0$ | +40.48 | +33.58 |
| $f_s + 3f_0$ | +43.22 | +40.68 |
| $f_s + 5f_0$ | +25.17 | +21.95 |

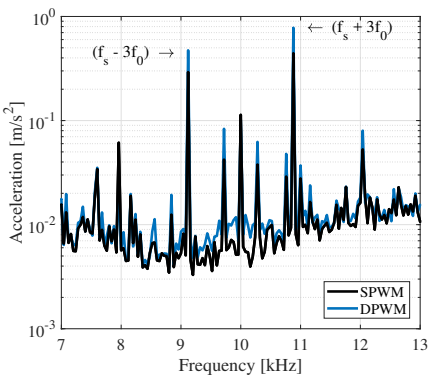


Figure 5.17: Measurements of stator acceleration at 3500 r/min and 55 Nm load. Comparison between SPWM and DPWM.

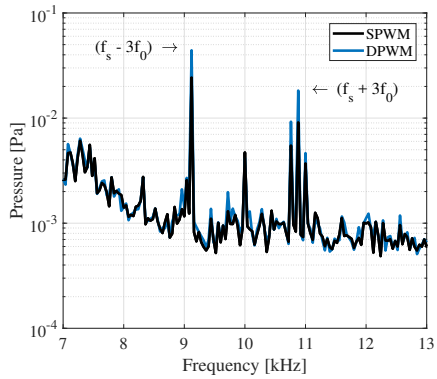


Figure 5.18: Measurements of acoustic pressure at 3500 r/min and 55 Nm load. Comparison between SPWM and DPWM.

In Fig. 5.19 and 5.20 the most significant harmonics around the switching frequency, considered to be the acoustically most relevant harmonics, are presented for the phase current and the radiated acoustic noise. The data was obtained experimentally from rotational speed sweeps from 500 to 6500 r/min at peak torque, with a fix switching frequency of $f_s = 10$ kHz. In the figures, $f_0$ equals the

fundamental frequency. As shown in the figures, DPWM results in a significant increase in the magnitude of the phase current harmonics, which causes the adverse effects on the acoustic performance. Especially below base speed (3500 r/min), the difference in the acoustic noise is evident. Furthermore, the results also indicate that above base speed, the differences are decreased, and occurrence of adverse effects on the acoustic performance is questionable. The results suggest that DPWM does not have any significant impact on the acoustic performance above base speed.

The figures show on the complexity in the dynamics linking phase current harmonics to harmonics in the acoustic emissions. The underlying harmonics in the radial force, acting on the stator teeth, are a result of the flux density squared, according to the Maxwell Stress Tensor. Consequently, the harmonics seen in the acoustic measurements differ from what is seen in the phase current. Moreover, acoustic harmonics, due to stator deformations, are combined results of the forces originating from different phase current harmonics.

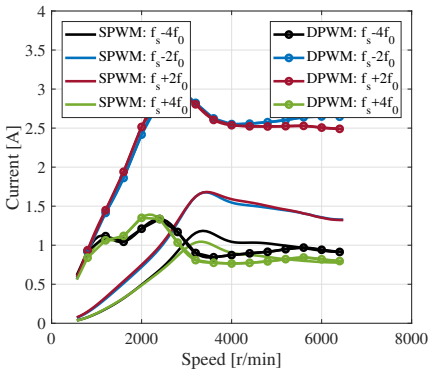


Figure 5.19: Measurements of the most significant harmonics in the phase current for DPWM and SPWM.

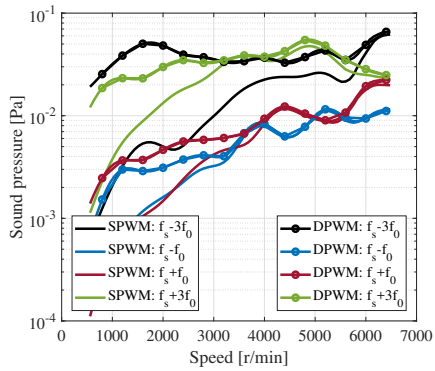


Figure 5.20: Measurements of the most prominent harmonics in the radiated acoustic sound pressure for DPWM and SPWM.

In Fig. 5.19 the most significant phase current harmonics are presented. As can be seen, the magnitude of the presented harmonics for the DPWM case exceeds the SPWM case below base speed. In the field weakening region, the difference between SPWM and DPWM for $f_s \pm 4f_0$ is considerably decreased.

Additionally, the characteristics of the data presented in Fig. 5.19 is in line with findings presented by Tsoumas et al. [38], where the characteristics of the

different harmonics are presented up to unity modulation index.

As previously discussed, randomization of the switching frequency is of interest to decrease the magnitude of the harmonics and ultimately reduce the tonality of the emitted noise, by smearing out the high-frequency harmonic spectra of the force density. The influence of switching frequency randomization on the phase current harmonic sidebands to the switching frequency is studied in Section 5.3.2.

**Influence of switching frequency randomization**

The randomization of the switching frequency is based on a Gaussian distribution with an expected value of $f_s = 10$ kHz and with different levels of variance ($\sigma$), presented in Table 5.3. In the context, the first case of $\sigma = 100$ Hz is by the author considered moderate, whereas the last case with $\sigma = 1000$ Hz is considered to have a rather substantial spread.

Table 5.3: Level of variance for the three cases used in the investigation of randomized switching frequency

| Case [n] | Variance [Hz] |
|---|---|
| 1 | 100 |
| 2 | 500 |
| 3 | 1000 |

In Fig. 5.21 and 5.22 the harmonics around the switching frequency for different levels of randomization are presented for both SPWM and DPWM, respectively. Generally, it can be concluded that even a moderate level of randomization significantly affects the tonality. Tonality is referred to as the difference between the magnitude of harmonics and the overall noise level. Also, the impact of increasing the variance is gradually decreased. The difference when the variance is changed from $\sigma = 500$ Hz to $\sigma = 1000$ Hz is significantly less than for instance the step from $\sigma = 100$ Hz to $\sigma = 500$ Hz.

It is of importance to understand the implications when the switching frequency is randomized. The tonality is decreased, which is seen in decreased magnitudes of the specified harmonics in Fig. 5.21 and 5.22. However, the background noise level is consistently increased with an increased level of randomization. In Fig. 5.23 the phase current is presented, in the frequency interval of 8 to 12

kHz, when DPWM is used both without randomization ($\sigma = 0$) and with two level of randomization ($\sigma = 100$ Hz and $\sigma = 500$ Hz). As the level of randomization increases, the magnitude of the peaks decay, whereas the background noise level is increased. At a level of $\sigma = 1000$ Hz, the noise is comparable with the magnitude of the harmonics themselves. Hence further randomization is without any gain. This case is not presented in Fig. 5.23 for clarity reasons.

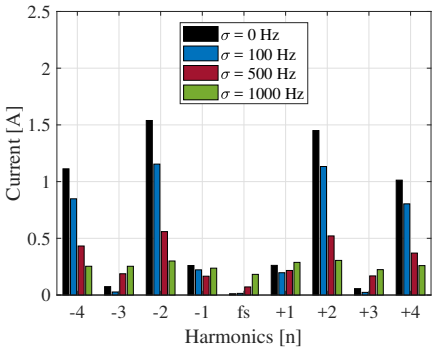


Figure 5.21: Measured phase current harmonics around the switching frequency using SPWM with different levels of randomization at a load torque of 55 Nm at 3500 r/min.

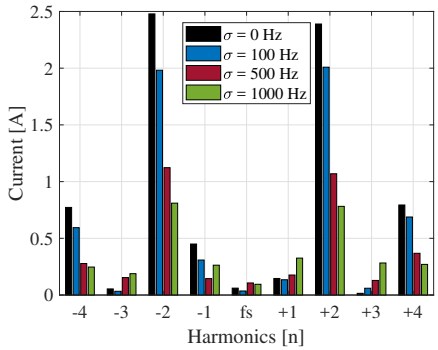


Figure 5.22: Measured phase current harmonics around the switching frequency using DPWM with different levels of randomization at a load torque of 55 Nm at 3500 r/min.

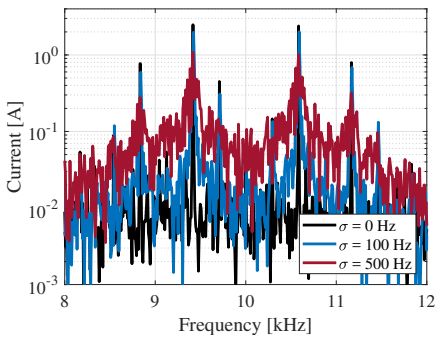


Figure 5.23: Comparison between different levels of randomization using DPWM, the data is obtained from measurements.

Worth noting is that the same behavior is expected in the radiated noise. Although, tonality is not the only measure of sound characteristics and hence not of sound quality. Previous research proclaims that randomization of the switching

frequency is a prominent method to increase the sound quality by harmonic spreading [9, 12, 36, 37, 38, 39], which brings attention to the method.

To conclude, the randomization has favorable results on the tonality of the phase current harmonics. Moreover, the harmonic spread is substantial as the variance is increased towards 1000 Hz, which for the given system is the limit where further randomization does not contribute to any decrease of the harmonics of interest. In Chapter 5.3.3 the randomization of the switching frequency is evaluated from a sound quality perspective by investigating the perceived annoyance.

### 5.3.3 Sound quality assessment

Since voltage modulation has acoustic drawbacks and switching frequency randomization might have a positive impact on the sound quality perception, a directional survey was conducted to explore those relations. For each modulation strategy six sound files, each with a duration of five seconds, were created from rotational speed sweeps from 500 to 7500 r/min at peak torque from microphone #2 (see Fig. 2.4), according to Table 5.4 and 5.5. The purpose of the test was to evaluate the sound quality of components related to a switching frequency of 10 kHz. Therefore, the sounds were modified by a second-order recursive IIR high-pass filter with a cut-on frequency of 6 kHz, to suppress the influence of low vibrational orders and noise from surrounding equipment, such as the DC-machine used as the load.

Table 5.4: List of modulation techniques used for sound quality assessments

| # | Modulation |
|---|---|
| 1 | SPWM 10 kHz (reference) |
| 2 | SPWM 10 kHz, random switching frequency ($\sigma = 500$ Hz) |
| 3 | SPWM 10 kHz, random switching frequency ($\sigma = 1$ kHz) |
| 4 | DPWM 10 kHz |
| 5 | DPWM 10 kHz, random switching frequency ($\sigma = 500$ Hz) |
| 6 | DPWM 10 kHz, random switching frequency ($\sigma = 1$ kHz) |

The objective was to determine whether different modulation techniques alter the perceived annoyance caused by high-frequency tones. Sounds recorded from the PMSM drive using different modulation techniques (number 2 to 6 in Table 5.4) were compared to a reference sound (number 1 in Table 5.4) recorded from the PMSM drive using SPWM with a fixed switching frequency of 10 kHz.

Table 5.5: Rotational speed sweep segments included in the sound quality assessment

| Speed | Interval [s] | Speed range [r/min] |
|---|---|---|
| 1 | 0-5 | 500-1090 |
| 2 | 10-15 | 1680-2280 |
| 3 | 20-25 | 2870-3470 |
| 4 | 30-35 | 4070-4670 |
| 5 | 40-45 | 5260-5860 |
| 6 | 50-55 | 6440-7040 |

**Listening tests - method**

A total of 18 subjects participated, six women and 12 men. All were volunteers. The mean age was 24 years (standard deviation 3.6 years), and all subjects had a self-reported normal hearing. The sounds were reproduced through calibrated headphones (Head Acoustics PEQ V amplifier and Sennheiser HD600 headphones).

The test was based on the Multi Stimulus test with Hidden Reference and Anchor (MUSHRA) developed by the International Telecommunication Union [47]. The method was developed for audio reproduction where an unprocessed signal with full bandwidth may be used as the reference when the quality of processed or transmitted signals is evaluated. In the MUSHRA, the full bandwidth signal is used both as a known and a hidden reference. This means that the subjects at any time during the evaluation can listen to the reference and that the reference also is hidden among the remaining stimulus. In this study, the SPWM 10 kHz recording served as the reference sound and all other stimulus were to be compared to this reference. The MUSHRA approach is most appropriate for evaluating medium or large impairments. This makes the method suitable for evaluating differences caused by the use of different modulation techniques and different levels of switching frequency randomization.

In the MUSHRA, anchors are used to indicating how the systems under test compare to well-known distortions [47]. Because the objective was to compare sounds from the PMSM drive with different modulation techniques, no conventional anchors existed and were therefore not included. As a result, the method was modified into a Multi Stimulus test with Hidden Reference (MUSHR) [48]. In the MUSHR, the subjects were asked to judge the differences in annoyance for the sounds compared to the reference (i.e. SPWM) where 0 indicated no difference

in annoyance, 100 indicated much more annoying and -100 indicated much less annoying. Only the stimulus that the subject thought was the hidden reference stimulus was given the value 0. For all other stimuli, the difference from the reference was judged on the scale ranging from -100 to 100. The subject controlled the listening test through a computer interface, shown in Fig. 5.24.

The analysis of the listening test results started with finding out how many of the subjects that could identify the hidden reference stimulus (SPWM 10 kHz) from the object stimuli (recordings of modulation techniques 2-6 in Table VI). This indicated how similarly the stimuli were perceived. A Repeated Measures ANOVA was conducted to determine if the sound emitted during use of the different modulation techniques were perceived differently.

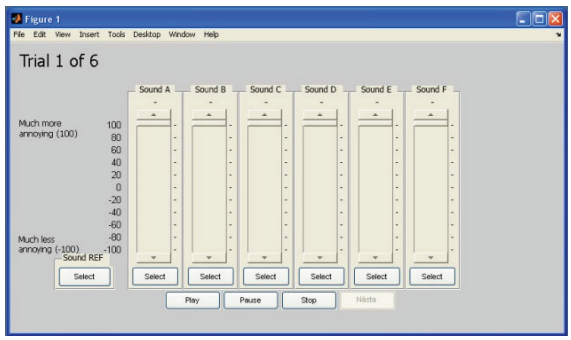


Figure 5.24: User interface used for listening test.

**Listening tests - results**

The number of times each stimulus was judged as being the reference stimulus is shown in Table 5.6. From these results, it is obvious that at lower rotational speeds most subjects easily identified the reference. At the highest rotational speed, the differences between the stimuli (the different modulation techniques) became almost indistinguishable. This can be seen by the vast spread of what was perceived as the reference in the last and second to last rows in Table 5.6.

A Repeated Measures ANVOVA was made to check whether there were significant ($p < .05$) differences in perceived annoyance between the different modulation techniques. In order words, if the grading of the perceived annoyance varied significantly between the subjects. The objective of the test is to determine whether the differences indicated by the subjects can be statistically ensured.

Table 5.6: Number of times each stimulus was judged as being the reference stimulus

| Speed[2] | SPWM | SPWM 500 Hz | SPWM 1 kHz | DPWM | DPWM 500 Hz | DPWM 1 kHz |
|---|---|---|---|---|---|---|
| 1 | 18 | 0 | 0 | 0 | 0 | 0 |
| 2 | 16 | 2 | 0 | 0 | 0 | 0 |
| 3 | 15 | 3 | 0 | 0 | 0 | 0 |
| 4[1] | 13 | 2 | 0 | 1 | 1 | 0 |
| 5[1] | 9 | 0 | 5 | 2 | 1 | 0 |
| 6[1] | 3 | 1 | 3 | 4 | 1 | 5 |

[1] For each of these conditions one subject missed to mark one of the stimuli as being the reference stimulus

[2] Rotational speed sweep segments defined in Table 5.5.

Mauchly's Test of Sphericity was used to check whether the assumption of sphericity, one of the underlying assumptions for Repeated Measures ANOVA, had been violated. Sphericity refers to the condition that the variance of the difference of the subject's answers is all equal. If the variance of the difference between all combinations of the subject's answer, for each of the speed intervals, are roughly equal, the assumption of sphericity is not violated.

The ANOVA results show that there were significant differences in annoyance assessments between the different modulation techniques for all speed ranges, except for the highest speed segment. This is further discussed in Paper III.

The mean annoyance is represented in Fig. 5.25. Note that the data is interpolated based on data from the six rotational speed sweep segments, seen in Table 5.5, for each combination of modulation technique and randomization. The peak torque is indicated to give further understanding of the rotational speed and appearance of the field weakening region. The figure is further discussed in the following section.

**Interpretation of listening tests results**

From the data, three conclusions can be drawn. Firstly, the perceived annoyance is higher for DPWM compared to SPWM for the first three speed segments. For the last three speed segments, the differences are generally small.

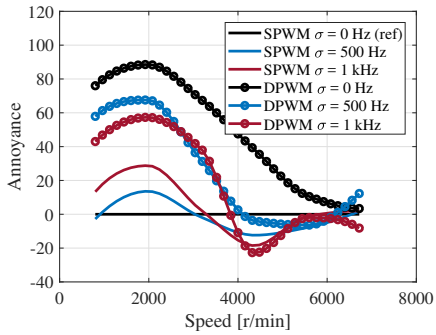


Figure 5.25: Perceived annoyance from acoustic listening test for the different modulation techniques. The data is interpolated based on the six speed cases presented in Table 5.5.

Secondly, up until field weakening, randomization of the switching frequency has a positive influence on sound quality for the DPWM samples. In most DPWM cases for these four-speed segments, the 1 kHz randomization provides less annoyance than the 500 Hz variance. This is coherent with the impression from the visual inspection of Fig. 5.26 where a large number of prominent tonal components are being smeared out when using randomization, yielding a more broadband spectrum. Although, Fig. 5.25 indicates that the change in variance from zero to 500 Hz has a larger impact than the step from 500 to 1000 Hz. This is clearly seen at low rotational speeds in Fig. 5.25. Hence one can argue that randomization of the switching frequency is beneficial in the case of DPWM. However, further increasing the level of randomization does not necessarily improve the acoustic sensation substantially and as a tool, it is not unanimously improving the situation, which can be seen for the SPWM cases.

Lastly, in the field weakening region, there were no statistically significant differences in perceived annoyance between the sound samples. This is coherent with the impression from the visual inspection of Fig. 5.27 where no significant differences between the spectra can be observed. Note that the noise in that particular segment does not relate to the switching process itself. The broadband noise originates from the surroundings, possibly from equipment such as the speed reducer and the brake-machine.

Moreover, data presented in Fig. 5.26 agree with the theory in Chapter 3 and Fig. 5.19 where the current harmonics with highest magnitude for the given rotational speed are presented.

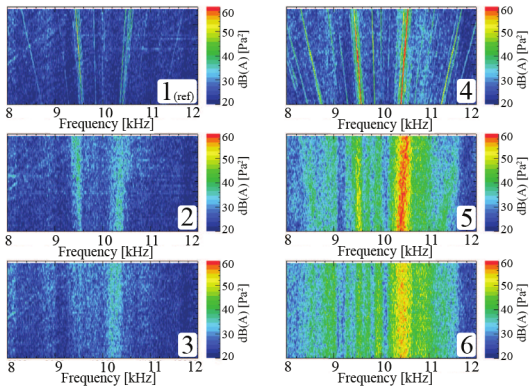


Figure 5.26: Autopower noise spectrum for the six modulation techniques, speed segment 2.

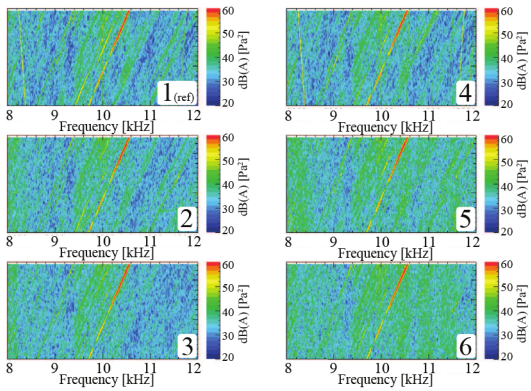


Figure 5.27: Autopower noise spectrum for the six modulation techniques, speed segment 6.

The results are to a certain degree expected based on previous publications - For DPWM, randomization is positive with respect to the sound character and DPWM has a more unpleasant spectrum compared to SPWM. Interestingly, there was almost an opposite trend by increasing the amount of randomization for the SPWM samples. These conclusions gave rise to further questions, as *which factors or metrics contribute to the perceived annoyance?* This is essential to understand and to be able to set objective requirements for ensuring acoustic pleasantness. Previous publications where this topic has been explored for electric motor whining noise are [49, 50, 51].

Thorough examinations of Pearson correlations between established standard metrics as well as psycho-acoustic metrics and the annoyance ratings were conducted. Besides, multiple linear regression analyses including two-way interactions and quadratic terms were performed to investigate to what extent annoyance could be modeled by combining the available metrics. The squared correlation coefficient from the multiple regression analyses and the metrics having a correlation coefficient $r$, $-.5 > r > .5$ is tabulated in Table 5.7. From the statistical explorations, the following conclusions were drawn:

- Different variants of sharpness, loudness (Zwicker-method according to ISO532B, Stevens mark VII-method) and the overall sound pressure level (SPL) are very highly correlated. This is rather expected due to the 6 kHz HP-filter applied to the samples.
- Among the available metrics for tonal exposure, tonality is most suitable for quantifying inverter-related tonal components. Prominence ratio (PR) and tone-to-noise ratio (TNR) need to be handled with care since the number of components around the switching frequency and the degree of randomization heavily will impact those metrics.
- The level-oriented metrics (loudness, SPL and sharpness) have the largest impact on the perceived annoyance and this confirms to some extent the findings by Bassett et al. [49] and Fingerhuth [51]. However, tonality did not contribute substantially in explaining the variance in the data. This concludes that there are one or more dimensions in the nature of the sounds that cannot be captured with established sound quality metrics.

Table 5.7: Squared correlation coefficients from multiple regression and correlation coefficients for the variables having the largest weights in the model

| Segment | $R^2$ | Metrics |
|---|---|---|
| 1 | 54.7 % | sharpness ($r$ = .70), SPL (.68) |
| | | loudness Zwicker FF ($r$ = .66), roughness (-.53) |
| 2 | 77.7 % | SPL ($r$ = .85), sharpness (.85), tonality (.54) |
| | | loudness Zwicker FF (.84), roughness (-.68) |
| 3 | 55.3 % | sharpness ($r$ = .67), tonality (.53), SPL (.51) |
| 4 | 29.8 % | tonality ($r$ = .53) |

### 5.3.4 Conclusions

The work presented has contributed to reducing the knowledge gap concerning the influence of VSI modulation strategies on energy saving and acoustic pleasantness. The test object for the case study was a PMSM drive which is currently in production in a mass-produced hybrid/electric vehicle. The main finding was that for representative rotational speed sweeps amounted to switching frequency, torque and speed range, a decrease of total inverter losses reached 17% with DPWM compared to the reference modulation strategy, SVM, for a significant speed range without degrading the acoustic comfort.

Randomizing the switching frequency with a bandwidth of 5% of the switching frequency was essential for DPWM to achieve this with respect to sound quality. Furthermore, advantages of randomization of the switching frequency are not unanimous. For SVM, no improvements with respect to audible noise were observed despite the smearing of the spectra. This implicates that claims such as that acoustic pleasantness automatically is improved if the spectra changes from tonal to more broadband, as often encountered in literature, are unsubstantiated and doubtful. These conclusions were drawn from statistical analyses of the rating results of the perceived annoyance during subjective assessments of the noise character in controlled listening environments. Further explorations of acoustic metrics are however needed to obtain robust prediction models for the perceived annoyance due to the signature of the inverter-specific tonal components.

In addition, the FEM-analysis showed that the choice of modulation technique did not significantly influence eddy current and hysteresis losses. Moreover, analytical expressions of the airgap radial flux density and force density harmonics were investigated. The findings show that the high-frequency harmonics in the flux density and the force density harmonics can be analytically determined, based on the harmonic content of the phase current.

To conclude, sophisticated methods such as varying the modulation technique and introducing different degrees of randomization at different rotational speeds can enable optimization of electric drive efficiency and performance as well as the acoustic pleasantness.

Further analyses and discussions on the subject of modulations techniques influence on inverter losses and acoustic sound quality are given in Paper I, III and V.

# Electric machine control

Electric machine control is a well-developed research area. Yet, new applications and emerging technologies, in combination with ever increasing computational power, adds possibilities to stretch that research further. The context of machine control does not only cover reference tracking problems but also parameter estimation. In this chapter, firstly the modeling of the PMSM is described. Thereafter, the standard Field Oriented Control (FOC) approach is presented. This solution was used throughout the work, and it was also used as a benchmark for the second machine control solution, the finite control set model predictive control (FCS-MPC). The FCS-MPC is an optimization-based, direct control approach. Thereby, it does not employ PWM but instead controls the switching states directly, by solving an optimization problem in real-time. Lastly, a sensorless control solution is presented. It shares similarities with the FCS-MPC, but rather than controlling the machine it estimates the rotor position angle allowing for motion sensorless control.

## 6.1 Drivesystem and PMSM modelling

### 6.1.1 Equivalent circuit model

The mathematical model of a salient-pole PMSM in the synchronous reference frame can be presented with the circuit equivalent model shown in Fig. 6.1 where $L_d$ and $L_q$ are the inductances in the direct and quadrature direction, $u_d$ and $u_q$ are the dq-stator voltages, $i_d$ and $i_q$ are the dq-current, $R_s$ is the stator resistance, $\omega_r$ is the electrical rotor speed, and $\Psi_m$ is the flux linkage originating from the

magnets, respectively [34].

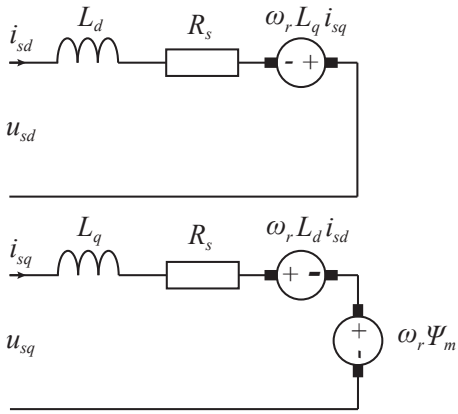


Figure 6.1: Equivalent circuit for the PMSM in the dq-reference frame.

The stator equations, representing the relations between stator voltage and phase current can be expressed as

$$L_d \frac{di_d}{dt} = u_d - R_s i_d + \omega_r L_q i_q \tag{6.1}$$

$$L_q \frac{di_q}{dt} = u_q - R_s i_q - \omega_r \left( L_d i_d + \Psi_m \right) \tag{6.2}$$

based on the illustration in Fig. 6.1. The flux linkage, as function of inductance and current, is expressed as

$$\Psi_d = L_d i_d + \Psi_m \tag{6.3}$$

$$\Psi_q = L_q i_q \tag{6.4}$$

The expression for the electromagnetic torque can be written as [34]

$$T_e = \frac{3 n_p}{2} \left( \Psi_d i_q - \Psi_q i_d \right) \tag{6.5}$$

where $n_p$ is the number of pole pairs.

In this model representation only fundamental components are included, without any secondary effects such as harmonics in the induced voltage. Neither

variations in $L_d$, $L_q$, and $\Psi_m$ are considered. Variations depending on $i_d$ and $i_q$ occurring due to magnetic saturation in the iron material. Due to cross saturation, $L_d$ is not only affected by $i_d$, and $L_q$ is not only affected by $i_q$ [19].

### 6.1.2 Maximum torque per ampere with variable inductances

In (6.5) the electromagnetic torque equation is presented. As the equation describes, the torque is a function of both $i_d$ and $i_q$. Consequently, different combinations of these can be used to obtain the same torque. The maximum torque per ampere (MTPA) approach was used for all simulations and all experimental testing, to achieve a high energy efficient drive system. For a given torque reference, the selection of $i_d$ and $i_q$ references was based on minimization of the RMS current. Variations in $L_d$, $L_q$ and $\Psi_m$ were considered as functions of both $i_d$ and $i_q$, which adds additional complexity. The maximum torque per ampere strategy was obtained by solving the following minimization problem

$$\begin{aligned} minimize \quad & f_0(i_d, i_q) \\ s.t. \quad & f_i(i_d, i_q) \leq 0 \\ & h_i(i_d, i_q) = 0 \end{aligned} \tag{6.6}$$

where

$$\begin{aligned} f_0(i_d, i_q) &= \sqrt{i_d^2 + i_q^2} \\ f_i(i_d, i_q) &= \sqrt{u_d(i_d, i_q)^2 + u_q(i_d, i_q)^2} - \frac{V_{dc}}{\sqrt{3}} \\ h(i_d, i_q) &= 1.5 n_p i_q \left[\Psi_m(i_d, i_q) + \left(L_d(i_d, i_q) - L_q(i_d, i_q)\right) i_d\right] - T_{e,ref} \end{aligned} \tag{6.7}$$

where $u_d(i_d, i_q)$ and $u_q(i_d, i_q)$ are calculated using the stator equations in steady state, described in (6.1) and (6.2) for the direct and quadrature axes, respectively. The objective function, $f_0$, equals the RMS phase current. The inequality constraint, $f_i(i_d, i_q)$, acts as voltage limitation. When this is active, field weakening is required. Lastly, the equality constraint, $h(i_d, i_q)$, defines the electromagnetic torque function which is also found in (6.5).

The problem definition implies that for each combination of torque and speed, there is a combination of $i_d$ and $i_q$ that minimizes the phase current RMS value, which aims to minimize the resistive losses in the inverter and the

machine. The trajectory obtained by this approach is not optimum in a global sense, improvements can be made by extending the problem by including, for instance, iron losses in the machine following the research presented by Meifen et al. [52]. However, the selection of only minimizing the RMS value of the phase current is considered to be a reasonable trade-off between efficiency-enhancing measures and time invested in the development of the optimization algorithm. Furthermore, during loading the copper losses are the most significant loss component in the drive system [53], also motivating the selected solution approach.

The variation in $L_d$, $L_q$ and $\Psi_m$ adds an additional degree of complexity, since these are not constants in (6.6) and (6.7). Therefore, the solution for all combinations of torque and rotational speeds are calculated offline and further implemented in the control system by the use of look-up tables.

In Fig. 6.2 the electromagnetic torque is presented as a function of $i_d$ and $i_q$. The rightmost edge of the colored area, which is indicated with the solid red line, gives maximum torque per ampere under the assumption that the rotational speed is below base speed, $\omega_e < \omega_b$. If the rotational speed exceeds the base speed, the inequality constraint $f_i(i_d, i_q)$ becomes active. As a consequence, the dq-current reference values will deviate from the MTPA-line. At such instances, $i_q$ is decreased and $i_d$ is increased in the negative direction to maintain the reference torque.

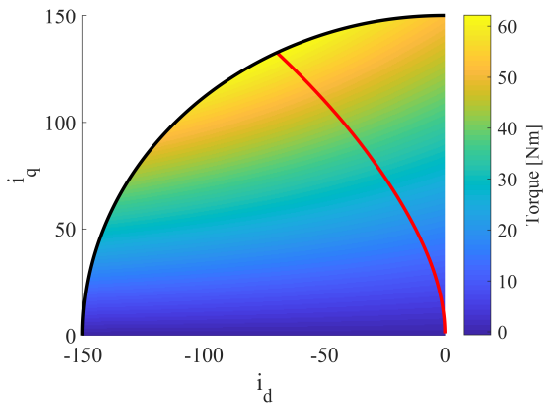


Figure 6.2: Electromagnetic torque as function of $i_d$ and $i_q$, obtained from FEM-calculations

## 6.2 Field oriented control

The FOC method is comprised of a speed controller cascade coupled with an inner current controller. The controllers were derived using the internal model control (IMC) strategy [34] and implemented using the synchronously rotating reference frame (dq-reference frame). For the dq-current, two parallel controllers were used where the d- and the q-component were controlled separately. This was enabled by decoupling the d and q axes from each other by feed-forwarding of the coupling terms. These are the parts of the stator equation where $i_d$ influences $i_q$ and vice versa. For enhanced performance, features such as anti-windup and active damping were implemented.

By feed-forwarding, the back-emf and the coupling term, the PMSM model stator current relation in the q-direction can be rewritten as

$$L_q \frac{di_q}{dt} = u_q - R_s i_q - \omega_r \left(L_d i_d + \Psi_m\right) + \omega_r \left(\hat{L}_d i_d + \hat{\Psi}_m\right) \tag{6.8}$$

where $\hat{L}_d$ and $\hat{\Psi}_m$ are estimated values of $L_d$ and $\Psi_m$, respectively. Assuming perfect parameters, i.e., $\hat{L}_d = L_d$ and $\hat{L}_q = L_q$, the following transfer function is obtained

$$G(S) = \frac{u_q(S)}{i_q(S)} = \frac{1}{sL_q + R_s}. \tag{6.9}$$

By defining the closed-loop system for the current controller as a low-pass filter with the bandwidth $\alpha_c$ the closed-loop system is defined as

$$G_{cl}(S) = \frac{F(S)G(S)}{1 + F(S)G(S)} = \frac{\alpha_c}{s + \alpha_c}. \tag{6.10}$$

The q-controller, $F_q(S)$, then becomes

$$F_q(S) = K_{pc} + \frac{K_{ic}}{s} = \frac{\alpha_c}{s} G(S)^{-1} = \alpha_c L_q + \frac{\alpha_c R_s}{s}. \tag{6.11}$$

The same procedure is used to derive the parameters for the d-current controller and the speed controller. In Fig. 6.3 the control system is illustrated. It is a closed loop system where the phase current and the rotor position are measured. The rotational speed of the machine is estimated using an estimator based on the phase lock loop (PLL) principle.

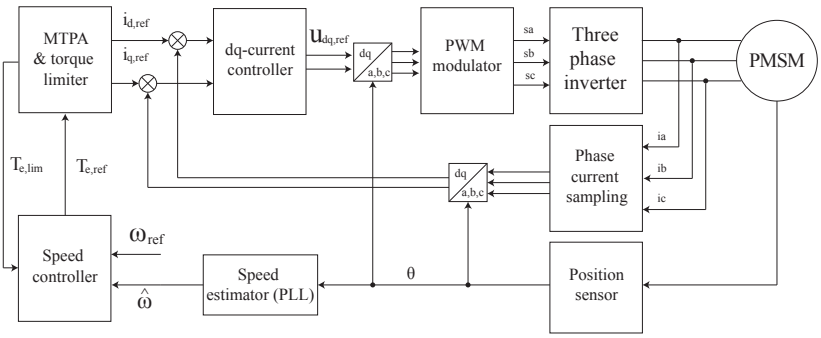


Figure 6.3: Illustration of the PMSM control system.

## 6.3 Model predictive current control

Model predictive control (MPC) has increasingly become an area of attention for power electronics applications [54, 55]. It is an emerging control method for a vast amount of applications. Applications including the field of electric drives where the subcategory of direct, or finite control set (FCS), MPC is a promising contender [56]. With the inverter states as manipulated variables, constrained to belong to an integer finite set, the direct MPC is a solution method which solves the current tracking and modulator problem in one computational step. The direct approach renders the subsequent pulse width modulation excessive, which is interesting from many perspectives [57, 58, 59, 60, 61]. Furthermore, the framework of MPC also eases the inclusion of nonlinearities and input constraints [55].

A significant disadvantage affiliated with nonlinear integer MPC problems is the computational challenge to solve the underlying problem in real-time, with a sufficiently high update frequency. The NP-hardness of the problem yields a complexity which grows exponentially with the length of the prediction horizon and the number of decision variables [56]. Thereby, the computational requirement aspects are indeed interesting.

An interesting FCS-MPC solution is given in [56]. The proposed solution incorporates an infinite horizon tail cost of the MPC problem formulation to maintain good performance while shortening the prediction horizon.

In the research presented in [57] and [58], Geyer *et. al* thoroughly process the subject of FCS-MPC for multi-level inverters. The research highlight benefits such as the rapid response and lower current total harmonic distortion (THD),

while consistently examines the impact of the different tuning variables. Variables, such as different horizon lengths, the impact of weighting factor on the switching effort and different update frequencies. Primarily, the tailored sphere decoding algorithm is in focus to improve the performance by reducing the computational burden. Yet, the derivation of the initial unconstrained solution, which also is of importance in real-time implementations, is partially overlooked in favor of the sphere decoding part of the solution.

Similarly, in [59, 62] the sphere decoding aspects are primarily targeted to reduce the computational complexity, by minimizing the number of examined nodes, given the optimal unconstrained solution.

In [63], a comparison between FCS-MPC and PI-PWM solutions for a five-phase induction machine is given. Interesting findings are presented regarding steady state and transient dynamics. The results show on the superiority at transients for the FCS-MPC solution researched. However, the research is limited to a single horizon length (two-step prediction) and without explicitly considering inverter losses. Further, the reasonably moderate MPC update frequency of 10 kHz is also believed to be a limiting factor in the search for performance. In [64], a similar comparison is given, where three different MPC schemes are evaluated for a five-phase inverter, two induction motor-configuration. Computational requirements are minimized by cleverly reducing the domain of possible optimal switching state candidates to be evaluated at every time step. Despite the high research quality and the interesting findings, it is based on a brute-force approach. An approach which fundamentally differs from the method proposed in this manuscript.

To the author's knowledge, much of the research on the subject is related to multi-level inverters. Often in the context of induction machine drives [56, 65], and references therein. In the fields of variable PMSM drives with 2-level inverters, with high rotational speeds and fundamental frequencies, the author acknowledges the amount of research as sparse [65]. On the subject of predictive control of PMSM-drives, different solutions have been evaluated [65, 66, 67, 68]. In [65], three different prediction control schemes are thoroughly examined and evaluated. Although the impeccable research and the interesting results, the assessed approaches differ from what is proposed in this manuscript. The inherent horizon length of one and the lack of a penalty on switching effort, as in [65, 66], is contradicted by the research presented in, for instance, [58] and [69]. Research that argues that the switching frequency can be reduced, and noise sensitivity issues can be remedied

by extending the horizon above one.

There is an interesting research gap for FCS-MPC for high fundamental frequency machines, typically operating with PWM switching frequencies above 8-10 kHz. This, due to the inherent computational requirements on the algorithms to allow for controller update frequencies above a couple of tens of kHz, while utilizing an extended horizon to accommodate long horizon benefits [58, 69]. In essence, a need for further computational complexity reduction.

The scientific contribution of this work builds further on the findings of [57, 58, 59, 60] and is primarily in the improvements of the computational requirements of the controller - A highly relevant research topic within the field of predictive control in general, and for drives applications in particular. The suggested improvements resulted in a decreased turnaround time of roughly 40 % for a horizon length of $N = 4$. This improvement is obtained by an alternative optimization problem setup where the problem at hand, stretched across a finite horizon, essentially is defined backward. This results in reduced complexity which enables more computationally-efficient matrix calculations when deriving the initial unconstrained optimum at each iteration. An initial optimal solution, which was then used in the iterative search for the integer constraint optimal solution.

Moreover, further contributions are within the analysis of the MPC-solver, including its tuning parameters (horizon length, update frequency, and weighting factors), as well as the acoustic sound performance assessment. The tuning parameters are evaluated using inverter efficiency, phase current harmonics and acoustic measures. The controller scheme is implemented in a real-time environment and assessed experimentally.

This work is in detail described in Paper VII. Hence the extent of the following problem formulation and the underlying mathematical formulations are only given in an abbreviated version.

### 6.3.1 Problem formulation

The proposed solution approach for the finite control set MPC, is to first solve the optimization problem analytically, without considering the integer constraints on the inverter switches. Thereafter, utilizing a branch-and-bound method known as Sphere decoding [59] to search the neighboring hyper-sphere for the optimum solution. A solution approach previously seen in for instance [57] and [70].

Essentially, the primary objective is to solve a current reference tracking problem along a pre-defined horizon. The aim is to solve the problem while incorporating the cost of altering the states in the inverter. The current controller is tunable with three variables; the selection of horizon length, switching effort penalty weight as well as the update frequency of the controller. Based on the selection, the controller characteristics can be tailored to a given application. Their influence on the inverter efficiency, the current harmonics and the acoustic performance of the machine is further evaluated in Paper VII.

A somewhat intuitive approach is to define a cost function combining current reference tracking error and penalties for switching the inverter states. The former is to fulfill the primary objective of reference tracking, whereas the latter incorporated switching effort penalty is introduced to reduce (or control) the energy losses in the switches. The difference in scientific majorities is handled by adding a weighting term $\lambda_u$ to adequately scale the two parts. The cost function to be minimized can be summarized as,

$$\begin{aligned} J &= \sum_{k=t}^{t+N} (1-\lambda_u) \underbrace{\left\|\Delta\vec{i}_{dq}(k+1)\right\|_2^2}_{\substack{\text{Reference current} \\ \text{tracking deviation}}} + \lambda_u \underbrace{\left\|\Delta\vec{u}(k)\right\|_2^2}_{\substack{\text{Penalty on} \\ \text{switching effort}}} \\ &= (1-\lambda_u)\left\|J_1\right\|_2^2 + \lambda_u \left\|J_2\right\|_2^2 \end{aligned} \tag{6.12}$$

where

$$\begin{aligned} \Delta\vec{i}_{dq}(k+1) &:= \vec{i}_{dq}(k+1) - \vec{i}^{*}_{dq}(k+1) \\ \vec{u}(k) &:= \vec{u}_{abc}(k) - \vec{u}_{abc}(k-1) \end{aligned} \tag{6.13}$$

where the summation in (6.12) extends across the horizon, of length $N$.

### 6.3.2 Integer Quadratic Programming Formulation

As previously discussed, a two-step solution approach was used - Firstly, the optimal unconstrained solution is determined analytically, and secondly, the neighboring hyper-sphere of the unconstrained solution is searched iteratively for the optimum solution fulfilling the integer constraint on the switching states.

By evolving (6.12), $J_1$ and $J_2$ can be expressed as,

$$\begin{aligned} J_1 &= \mathbf{\Gamma}\vec{x}(k) + \mathbf{\Upsilon}\vec{U}(k) + \mathbf{\Psi} - \vec{Y}(k) \\ J_2 &= \mathbf{S}\vec{U}(k) - \mathbf{E}u(k-1) \end{aligned} \tag{6.14}$$

where, for $N = 4$, the matrices takes the following form,

$$\mathbf{\Gamma} = \begin{bmatrix} \mathbf{CA}^N \\ \mathbf{CA}^3 \\ \vdots \\ \mathbf{CA} \end{bmatrix}, \quad \mathbf{S} = \begin{bmatrix} \mathbf{I} & -\mathbf{I} & 0 & 0 \\ 0 & \mathbf{I} & -\mathbf{I} & 0 \\ \vdots & 0 & \mathbf{I} & -\mathbf{I} \\ 0 & \dots & 0 & \mathbf{I} \end{bmatrix}, \quad \mathbf{E} = \begin{bmatrix} 0 \\ \vdots \\ 0 \\ \mathbf{I} \end{bmatrix} \tag{6.15}$$

$$\mathbf{\Upsilon} = \begin{bmatrix} \mathbf{CBP_{k+3}} & \mathbf{CABP_{k+2}} & \mathbf{CA^2BP_{k+1}} & \mathbf{CA^3BP_k} \\ 0 & \mathbf{CBP_{k+2}} & \mathbf{CABP_{k+1}} & \mathbf{CA^2BP_k} \\ \vdots & 0 & \mathbf{CBP_{k+1}} & \mathbf{CABP_k} \\ 0 & \dots & 0 & \mathbf{CBP_k} \end{bmatrix} \tag{6.16}$$

$$\begin{aligned} \vec{U}(k) &= \begin{bmatrix} u(k+N-1) & \dots & u(k+1) & u(k) \end{bmatrix}^T \\ \vec{Y}(k) &= \begin{bmatrix} y(k+N) & \dots & y(k+2) & y(k+1) \end{bmatrix}^T \end{aligned} \tag{6.17}$$

There are two important remarks to highlight: Firstly, note the different $\mathbf{P}$-matrices for each column of $\mathbf{\Upsilon}$, which is a result of the forward simulation of the rotational angle in each time step. Secondly, note the reverse order of the problem definition, e.g., that the first index holds the last values, and vice versa.

By evolving the two Euclidean norms, the following expression can be obtained,

$$J = c + 2\mathbf{\Theta}^T \vec{U}(k) + \left\| \vec{U}(k) \right\|_{\mathbf{Q}}^2 \tag{6.18}$$

where

$$\begin{aligned} c &= (1-\lambda_u) \left\| \mathbf{\Gamma}\vec{x}(k) + \mathbf{\Psi} - \vec{Y}(k) \right\|_2^2 + \lambda_u \left\| \mathbf{E}u(k-1) \right\|_2^2 \\ \mathbf{\Theta}^T &= (1-\lambda_u) \left( \mathbf{\Gamma}\vec{x}(k) + \mathbf{\Psi} - \vec{Y}(k) \right)^T \mathbf{\Upsilon} - \\ &\quad \lambda_u \left( \mathbf{E}u(k-1) \right)^T \mathbf{S} \\ \mathbf{Q} &= (1-\lambda_u)\, \mathbf{\Upsilon^T \Upsilon} + \lambda_{\mathbf{u}} \mathbf{S^T S} \end{aligned} \tag{6.19}$$

By defining the problem formulation as the *argument minima*, rather than the *global minima*, the optimum solution is not affected by terms in the cost function which does not contain the optimization variable. Conclusively, additional terms (not including the switching states) can be either added or removed without affecting the outcome. Since $\mathbf{Q}$, by definition, is symmetric and positive definite

the following term, $c_2 = \mathbf{\Theta}^T\mathbf{Q}^{-1}\mathbf{\Theta}$, can be added to the cost function, which enables the following representation

$$J = c + c_2 + \left(\vec{U}(k) + \mathbf{Q}^{-1}\mathbf{\Theta}\right)^T \mathbf{Q}\left(\vec{U}(k) + \mathbf{Q}^{-1}\mathbf{\Theta}\right) \tag{6.20}$$

Note that neither $c$ nor $c_2$ is dependent on the inverter states within the horizon. Hence, these terms are rejected as the augmented minimum is to be found. The unconstrained solution (without considering the constraints on the switching states) are

$$\vec{U}_{unc} = -\mathbf{Q}^{-1}\mathbf{\Theta} \tag{6.21}$$

which leads to the following optimization problem formulation

$$\begin{aligned}\vec{U}_{opt}(k) =& \underset{\vec{U}(k)}{\arg\min}\ \left(\vec{U}(k) + \vec{U}_{unc}\right)^T \mathbf{Q}\left(\vec{U}(k) + \vec{U}_{unc}\right) \\ =& \underset{\vec{U}(k)}{\arg\min}\ \left\|\mathbf{H}\vec{U}(k) - \mathbf{H}\vec{U}_{unc}(k)\right\|_2^2\end{aligned} \tag{6.22}$$

by Cholesky decomposition of $\mathbf{Q}$ as,

$$\mathbf{H}^T\mathbf{H} = \mathbf{Q} \tag{6.23}$$

where $\mathbf{H}$ is upper triangular.

Since the problem to start with, somewhat precariously, is defined backwards, e.g., that the first index holds the last values, and vice versa, the presented Cholesky decomposition is viable. If the problem would have been defined as one typically do, as in [60, 59, 57], it would not have been mathematically possible to determine the (in that case) lower triangular decomposition $\mathbf{H}$ without calculating the inverse of the dense matrix $\mathbf{Q}$. An inverse, which would have been the single most computationally intense operation. Furthermore, since the matrix $\mathbf{H}$ is readily determined, the unconstrained solution (involving the inverse of $\mathbf{Q}$) multiplied with $\mathbf{H}$ can be efficiently calculated as

$$\begin{aligned}\mathbf{H}\vec{U}_{unc} =& -\mathbf{H}\mathbf{Q}^{-1}\mathbf{\Theta} \\ =& -\mathbf{H}\left(\mathbf{H}^T\mathbf{H}\right)^{-1}\mathbf{\Theta} \\ =& -\mathbf{H}^{-T}\mathbf{\Theta} \\ :=& \vec{U}_{unc}\end{aligned} \tag{6.24}$$

which completely removes the need to invert $\mathbf{Q}$.

In summary, by defining the optimization problem backwards, the operations of

- inverse of the dense matrix $\mathbf{Q}$,
- Cholesky factorization of dense matrix $\mathbf{Q}^{-1}$,
- inverse of the triangular matrix $\mathbf{H}^{-1}$

is replaced by

- Cholesky factorization of dense matrix $\mathbf{Q}$
- inverse of the triangular matrix $\mathbf{H}$

which is proven to reduce the computational turnaround time of the entire MPC-solver by approximately 40 % for $N = 4$.

An important remark is that the backward problem formulation does not affect the outcome. Choosing a traditional forward formulation or the proposed backward formulation does not change the problem at hand, i.e., the optimum solution for the former equals the optimum solution for the latter. Consequently, it is excessive to evaluate both since the results would be the same for both (apart from the computational needs). Further, the turnaround time improvements lie in the solution approach where fewer computations are needed to derive the initial unconstrained optimum and the matrices required in the sphere decoding algorithm.

### 6.3.3 Assessment

In Fig. 6.4, the turnaround time is presented for different horizon lengths for the FCS-MPC solver. The solid lines show the mean TAT for the complete MPC solver, whereas for the dashed lines, the sphere decoding part is subtracted. The data is obtained from experimental testing with measurement series of 10 seconds at steady state, for each setup.

The reference solution surpasses the proposed solution in terms of computational turnaround time. It is of importance to emphasize that both the proposed and the reference solution solves the same problem, obtaining the same optimum solutions. Hence only the solution approach differs. As can be seen, although the sphere decoding part of the solver is time-consuming, the efforts required to set up

the problem and obtaining the analytical solution is dominating for the reference solution. For a horizon length of $N = 1$ and $N = 4$, the reduction in average TAT is -23.6 % and -40.2 %, respectively.

In Fig. 6.5, the MPC solution is evaluated for different update frequencies. The data was obtained from simulations at 4000 r/min and peak torque. As can be seen, in comparison to the FOC-solution, the MPC-solution performs well with respect to switching losses and TDD, defined as

$$I_{TDD} = \frac{1}{I_{s,nom}} \sqrt{\sum_{k \neq 1} (i_n)^2} \tag{6.25}$$

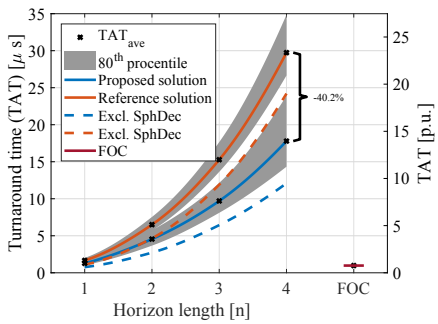


Figure 6.4: Experimental evaluation of turnaround time (TAT) in $\mu s$ for the proposed and the reference solutions. In relation, the ADC required 4.50 $\mu s$ to execute. The dashed lines include the analytical solver only.

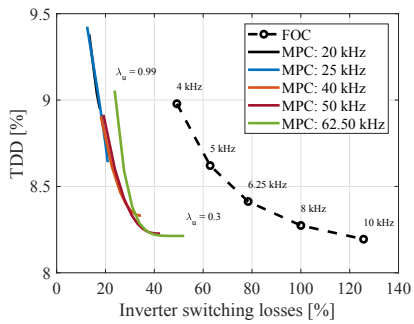


Figure 6.5: Simulations results at 4000 r/min and 50 Nm torque showing the impact of different update frequencies and weighting factors $\lambda_u$. The axis is normalized w.r.t. FOC with $f_s = 8$ kHz. The data is least square fitted based on linearly spaced weighting factors in the interval from 0.3 to 0.99.

Moreover, in Paper VII an evaluation regarding the horizon is also give. It was found that the update frequency has a more significant impact than the horizon length. Further, as the update frequency is increased, the effect of varying the switching effort penalty $\lambda_u$ is also enlarged - As the update frequency is increased, more liberty to tune the controller using $\lambda_u$ is obtained.

Vibration measurements of the machine were conducted to explore the structural response and the acoustic performance. For the two control approaches,

the stator housing vibrations were measured using a unidirectional accelerometer glued to one of four rubber bushing-supported connection points.

In Fig. 6.6, 6.7, 6.8 and 6.9, the frequency spectra of the phase current and the vibrations are presented. The data was obtained using 15 seconds steady state recordings. The characteristics of both the phase current and the vibration frequency spectra differ between the two solutions. The lack of PWM for the MPC-solution yields a completely different spectrum, where the concentrations of harmonics around integer multiples of the switching frequency are absent. Acoustically, it has a less tonal appearance. Instead, the frequency spectrum is of more broadband characteristics, slightly elevated in comparison to the FOC-solution.

The MPC-solution's harmonic spectra share similarities with heavily randomized switching frequency PWM, presented in [71]. With support by the analysis and discussions in [71], it is likely that at low rotational speeds, the acoustic performance of the MPC-solution would suffer from an increased sound power level (SPL). This is due to concluded correlations between annoyance and level-oriented matrices (s.a. loudness, SPL, and sharpness). Moreover, the significant reduction of tonality is believed to have a positive contribution acoustically. A claim which is in line with previous research on the subject [46, 1]. However, in [71], no such significant correlations where detected. Although, as discussed in [71], the complexity of acoustic pleasantness is of such nature that a single psycho-acoustic matrix is not sufficient to correlate the harmonic spectra with the perceived annoyance.

Conclusively, acoustically it is not evident which of the solutions to favor. However, it is plausible that the MPC-solution, in the context of automotive applications with its low-frequency masking noise, from tire-to-road interaction and aerodynamics, is favorable from a system perspective.

### 6.3.4 Conclusions

An FCS-MPC solution with improved computational turnaround time is presented in this work. A detailed analysis of its performance is given, in relation to the well-established field-oriented current control solution. It is shown that the proposed solution is feasible, that the associated optimization problem at hand can be solved in real-time while exploiting the attractiveness of the proposed improvements. The improved problem formulation suggested lowers the computational turnaround

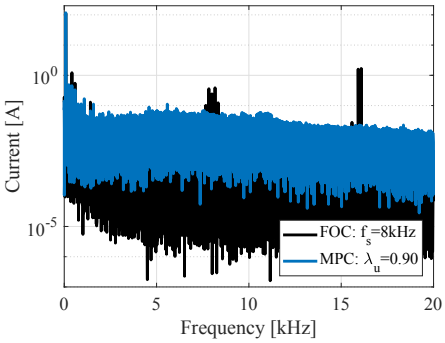


Figure 6.6: Measured frequency spectra of phase current at 1000 r/min, at 50 Nm load torque. The switching frequency using the FOC-solution was 8 kHz and the update frequency for the MPC-solution was 40 kHz.

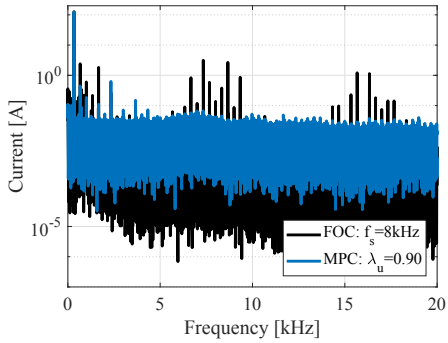


Figure 6.7: Measured frequency spectra of phase current at 4000 r/min, at 50 Nm load torque. The switching frequency using the FOC-solution was 8 kHz and the update frequency for the MPC-solution was 40 kHz.

time of the solver with approximately 40 % for a horizon length of $N = 4$. Apart from the computational requirement aspects, the assessment focuses on inverter efficiency, phase current total demand distortion and acoustic performance.

In summary, it is concluded that the inverter efficiency can be improved without deteriorating the phase current harmonic content. With the given setup, the inverter losses were reduced with 5-15 %. Additionally, a significant decrease in effective switching frequency was obtained. Possibly, the MPC-solution might also be favorable from an acoustic point of view. Although, the acoustic results are not unambiguous, its characteristics with decreased tonality in combination with increased power levels are believed to be favorable for an automotive application. Moreover, it is shown that the update frequency of the solver has a more significant impact on the TDD than the length of the horizon. As the update frequency is increased, more liberty to tune the controller using the penalty weight $\lambda_u$ is obtained.

On the aspects of future work, the author proposes a variety of interesting investigations related to performance enhancements of the current controller as well as the drive system. Firstly, it is believed that a better DC-voltage utilization can be achieved without the risk of reaching an uncontrollable event, both statically and dynamically. Further, increased model and measurement noise resistance could possibly be achieved by evolving the state-space representation to an extended

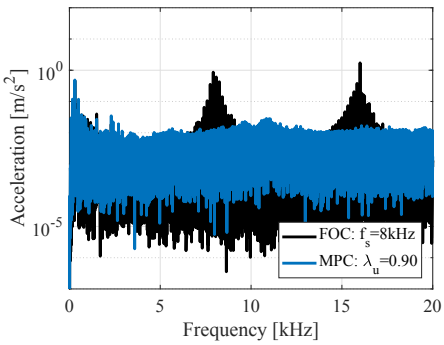


Figure 6.8: Measured frequency spectra of stator vibrations at 1000 r/min, at 50 Nm load torque. The switching frequency using the FOC-solution was 8 kHz and the update frequency for the MPC-solution was 40 kHz.

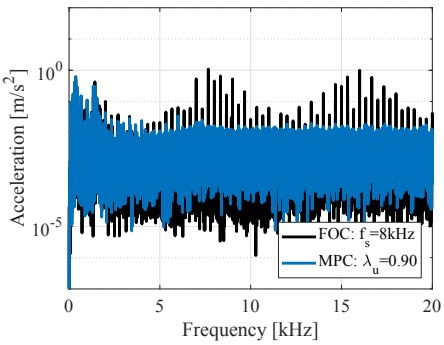


Figure 6.9: Measured frequency spectra of stator vibrations at 4000 r/min, at 50 Nm load torque. The switching frequency using the FOC-solution was 8 kHz and the update frequency for the MPC-solution was 40 kHz.

Kalman filter representation with noise prediction.

## 6.4 Motion sensorless control

For applications such as automotive electric propulsion systems, the need for accurate and reliable rotor position information is two-fold. Firstly, it is needed to enable specific system attributes such as high performance closed loop control systems. Secondly, it is essential to fulfilling functional safety requirements. Such functional safety requirements, originating from the standard ISO-26262 and automotive safety integrity levels, can include but is not limited to, system stability criteria, fault handling abilities, and output torque tracking abilities. Despite the inherent difficulties with sensorless control, there exist intermediate options where a software-based estimator, for instance, can act as a complement to the existing sensor. Either for redundancy purposes or as a complement to a low-speed, low resolution and low-cost sensor. Options that according to the author motivate the need for further research within the area, which also is emphasized in [72].

Methods for sensorless control of AC-drives have been extensively researched the last decades [72, 73, 74, 75, 76]. Typically, researchers divide the methods into two categories - methods based on high-frequency signal injection and methods using the fundamental electrical frequency, often referred to as fundamental

model-based methods [77, 78, 79, 80]. The objective of model-based methods is to use mathematical models to enable access to unknown information based on available information. Naturally, options for different system model representations, application specific limitations, and solution approaches give rise to a vast amount of proposed solutions in literature, neatly illustrated in [74, 73, 76, 80, 81].

In [72], extensive analysis on solutions specifically intended for salient-pole PMSM is given, and prospects for application areas are discussed. Sul *et. al*, highlight applications with heavily saturated, high power density, interior PMSM (IPMSM) as a developing area for sensorless control. Applications, suffering from severe operation conditions and significant parameter variations. In [73], active flux, model-based, observers were thoroughly investigated showing their substantial potential. Moreover, the machine topology universality and the notable simplifications possible as a result of the use of active flux are also shown and discussed.

Moving horizon estimation (MHE), which is the topic of the presented work, has been successfully researched previously for different applications. Frick *et. al.* [82] determined its superiority to more established conventional estimator techniques, such as MRAS- and EKF-based observers, for sensorless induction motor drives. Kuhl *et. al.* [83] reported on the superiority of MHE compared to EKF-based observers in chemical engineering problems. Yet, to the author's knowledge, MHE-based estimators for sensorless control of synchronous machines have not been researched.

In this work, the author proposes a robust active flux-based moving horizon estimator with a Luenberger pre-estimator for automotive applications. The MHE approach relies on a series of measurements, observed over a horizon with a fixed length. At each time instance, the series of measurements, forward simulation of a system model and constraints are used to define a cost function. A function which is defined by a set of weighted least-squares. The optimization objective is to minimize the cost function, subjected to the given constraints. As decision variables, the algorithm estimates the non-measured system states and the process noise for each time instance across the horizon.

At every iteration, the horizon is shifted forward in time, continuously adding new data to the MHE-problem. Data falling out of the horizon at every time-shift of the horizon is summarized in an arrival cost to enhance the performance. The Luenberger pre-estimator was used to further enhance the performance. Primarily at low rotational speeds. The main contribution of this work is to demonstrate the

abilities model-based prediction has in the fields of sensorless control of electrical machines. Experimental results show its feasibility in real-time implementations with high update frequencies and time-varying systems.

It is of importance to emphasize the proposed methods inherent robustness to parameter variations. Explicitly, only the stator resistance and the quadrature-axis inductance are affecting the performance of the estimator, where the effects of stator resistance variations are only minor. This work is in detail described in Paper VI. Hence the extent of the following theoretical sections and the underlying mathematical formulations are only given in an abbreviated version.

### 6.4.1 Problem formulation

The sensorless solution proposed in this paper is based on the concept of active flux, also known as the torque producing flux. A concept which, to the best of the author's knowledge, first was introduced by Boldea *et al.* [74]. Note similarities and differences to previously researched extended EMF solutions [73]. The active flux concept renders salient-pole ac machines into mathematically non-salient ac machines. Observers originating from this concept have been extensively researched, both for different machine topologies and applications. Various derivatives of active flux-based observers can be found in literature, for instance in [74] and [84]. The concept of active flux is based on the appearance of the active flux vector in stationary coordinates, which by its definition falls along the d-axis of the machine, if cross-saturation is either absent or compensated for [85]. Intuitively, it makes a sound basis for rotor position estimation.

The active flux is defined as the flux, which multiplied with the q-current, produces torque. For a PM synchronous machine, using dq-coordinates, it is defined as

$$\lambda_d^a = \lambda_m + (L_d - L_q) i_d \tag{6.26}$$

where $\lambda_d^a$, $\lambda_m$, $L_d$ and $L_q$ are the active flux, permanent magnet flux constant, and d- and q-axis inductances, respectively. $i_d$ is the momentary d-axis current.

From the dq-representation of the salient pole machine, the following non-salient model can be obtained [74]

$$u_s = R_s i_s + (p + j\omega) L_q i_s + (p + j\omega) \lambda_d^a \tag{6.27}$$

where $\lambda_d^a = \lambda_m + (L_d - L_q)i_d$ is the active flux magnitude masking the saliency. $R_s$, $\omega$ and $p$ are the stator resistance, the electrical rotor speed and the differentiate operator, respectively. $i_s$ and $u_s$ are the stator current and voltage. Transformation to the $\alpha\beta$-reference frame gives

$$u_s^s = R_s i_s^s + pL_q i_s^s + p\lambda_d^{a,s} \tag{6.28}$$

which on state space form is equivalent to

$$\begin{bmatrix} u_\alpha \\ u_\beta \end{bmatrix} = \begin{bmatrix} R_s + pL_q & 0 \\ 0 & R_s + pL_q \end{bmatrix} \begin{bmatrix} i_\alpha \\ i_\beta \end{bmatrix} + \begin{bmatrix} e_\alpha \\ e_\beta \end{bmatrix} \tag{6.29}$$

where $e_\alpha$ and $e_\beta$ are the equivalent EMF-components. These can be represented as

$$\begin{bmatrix} e_\alpha \\ e_\beta \end{bmatrix} = p \begin{bmatrix} \lambda_{d\alpha}^a \\ \lambda_{d\beta}^a \end{bmatrix} \simeq w\lambda_d^a \begin{bmatrix} -sin(\theta) \\ cos(\theta) \end{bmatrix} \tag{6.30}$$

where $\lambda_{d\alpha}^a$ and $\lambda_{d\beta}^a$ are the $\alpha\beta$-components of the active flux in the $\alpha\beta$-reference frame, and $\theta$ is the electrical rotor position. In (6.30), the time derivative of the d-current is approximated to zero to simplify the calculations. An approximation, which at steady state operation is acceptable, but puts demands on the algorithm during transients.

A reasonable approach for state space representation of (6.29) and (6.30) would be to choose a state vector as $[i_\alpha \; i_\beta \; e_\alpha \; e_\beta]^T$, as in [84]. However, the selection of $e_\alpha$ and $e_\beta$ as states brings unnecessary modelling weakness to the MHE-problem. This weakness originates from the inherent magnitude variations of $|e_{\alpha\beta}|$ due to the linear dependence of $w$ as well as the influence of the hidden saliency. The authors instead propose to use a mathematically equivalent model with the state vector defined as

$$x = \begin{bmatrix} i_\alpha \\ i_\beta \\ \frac{\lambda_d^a cos(\theta)}{L_q} \\ \frac{\lambda_d^a sin(\theta)}{L_q} \end{bmatrix} = \begin{bmatrix} i_\alpha \\ i_\beta \\ \frac{\lambda_{d,\alpha}^a}{L_q} \\ \frac{\lambda_{d,\beta}^a}{L_q} \end{bmatrix} \tag{6.31}$$

where the active flux in $\alpha\beta$-coordinates, divided by the q-inductance, were used as states directly. This leads to the following final continuous time state space matrices,

$$
\begin{aligned}
A &= \begin{bmatrix} -\frac{R_s}{L_q} & 0 & 0 & \omega \\ 0 & -\frac{R_s}{L_q} & -\omega & 0 \\ 0 & 0 & 0 & -\omega \\ 0 & 0 & \omega & 0 \end{bmatrix} \\
B &= \begin{bmatrix} \frac{1}{L_q} & 0 \\ 0 & \frac{1}{L_q} \\ 0 & 0 \\ 0 & 0 \end{bmatrix}, \quad C = \begin{bmatrix} 1 & 0 & 0 & 0 \\ 0 & 1 & 0 & 0 \end{bmatrix}
\end{aligned} \tag{6.32}
$$

As can be seen in (6.32), the only two parameters required are the stator resistance and the q-axis inductance. By incorporating the active flux magnitude in the states, both $L_d$ and $\lambda_m$ are hidden. Hence, variations in these parameters do not influence the performance of the estimator. Suppressing uncertainties tied to these parameters brings additional robustness to the model which also increases the confidence in the model. Moreover, by including the division by $L_q$ in the two latter states, their magnitude is more comparable to the stator current, which is favorable when solving the MHE-problem.

From the estimates, $\hat{x}_3$ and $\hat{x}_4$, the rotor position and the rotational speed was obtained using a normalized quadrature phase locked loop (Q-PLL). The error signal to the Q-PLL was defined as

$$
e = 2\hat{x}_3\hat{x}_4 cos(2\hat{\theta}) - sin(2\hat{\theta})\left(\hat{x}_3^2 - \hat{x}_4^2\right) \tag{6.33}
$$

In the Q-PLL, the rotational speed was obtained by a PI-controller driven by the error (6.33) whereas the rotor angle was obtained by integrating the rotational speed, much in similarity with the proposed Q-PLL presented in [86].

The closed loop transfer function of the Q-PLL is

$$
\frac{\hat{\theta}}{\theta} = \frac{sK_p + K_i}{s^2 + sK_p + K_i} \tag{6.34}
$$

The poles were defined as complex conjugates and located at $s = (-1 \pm j)\omega_b/\sqrt{2}$, resulting in $K_p = \sqrt{2}\omega_b$ and $K_i = \omega_b^2$, where $\omega_b$ is regarded as the bandwidth of the Q-PLL.

In the proposed algorithm, the state space model, based on the discretization of the model in (6.32), was extended with a Luenberger output feedback observer.

Luenberger observers have shown superiority, both considering robustness and performance, in several comparative studies [87, 88]. The observer adds a correction to the model by its feedback of the measurable states to enhance the dynamic performance, primarily at low rotational speeds. The resulting system dynamics was modeled as

$$\begin{aligned} \dot{x} &= Ax + Bu + L\left(y - \hat{y}\right) \\ \hat{y} &= Cx \end{aligned} \tag{6.35}$$

where $L$ is the Luenberger gain matrix, $y$ and $\hat{y}$ are the measured and estimated phase currents in the $\alpha\beta$-reference frame.

The pole assignment selection was based on a trade-off between response time and robustness. The observer gain matrix was designed based on pole assignment of the error dynamics $(A - LC)$, where the observer dynamics were set to be approximately ten times faster than the system dynamics. As discussed by Zhang *et. al.* [88], the pole assignment is a delicate matter in variable speed drive applications. In the proposed algorithm, the gain matrix is derived at a specific rotational speed of the machine and scaled linearly with the speed as it varies. It is of high importance to study, for instance, the root locus for a wide speed range to guarantee observer stability for the entire rotational speed range.

The Luenberger observer is further discussed in Paper VI, where issues related to the time-variant plant model is analyzed.

### 6.4.2 Linear moving horizon estimation

Parameter estimation using linear systems with random measurement and process noises are commonly seen. From theory, it follows that the Kalman filter (KF) estimator is the optimal linear estimator if the probability distribution of the noise is known and the system representation is exact. Assumptions which might be motivated by mathematical tractability, yet for many practical problems questionable and possibly erroneous.

The motivation for using MHE, with the framework of KF, is based on the hypothesis to remedy problems associated with the aforementioned imperfections, by exploiting more data recursively.

The optimization variables are the state vector in the state space model, e.g., the phase current and the active flux in the $\alpha\beta$-reference frame, and the

process noise. The optimization objective is to minimize the least square error between the measured and estimated phase, i.e., the tracking error of the phase current currents, as well as the process noise. The former is somewhat intuitive, whereas the latter is needed to prevent the noise to dominate completely. If the noise was not included, it will to a larger extent be used to cancel the error defined by the tracking error.

The system was represented with the following discrete-time linear, time-variant, state space model

$$\begin{aligned} \hat{x}_{k+1} &= A_d\hat{x}_k + B_d u_k + w_k + L\left(y_k - \hat{y}_k\right) \\ \hat{y}_k &= C\hat{x}_k + v_k \\ \hat{x}_k &= \in \mathbb{X},\ w_k \in \mathbb{W},\ v_k \in \mathbb{V} \end{aligned} \tag{6.36}$$

where $\mathbb{X}$, $\mathbb{W}$ and $\mathbb{V}$ are constrained. The subscript $k$ index the discrete time samples in chronological order. The last term, $L\left(y_k - \hat{y}_k\right)$, represents the Luenberger output feedback observer and $w_k$ and $v_k$ are the process and observation noises at time $k$. Both $w_k$ and $v_k$ are assumed to be zero-mean noises with the covariance matrices $Q_k$ and $R_k$, respectively. $w_k$ models disturbances and model inaccuracies whereas $v_k$ models sensor noise in the measurement. By forward simulation, the output data sequence $\{\hat{y}\}_0^k$ can be obtained based on measurements $\{y\}_0^k$, the initial state vector $x_0$ and its covariance matrix $\Pi_0$ and the disturbance sequence $\{w\}_0^k$. The initial state vector of the system $x_0$ was assumed to be normally distributed with mean $\bar{x}$ and covariance $\Pi_0$.

The optimization problem is formulated as the following set of constrained least-squares problem:

$$\begin{aligned} \phi\left(x_0, w_k\right) = ||x_0 - \bar{x}_0||^2_{P_0} + \\ \sum_{k=0}^{T} ||y_k - Cx_k||^2_V + \sum_{k=0}^{T-1} ||w_k||^2_W \end{aligned} \tag{6.37}$$

subject to (6.36). The norms were defined as $||z - \bar{z}||^2_A := (z - \bar{z})^T A^T A(z - \bar{z})$ and $V^T V = R^{-1}$, $W^T W = Q^{-1}$ and $P_0^T P_0 = \Pi_0^{-1}$, assuming that the covariance matrices are non-singular and hence invertible.

With this formulation, the problem size grows with time, since more data is included as time proceeds. The complexity of such problems grows at least linearly with time [89]. The problem size needs to be bound, to make the problem feasible for real-time implementation. This was done by employing a moving

horizon approach. The approach is based on a fixed horizon where the problem data is bounded by a number of consecutive sampling instances, equivalent to the length of the horizon. Information not explicitly treated within the window of the optimization horizon is summarized in an arrival cost term, updated sequentially as the fixed horizon is moved forward in time. With the approach of a fixed horizon of length $N$ and an arrival cost, the MHE-problem can be redefined as

$$\begin{aligned}\phi\left(x_k, w_k\right) := \phi_{T-N}\left(x_0\right) + \\ \sum_{k=T-N}^{T} ||y_k - Cx_k||_V^2 + \sum_{k=T-N}^{T-1} ||w_k||_W^2\end{aligned} \tag{6.38}$$

where the arrival cost $\phi_{T-N}\left(x_0, w_k\right)$ at time $k = T - N$ was defined as

$$\phi_{T-N}\left(x_k\right) = ||x_{T-N} - \bar{x}_{T-N}||_{P_{T-N}}^2 + \phi_{T-N}^* \tag{6.39}$$

where $\phi_{T-N}^*$ is the optimal cost to go at time $k = T - N$ [89], leading to the final problem definition

$$\begin{aligned}\phi\left(x_k, w_k\right) := ||x_{T-N} - \bar{x}_{T-N}||_{P_{T-N}}^2 + \\ \underbrace{\sum_{k=T-N}^{T} ||y_k - Cx_k||_V^2 + \sum_{k=T-N}^{T-1} ||w_k||_W^2}_{\Lambda_k}\end{aligned} \tag{6.40}$$

The solution to the optimization and hence to the minimization of (6.40), yields the optimal disturbance sequence $\{w\}_{k=T-N}^{k=T-1}$ and the optimal states sequence $\{x\}_{k=T-N}^{k=T}$. The length of the horizon is directly affecting the results and was treated as a tuning parameter in the MHE-formulation. As the horizon grows the optimization explicitly handles more data and the performance is enhanced with the expense of computational burden. However, as the complexity grows at least linearly with the horizon length, but the returns diminish as the horizon is sufficiently large, the computational cost for increased performance increases rapidly as the horizon is extended beyond a certain level. Rao *et. al.* [90], recommend a horizon length twice the order of the system as a reasonable trade-off between accuracy and computational burden.

The key of preserving stability and enabling high performance is the approximation of the arrival cost term, and explicitly how discarded data, e.g., data falling out of the horizon, is preserved and used in the optimization [90, 83, 91]. For

unconstrained linear optimization, the arrival cost can be explicitly expressed using the Kalman filter covariance matrix update formula, in opposition to non-linear systems where analytical approximations are required [91].

As discussed by Rao *et. al* [90], for linear systems when inequality constraints are inactive, the arrival cost approximation with the Kalman filter covariance matrix update is exact. Hence a reasonable solution is to approximate the arrival cost for the unconstrained problem. The covariance matrix update is obtained by solving the Riccati equation

$$\begin{aligned}\Pi_T = Q + A\Pi_{T-1}A^T - \\ A\Pi_{T-1}C^T\left(R + C\Pi_{T-1}C^T\right)^{-1} C\Pi_{T-1}A^T\end{aligned} \tag{6.41}$$

The solution to the MHE-problem is obtained by solving the Lagrange function associated with (6.40), which turns out as a root finding problem. The solution, defined by the gradient of the dual feasibility equations ($\nabla\mathcal{L}$) and the gradient of the primal feasibility equations ($G = 0$) [92], is defined as

$$\begin{pmatrix}\nabla\mathcal{L} \\ G\end{pmatrix} = 0 \tag{6.42}$$

The gradient of the Lagrangian results in a set of matrix equations where the gradients themselves are row vectors, each with a size equal to the number of states, expressed as

$$\begin{aligned}\nabla_{x_0}\mathcal{L} = r_{x_0} = \nabla_{x_0}\Gamma + \nabla_{x_0}\Lambda_0 - \nabla_{x_0}f_0^T\lambda_1 = 0 \\ \nabla_{x_k}\mathcal{L} = r_{x_k} = \nabla_{x_k}\Lambda_k - \nabla_{x_k}f_k^T\lambda_{k+1} + \lambda_k = 0 \\ \nabla_{x_N}\mathcal{L} = r_{x_N} = \nabla_{x_N}\Lambda_N + \lambda_k = 0 \\ \nabla_{w_k}\mathcal{L} = r_{w_k} = \nabla_{w_k}\Lambda_k - \nabla_{w_k}f_k^T\lambda_{k+1} = 0 \\ \nabla_{\lambda_{k+1}}\mathcal{L} = r_{\lambda_{k+1}} = x_{k+1} - f_k = 0\end{aligned} \tag{6.43}$$

where $\Gamma$ is the arrival cost term, $\Lambda_k$ is the stage cost at time $k$ and $f_k = A_d\hat{x}_k + B_d u_k + w_k + L(y - \hat{y}_k)$. For $N = 2$, the solution to the MHE-problem is obtained solving the following KKT-system

$$\left[\begin{array}{ccc|ccc|c} E_0 & & A_0^T & & & & \\ & R_0 & G_0^T & & & & \\ A_0 & G_0 & & -I & & & \\ \hline & & -I & Q_1 & & A_1^T & \\ & & & & R_1 & G_1^T & \\ & & & A_1 & G_1 & & -I \\ \hline & & & & & -I & Q_2 \end{array}\right] \left[\begin{array}{c} x_0 \\ w_0 \\ \lambda_0 \\ \hline x_1 \\ w_1 \\ \lambda_1 \\ \hline x_2 \end{array}\right] = \left[\begin{array}{c} r_{x_0} \\ r_{w_0} \\ r_{\lambda_0} \\ \hline r_{x_1} \\ r_{w_1} \\ r_{\lambda_1} \\ \hline r_{x_2} \end{array}\right] \tag{6.44}$$

where $A_k^T = -\nabla_{x_k} f_k^T \lambda_{k+1}$, $G_k^T = -\nabla_{w_k} f_k^T \lambda_{k+1}$, $E_0 = 2C_d^T V^T V C_d + \Pi_0^{-1} + \Pi_0^{-T}$, $R_k = 2W^T W$ and $Q_k = 2C_d^T V^T V C_d$.

Direct multiple-shooting was used to solve the problem online. The structure of the symmetric KKT-matrix was exploited, and the solution was derived using LU-factorization with forward-backward substitution. The problem as a whole was for each time instance defined and solved online, without the use of any offline calculations - An approach which might not be optimal considering turnaround time. If the states had been selected differently, the time variations could have been moved to the states resulting in a time-invariant system. In such case, much of the computations leading up to the problem definition could be done offline.

The system dynamics was discretized on a uniform time grid, equally spaced with a time separation equal to the update time of the algorithm. On the time intervals, the inputs were treated as piece-wise constants. By analogy with non-linear MHE, a single Newton step was used to solve the problem at each time instance.

### 6.4.3 Assessment

In the following section, the proposed MHE-sensorless algorithm is evaluated using results from both simulations and experimental testing. The evaluation focuses primarily on dynamic performance, parameter sensitivity and turnaround time (e.g., the execution time required for the different solutions).

In Fig. 6.10, the rotational speed and electromagnetic torque profiles used during the experiments are presented. In the first half, both rotational speed and torque are positive, whereas in the second half the speed is reversed while the torque remains positive. Combined, both motor and generator mode, as well as positive and negative rotational directions, were tested. The speed reversal

appears during no-load - A case when the system is minimally excited. In Fig. 6.12 and 6.13 the steady-state mean RMS error, and the turnaround time are presented for different length of the estimation horizon. The mean RMS error and its standard deviation were calculated using 40 consecutive measurement series, as the one presented in Fig. 6.10. The mean RMS-error was defined as the mean of the RMS-error in each of the 40 series. As shown in Fig. 6.12, the MHE-solution outperforms the active flux-based observer. Although, it is to a considerable computational cost, as is shown in Fig. 6.13.

Furthermore, the performance of the MHE is enhanced as the horizon length is extended. However, the benefits of longer horizons decay as it grows. This is clearly in line with previous research where, for instance, Rao *et. al.* [90] recommend a horizon length twice the order of the system as a reasonable trade-off to reconcile both objectives of performance and turnaround time. The performance enhancements obtained from a longer horizon is not only in terms of mean RMS-error, but it is also shown that the standard deviation decay with longer horizons. A result, showing on increased consistency, which is interpreted as decreased noise sensitivity.

Moreover, it might be appealing to accredit the MHE performance advantage to specific parts of the measurement series. Such as either the zero-crossing event or the other parts. However, excluding the zero-crossing event data, the absolute values decrease, but the trend remains, as can be seen in Fig. 6.12. Clearly, the MHE with a horizon of 2 or longer yields lower RMS-error than the benchmark solution.

Since none of the solutions is rotor position estimator, but somewhat active flux estimators, the subsequent Q-PLL is a key factor in both solutions. In Fig. 6.11, the rotor position error in electrical degrees are presented for different Q-PLL bandwidths. The data is showing the RMS-error during no-load obtained from 20-second steady state measurements at every 200 r/min, stretching from 400 to 4000 r/min. At speeds less than 3000 r/min, the difference is significant, hence the logarithmic y-scale. Evidently, the no-load performance of the MHE is superior to the reference Active flux-observer. Although it is not shown, it has been noted (and indicated by the trends in Fig. 6.11), that stability is kept further towards zero speed for the MHE-observer, then for the Active flux-observer. Also, the MHE-solution performs reasonably well with all three Q-PLL bandwidths.

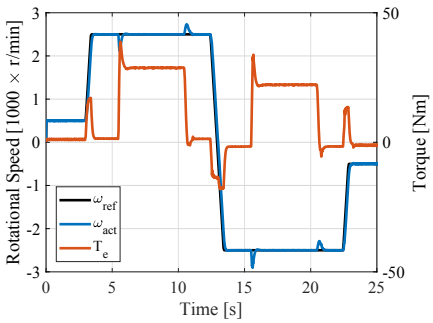


Figure 6.10: Speed and torque profiles used during the experimental testing. The measurement procedure was automated to improve consistency when multiple consecutive runs were executed.

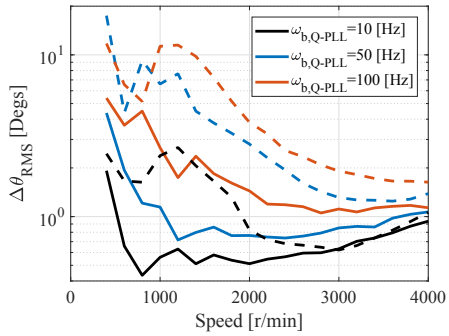


Figure 6.11: Measured RMS-error of rotor position in electrical degrees for different bandwidths of the Q-PLL. The solid and dashed lines show results using MHE and Active Flux-observer, respectively. Each data point is based on steady state measurements with a duration of 20 seconds.

### 6.4.4 Conclusions

A moving horizon estimation algorithm for motion sensorless control of an IPMSM is presented in this work. A detailed analysis of its performance is given, in relation to a well-established active flux-based observer. It is shown that the proposed solution is feasible, that the associated dynamic optimization problem can be solved in real-time while exploiting the attractiveness of the MHE-approach to obtain highly accurate estimates.

The influence of the length of the estimation horizon is discussed. It is shown that the length of the horizon directly affects the performance, where longer horizons are preferable. Although, it comes with an increased computational cost. Moreover, the absence of d-axis flux in the proposed solution is considered a significant strength. Conclusively, it turns the proposed solution into a universal solution for any synchronous motor, regardless of whether a PM-, PM-assisted or reluctance motor is used, non-dependent on the presence of magnetic saliency.

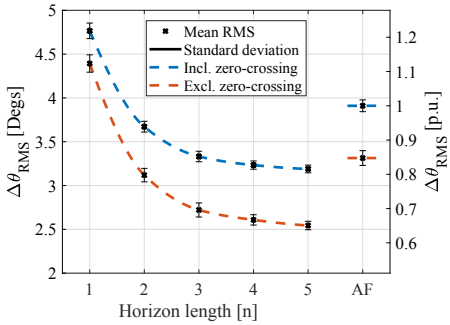


Figure 6.12: Measured mean RMS-error with one standard deviation for MHE with horizon lengths $N = 1 - 5$ and the Active flux-observer, each based on 40 measurement series. The results are given both with and without the influence of the zero-crossing.

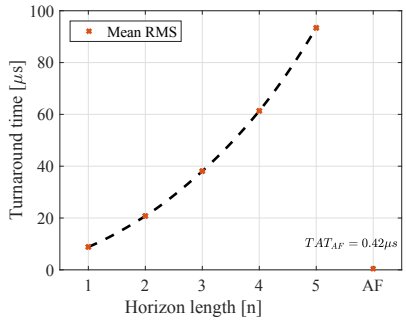


Figure 6.13: Measured turnaround time for different horizon lengths as well as for the Active flux-observer. The results are calculated using 40 measurement series for each setup.

# References

[1] I. P. Tsoumas and H. Tischmacher. Influence of the inverter's modulation technique on the audible noise of electric motors. *IEEE Transactions on Industry Applications*, 50(1):269–278, Jan 2014.

[2] E. A. Grunditz and T. Thiringer. Performance analysis of current bevs based on a comprehensive review of specifications. *IEEE Transactions on Transportation Electrification*, 2(3):270–289, Sept 2016.

[3] W. Zine, L. Idkhajine, L. Kobylanski, E. Monmasson, P. A. Chauvenet, A. Bruyere, and B. Condamin. Compensation of cross-saturation effects on ipmsm sensorless control - application to electric vehicle. In *IECON 2016 - 42nd Annual Conference of the IEEE Industrial Electronics Society*, pages 6675–6680, Oct 2016.

[4] B. Sarlioglu, C. T. Morris, D. Han, and S. Li. Benchmarking of electric and hybrid vehicle electric machines, power electronics, and batteries. In *2015 Intl Aegean Conference on Electrical Machines Power Electronics (ACEMP), 2015 Intl Conference on Optimization of Electrical Electronic Equipment (OP-*

*TIM) 2015 Intl Symposium on Advanced Electromechanical Motion Systems (ELECTROMOTION)*, pages 519–526, Sept 2015.

[5] International Energy Agency. Global EV Outlook 2017 [Online]. Accessed 2017-05-14. Available at `https://www.iea.org/publications/freepublications/publication/GlobalEVOutlook2017.pdf`.

[6] International Energy Agency. Nordic EV Outlook 2018 [Online]. Accessed 2017-05-14. Available at `https://www.iea.org/publications/freepublications/publication/NordicEVOutlook2018.pdf`.

[7] Chong Wang Jacek F. Gieras and Joseph Cho Lai. *Noise of Polyphase Electric Motors*. CRC Press, 2005.

[8] Yongxiang Xu, Qingbing Yuan, Jibin Zou, and Yong Li. Analysis of triangular periodic carrier frequency modulation on reducing electromagnetic noise of permanent magnet synchronous motor. *IEEE Transactions on Magnetics*, 48(11):4424–4427, Nov 2012.

[9] Jui-Yuan Chai, Yeh-Hsiang Ho, Yu-Choung Chang, and Chang-Ming Liaw. On acoustic-noise-reduction control using random switching technique for switch-mode rectifiers in pmsm drive. *IEEE Transactions on Industrial Electronics*, 55(3):1295–1309, March 2008.

[10] D. Torregrossa, D. Paire, F. Peyraut, B. Fahimi, and A. Miraoui. Active mitigation of electromagnetic vibration radiated by pmsm in fractional-horsepower drives by optimal choice of the carrier frequency. *IEEE Transactions on Industrial Electronics*, 59(3):1346–1354, March 2012.

[11] Conggan Ma and Shuguang Zuo. Black-box method of identification and diagnosis of abnormal noise sources of permanent magnet synchronous machines for electric vehicles. *IEEE Transactions on Industrial Electronics*, 61(10):5538–5549, Oct 2014.

[12] M. Sarrazin, J. Anthonis, H. Van der Auweraer, C. Martis, and J. Gyselinck. Signature analysis of switched reluctance and permanent magnet electric vehicle drives. In *International Conference on Electrical Machines (ICEM)*, pages 1831–1837, Sept 2014.

[13] Yen-Shin Lai, Ye-Then Chang, and Bo-Yuan Chen. Novel random-switching pwm technique with constant sampling frequency and constant inductor average current for digitally controlled converter. *IEEE Transactions on Industrial Electronics*, 60(8):3126–3135, Aug 2013.

[14] Yen-Shin Lai and Bo-Yuan Chen. New random pwm technique for a full-bridge dc/dc converter with harmonics intensity reduction and considering efficiency. *IEEE Transactions on Power Electronics*, 28(11):5013–5023, Nov 2013.

[15] J. Prieto, M. Jones, F. Barrero, E. Levi, and S. Toral. Comparative analysis of discontinuous and continuous pwm techniques in vsi-fed five-phase induction motor. *IEEE Transactions on Industrial Electronics*, 58(12):5324–5335, Dec 2011.

[16] R.L. Kirlin, M.M. Bech, and A.M. Trzynadlowski. Analysis of power and power spectral density in pwm inverters with randomized switching frequency. *IEEE Transactions on Industrial Electronics*, 49(2):486–499, Apr 2002.

[17] N. Boudjerda, A. Boudouda, M. Melit, B. Nekhoul, K. El Khamlichi Drissi, and K. Kerroum. Optimized dual randomized pwm technique for reducing conducted emi in dc-ac converters. In *EMC Europe*, pages 701–706, Sept 2011.

[18] T. Rylander, A. Bondeson, and P. Ingelstrom. *Computational Electromagnetics*. Springer, 2013.

[19] J.R Hendershot and T.J.E Miller. *Design of Brushless Permanent-Magnet Machines*. Magna Physics Publishing And Oxford University Press, 1994.

[20] Maxwell online help. release 14.5 - sas ip, inc.

[21] N. Mohan, T. Undeland, and W. Robins. *Power electronics : converters, applications and design*. John Wiley and sons inc., 2003.

[22] K. C. Maliti. *Modelling and Analysis of magnetic noise in squirrel-cage induction motors*. KTH Hogskoletryckeriet, 2000.

[23] B. Sutthiphornsombat, A. Khoobroo, and B. Fahimi. Mitigation of acoustic noise and vibration in permanent magnet synchronous machines drive using field reconstruction method. *IEEE Vehicle Power and Propulsion Conference (VPPC)*, pages 1–5, Sept 2010.

[24] S. Zuo, F. Lin, and X. Wu. Noise analysis, calculation and reduction of external rotor permanent magnet synchronous motor. *IEEE Transactions on Industrial Electronics*, PP(99):1–1, 2015.

[25] L. Chang, A.R. Eastham, and G.E. Dawson. Permanent magnet synchronous motor: finite element torque calculations. In *Conference Record of the 1989*

*IEEE Industry Applications Society Annual Meeting*, pages 69–73 vol.1, Oct 1989.

[26] W. Zhu, B. Fahimi, and S. Pekarek. Optimal excitation of permanent magnet synchronous machines via direct computation of electromagnetic force components. In *IEEE International Conference on Electric Machines and Drives*, pages 918–925, May 2005.

[27] Haodong Yang and Yangsheng Chen. Influence of radial force harmonics with low mode number on electromagnetic vibration of pmsm. *IEEE Transactions on Energy Conversion*, 29(1):38–45, March 2014.

[28] D. Zarko, D. Ban, and T.A. Lipo. Analytical calculation of magnetic field distribution in the slotted air gap of a surface permanent-magnet motor using complex relative air-gap permeance. *IEEE Transactions on Magnetics*, 42(7):1828–1837, July 2006.

[29] Haodong Yang and Yangsheng Chen. Influence of radial force harmonics with low mode number on electromagnetic vibration of pmsm. *IEEE Transactions on Energy Conversion*, 29(1):38–45, March 2014.

[30] Umamaheshwar Krishnamurthy. *Mitigation of Vibration in a Permanent Magnet Synchronous Machine Using Field Reconstruction*. The University of Texas at Arlington, 2008.

[31] O. Josefsson, T. Thiringer, S. Lundmark, and H. Zelaya. Evaluation and comparison of a two-level and a multilevel inverter for an ev using a modulized battery topology. In *38th Annual Conference on IEEE Industrial Electronics Society (IECON)*, pages 2949–2956, Oct 2012.

[32] Oskar Josefsson. *Investigation of a Multilevel Inverter for Electric Vehicle Applications*. PhD thesis, Technical university of Chalmers, 2015.

[33] Stephan Brueske, Robin Kuehne, and Friedrich W. Fuchs. Comparison of topologies for the main inverter of an electric vehicle. In *Proceedings of International Exhibition and Conference for Power Electronics, Intelligent Motion, Renewable Energy and Energy Management PCIM*, pages 1–8, May 2014.

[34] L. Harnefors. *Control of Variable-Speed Drives*. Applied signal processing and control, Department of electronics, Malardalen University, Vasteras, Sweden, 2002.

[35] Yunxiang Wu, M.A. Shafi, A.M. Knight, and R.A. McMahon. Comparison of the effects of continuous and discontinuous pwm schemes on power losses of voltage-sourced inverters for induction motor drives. *IEEE Transactions on Power Electronics*, 26(1):182–191, Jan 2011.

[36] T.G. Habetler and D.M. Divan. Acoustic noise reduction in sinusoidal pwm drives using a randomly modulated carrier. In *20th Annual IEEE Power Electronics Specialists Conference (PESC)*, pages 665–671 vol.2, Jun 1989.

[37] K.Y. Cho, S.B. Yang, H.W. Kim, and J.C. Kim. Improving sound quality of reciprocating compressor using random pwm. In *Eighth International Conference on Power Electronics and Variable Speed Drives. (IEE Conf. Publ. No. 475)*, pages 431–436, 2000.

[38] I.P. Tsoumas and H. Tischmacher. Influence of the inverter's modulation technique on the audible noise of electric motors. *IEEE Transactions on Industry Applications*, 50(1):269–278, Jan 2014.

[39] S.L. Capitaneanu, B. de. Fornel, M. Fadel, and F. Jadot. On the acoustic noise radiated by pwm ac motor drives. *AUTOMATIKA*, 44(3-4):137–145, 2003.

[40] V. Lanfranchi, G. Friedrich, J. Le Besnerais, and M. Hecquet. Spread spectrum strategies study for induction motor vibratory and acoustic bahevior. In *32nd Annual Conference on IEEE Industrial Electronics (IECON)*, pages 1423–1428, Nov 2006.

[41] D. Baimel, R. Rabinovici, and S. Tapuchi. Phase shifted pwm with third harmonic injection for over-modulation range operation. In *2014 International Symposium on Power Electronics, Electrical Drives, Automation and Motion*, pages 753–757, June 2014.

[42] A. Beig, S. Kanukollu, K. AlHosani, and A. Dekka. Space vector based synchronized three-level discontinuous pwm for medium voltage high power vsi. *IEEE Transactions on Industrial Electronics*, PP(99):1–1, 2013.

[43] Miliani El Hadj. Dsp based random discontinuous space vector pwm for variable speed electrical drives. In *15th European Conference on Power Electronics and Applications (EPE)*, pages 1–10, 2013.

[44] A. M. Hava, R. J. Kerkman, and T. A. Lipo. Carrier-based pwm-vsi over-modulation strategies: Analysis, comparison, and design. *IEEE Transactions on Power Electronics*, 13(4):674–689, Jul 1998.

[45] D. Eggers, S. Steentjes, and K. Hameyer. Advanced iron-loss estimation for nonlinear material behavior. *IEEE Transactions on Magnetics*, 48(11):3021–3024, Nov 2012.

[46] J. Y. Chai, Y. H. Ho, Y. C. Chang, and C. M. Liaw. On acoustic-noise-reduction control using random switching technique for switch-mode rectifiers in pmsm drive. *IEEE Transactions on Industrial Electronics*, 55(3):1295–1309, March 2008.

[47] Method for the subjective assessment of intermediate quality level of coding systems, 2003.

[48] M. Lofdahl, A. Nykanen, and R. Johnsson. Prominence of different directions of hub forces and moments in structure-borne tire noise. *SAE Int. J. Passeng. Cars - Mech. Syst.*, 8(1):346–353, 2015.

[49] T.W. Bassett, S. Tate, and M. Maunder. Study of high frequency noise from electric machines in hybrid and electric vehicles. In *Proc. of InterNoise*, 2014.

[50] D. Lennstrom, T. Lindbom, and Nykanen. Prominence of tones in electric vehicle interior noise. In *Proc. of InterNoise*, 2013.

[51] S. Fingerhuth. *Tonalness and consonance of technical sounds.* PhD thesis, Rhine-Westphalia Institute of Technology Aachen, 2009.

[52] Meifen Cao and N. Hoshi. Electrical loss minimization strategy for interior permanent magnet synchronous motor drives. In *IEEE Vehicle Power and Propulsion Conference (VPPC)*, pages 1–6, Sept 2010.

[53] C. Cavallaro, A.O. Di Tommaso, R. Miceli, A. Raciti, G.R. Galluzzo, and M. Trapanese. Efficiency enhancement of permanent-magnet synchronous motor drives by online loss minimization approaches. *IEEE Transactions on Industrial Electronics*, 52(4):1153–1160, Aug 2005.

[54] P. Cortes, M. P. Kazmierkowski, R. M. Kennel, D. E. Quevedo, and J. Rodriguez. Predictive control in power electronics and drives. *IEEE Transactions on Industrial Electronics*, 55(12):4312–4324, Dec 2008.

[55] J. Rodriguez, M. P. Kazmierkowski, J. R. Espinoza, P. Zanchetta, H. Abu-Rub, H. A. Young, and C. A. Rojas. State of the art of finite control set model predictive control in power electronics. *IEEE Transactions on Industrial Informatics*, 9(2):1003–1016, May 2013.

[56] B. Stellato, T. Geyer, and P. J. Goulart. High-speed finite control set model predictive control for power electronics. *IEEE Transactions on Power Electronics*, 32(5):4007–4020, May 2017.

[57] T. Geyer and D. E. Quevedo. Multistep direct model predictive control for power electronics; part 1: Algorithm. In *2013 IEEE Energy Conversion Congress and Exposition*, pages 1154–1161, Sept 2013.

[58] T. Geyer and D. E. Quevedo. Multistep direct model predictive control for power electronics; part 2: Analysis. In *2013 IEEE Energy Conversion Congress and Exposition*, pages 1162–1169, Sept 2013.

[59] P. Karamanakos, T. Geyer, T. Mouton, and R. Kennel. Computationally efficient sphere decoding for long-horizon direct model predictive control. In *2016 IEEE Energy Conversion Congress and Exposition (ECCE)*, pages 1–8, Sept 2016.

[60] T. Geyer and D. E. Quevedo. Multistep finite control set model predictive control for power electronics. *IEEE Transactions on Power Electronics*, 29(12):6836–6846, Dec 2014.

[61] F. Wang, X. Mei, J. Rodriguez, and R. Kennel. Model predictive control for electrical drive systems-an overview. *CES Transactions on Electrical Machines and Systems*, 1(3):219–230, September 2017.

[62] M. Dorfling, H. Mouton, P. Karamanakos, and T. Geyer. Experimental evaluation of sphere decoding for long-horizon direct model predictive control. In *2017 19th European Conference on Power Electronics and Applications (EPE'17 ECCE Europe)*, pages P.1–P.10, Sept 2017.

[63] C. S. Lim, E. Levi, M. Jones, N. A. Rahim, and W. P. Hew. Fcs-mpc-based current control of a five-phase induction motor and its comparison with pi-pwm control. *IEEE Transactions on Industrial Electronics*, 61(1):149–163, Jan 2014.

[64] C. S. Lim, E. Levi, M. Jones, N. A. Rahim, and W. P. Hew. A comparative study of synchronous current control schemes based on fcs-mpc and pi-pwm for a two-motor three-phase drive. *IEEE Transactions on Industrial Electronics*, 61(8):3867–3878, Aug 2014.

[65] A. A. Ahmed, B. K. Koh, and Y. I. Lee. A comparison of finite control set and continuous control set model predictive control schemes for speed control of

induction motors. *IEEE Transactions on Industrial Informatics*, PP(99):1–1, 2017.

[66] M. Siami, D. Arab Khaburi, and J. Rodriguez. Simplified finite control set-model predictive control for matrix converter-fed pmsm drives. *IEEE Transactions on Power Electronics*, 33(3):2438–2446, March 2018.

[67] M. Siami, D. A. Khaburi, M. Rivera, and J. RodrÃŋguez. An experimental evaluation of predictive current control and predictive torque control for a pmsm fed by a matrix converter. *IEEE Transactions on Industrial Electronics*, 64(11):8459–8471, Nov 2017.

[68] S. S. Yeoh, T. Yang, L. Tarisciotti, C. I. Hill, S. Bozhko, and P. Zanchetta. Permanent-magnet machine-based starter generator system with modulated model predictive control. *IEEE Transactions on Transportation Electrification*, 3(4):878–890, Dec 2017.

[69] T. Geyer, N. Oikonomou, G. Papafotiou, and F. D. Kieferndorf. Model predictive pulse pattern control. *IEEE Transactions on Industry Applications*, 48(2):663–676, March 2012.

[70] R. Baidya, R. P. Aguilera, P. AcuÃśa, S. Vazquez, and H. d. T. Mouton. Multistep model predictive control for cascaded h-bridge inverters: Formulation and analysis. *IEEE Transactions on Power Electronics*, 33(1):876–886, Jan 2018.

[71] A. Andersson, D. LennstrÃűm, and A. NykÃďnen. Influence of inverter modulation strategy on electric drive efficiency and perceived sound quality. *IEEE Transactions on Transportation Electrification*, 2(1):24–35, March 2016.

[72] S. K. Sul, Y. C. Kwon, and Y. Lee. Sensorless control of ipmsm for last 10 years and next 5 years. *CES Transactions on Electrical Machines and Systems*, 1(2):91–99, 2017.

[73] I. Boldea and S. C. Agarlita. The active flux concept for motion-sensorless unified ac drives: A review. In *International Aegean Conference on Electrical Machines and Power Electronics and Electromotion, Joint Conference*, pages 1–16, Sept 2011.

[74] I. Boldea, M. C. Paicu, and G. D. Andreescu. Active flux concept for motion-sensorless unified ac drives. *IEEE Transactions on Power Electronics*, 23(5):2612–2618, Sept 2008.

[75] S. Rind, Y. Ren, and L. Jiang. Traction motors and speed estimation techniques for sensorless control of electric vehicles: A review. In *2014 49th International Universities Power Engineering Conference (UPEC)*, pages 1–6, Sept 2014.

[76] R. Bojoi, M. Pastorelli, J. Bottomley, P. Giangrande, and C. Gerada. Sensorless control of pm motor drives; a technology status review. In *2013 IEEE Workshop on Electrical Machines Design, Control and Diagnosis (WEMDCD)*, pages 168–182, March 2013.

[77] S. Chi, Z. Zhang, and L. Xu. Sliding-mode sensorless control of direct-drive pm synchronous motors for washing machine applications. *IEEE Transactions on Industry Applications*, 45(2):582–590, March 2009.

[78] S. Ichikawa, M. Tomita, S. Doki, and S. Okuma. Sensorless control of permanent-magnet synchronous motors using online parameter identification based on system identification theory. *IEEE Transactions on Industrial Electronics*, 53(2):363–372, April 2006.

[79] A. Yousefi-Talouki, P. Pescetto, G. Pellegrino, and I. Boldea. Combined active flux and high frequency injection methods for sensorless direct flux vector control of synchronous reluctance machines. *IEEE Transactions on Power Electronics*, PP(99):1–1, 2017.

[80] Y. Lee, Y. C. Kwon, and S. K. Sul. Comparison of rotor position estimation performance in fundamental-model-based sensorless control of pmsm. In *2015 IEEE Energy Conversion Congress and Exposition (ECCE)*, pages 5624–5633, Sept 2015.

[81] R. Kumar, S. Das, P. Syam, and A. K. Chattopadhyay. Review on model reference adaptive system for sensorless vector control of induction motor drives. *IET Electric Power Applications*, 9(7):496–511, 2015.

[82] D. Frick, A. Domahidi, M. Vukov, S. MariÃľthoz, M. Diehl, and M. Morari. Moving horizon estimation for induction motors. In *3rd IEEE International Symposium on Sensorless Control for Electrical Drives (SLED 2012)*, pages 1–6, Sept 2012.

[83] Peter Kuhl, Moritz Diehl, Tom Kraus, Johannes P. Schloder, and Hans Georg Bock. A real-time algorithm for moving horizon state and parameter estimation. *Computers and Chemical Engineering*, 35(1):71 – 83, 2011.

[84] Z. Guoqiang, W. Gaolin, N. Ronggang, and X. Dianguo. Active flux based full-order discrete-time sliding mode observer for position sensorless ipmsm drives. In *2014 17th International Conference on Electrical Machines and Systems (ICEMS)*, pages 3569–3572, Oct 2014.

[85] F. J. H. Kalluf, A. S. IsfÄČnuÅči, L. N. Tutelea, A. Moldovan-Popa, and I. Boldea. 1-kw 2000-4500 r/min ferrite pmsm drive: Comprehensive characterization and two sensorless control options. *IEEE Transactions on Industry Applications*, 52(5):3980–3989, Sept 2016.

[86] Yongchang Zhang and Jiali Liu. An improved q-pll to overcome the speed reversal problems in sensorless pmsm drive. In *2016 IEEE 8th International Power Electronics and Motion Control Conference (IPEMC-ECCE Asia)*, pages 1884–1888, May 2016.

[87] L. Saihi and A. Boutera. Robust sensorless sliding mode control of pmsm with mras and luenberger extended observer. In *2016 8th International Conference on Modelling, Identification and Control (ICMIC)*, pages 174–179, Nov 2016.

[88] X. Zhang, G. Tian, Y. Huang, and Z. Lu. A comparative study of pmsm sensorless control algorithms: Model based vs luenberger observer. In *2016 IEEE Vehicle Power and Propulsion Conference (VPPC)*, pages 1–6, Oct 2016.

[89] Christopher V. Rao, James B. Rawlings, and Jay H. Lee. Constrained linear state estimationâĂŤa moving horizon approach. *Automatica*, 37(10):1619 – 1628, 2001.

[90] Christopher V. Rao and James B. Rawlings. Constrained process monitoring: Moving-horizon approach. *AIChE Journal*, 48(1):97–109, 2002.

[91] Cheryl C. Qu and Juergen Hahn. Computation of arrival cost for moving horizon estimation via unscented kalman filtering. *Journal of Process Control*, 19(2):358 – 363, 2009.

[92] Stephen Boyd and Lieven Vandenberghe. *Convex Optimization*. Cambridge University Press, 2004.

# Derivation of the radial force density harmonics

In this Appendix, the derivation of the radial force density, acting on the stator, is presented. Firstly, the force density from the permanent magnets is treated followed by the contribution from the stator excitation. For this analysis, the Maxwell Stress Tensor is simplified accordingly,

$$
\begin{aligned}
f_n(\theta,t) &= \frac{1}{2\mu_0}\left[B_n(\theta,t)^2 - B_t(\theta,t)^2\right] && \text{(A.1)}\\
&\simeq \frac{1}{2\mu_0}B_n(\theta,t)^2 && \text{(A.2)}\\
&= \frac{1}{2\mu_0}\left(B_{nm}(\theta,t) + B_{ns}(\theta,t)\right)^2 && \text{(A.3)}
\end{aligned}
$$

where subscripts $n$ and $t$ indicates radial and tangential components and $m$ and $s$ indicates origin from permanent magnets or stator excitation, respectively. Three parts are obtained if the equation is further extended - Contributions from the stator and permanent magnets as well as the interaction from both. To calculate these, firstly the contribution from the permanent magnets is treated, followed by the contribution from the stator excitation and finalized with the contribution from the interaction of both.

## A.1 Force density originating from permanent magnets

The flux density originating from the permanent magnets can be expressed as [1, 2, 3],

$$B_n = \sum_u \sum_k B_{un} cos\left[up\omega_r t - (up \mp kN_s)\,\theta\right] \quad (A.4)$$

$$= \sum_u \sum_k B_{un} cos\left(u\alpha \pm k\beta\right) \quad (A.5)$$

where $u = 1, 3, 5, ...$ and $k = 0, 1, 2, ....$ $p$ and $N_s$ are the number of pole pairs and the number of stator slots, respectively. If the term $kN_s$ is neglected, both time and space harmonics are integer multipliers of the synchronous rotational speed of the rotor position. This is a result of the machine being a synchronous machine and differs from what is expected in, for example, an induction machine. The term $kN_s$ is due to the variable permeance which is a result of the stator slots, more thoroughly discussed in [1].

Limiting the summation to the three terms $[u, k] = [1, 0]\ [3, 1]\ [5, 2]$ gives

$$B_n \propto cos\left(\alpha\right) + cos\left(3\alpha \pm 1\beta\right) + cos\left(5\alpha \pm 2\beta\right). \quad (A.6)$$

From the simplified version of the Maxwell Stress Tensor, the radial force density is expressed as $f_n = \frac{1}{2\mu_0} B_n^2$ which is calculated as

$$\begin{aligned} f_n &\propto [cos(\alpha) + cos(3\alpha + \beta) + cos(3\alpha - \beta) \\ &+ cos(5\alpha + 2\beta) + cos(5\alpha - 2\beta)]^2 \\ &= cos(\alpha)^2 + cos(3\alpha + \beta)^2 + cos(3\alpha - \beta)^2 \cdots \\ &+ 2cos(\alpha)cos(3\alpha + \beta) + 2cos(\alpha)cos(3\alpha - \beta) \cdots \end{aligned}$$

Using the trigonometric equalities

$$cos(\alpha \pm \beta) = cos(\alpha + \beta) + cos(\alpha - \beta) \quad (A.7)$$

$$cos(\alpha)^2 = \frac{1 + cos(2\alpha)}{2} \quad (A.8)$$

gives the following rearranged expression

$$\begin{aligned} f_n &\propto 1.5 + \frac{1}{2}cos(2\alpha) + cos(6\alpha) + cos(10\alpha) \\ &+ cos(2\beta) + cos(4\beta) \\ &+ cos(-4\alpha \pm 2\beta) + 2cos(-2\alpha \pm \beta) + cos(-2\alpha \pm 3\beta) \\ &+ cos(4\alpha \pm \beta) + \frac{3}{2}cos(6\alpha \pm 2\beta) \\ &+ cos(8\alpha \pm \beta + cos(8\alpha \pm 3\beta) + \frac{1}{2}cos(10\alpha \pm 2\beta) \end{aligned}$$

which can be summarized in

$$\begin{aligned} f_n &\propto \sum_n \sum_l f_{nl} cos\left[2np\omega_r t - (2np \mp lN_s)\,\theta\right] \\ n, l &= 0, 1, 2, 3, ... \end{aligned} \tag{A.9}$$

where $\alpha$ and $\beta$ is changed to $p\omega_r t - p\theta$ and $lN_s\theta$, respectively. Note that the variables $n$ and $l$ is not functions of each other, which to some extent is the case for $B_n$. Worth noting is that the domain of $f_n$ for a particular sets of $n$ and $l$ is not in general strictly separated from any other set of $n$ and $l$, i.e. $P[f_n(n_1, l_1) \cap f_n(n_2, l_2)] \neq 0$ for some combinations as a result of the $\mp$-sign. This can be seen by studying the aforementioned equations noticing scaling factors of 2 and 3/2 appearing for some cosine-functions. Summarizing the expression, the following frequency and orders of the force density originating from the permanent magnets is obtained,

$$\left[2npf_1,\ -2np \pm lN_s\right]. \tag{A.10}$$

## A.2 Force density originating from the stator excitation

The derivation of the force density originating from the stator excitation itself starts with the excitation of the three phases. A perfectly sinusoidal excitation is assumed, expressed as

$$
\begin{aligned}
i_A &= \sqrt{2} i_1 cos(\omega t) \\
i_B &= \sqrt{2} i_1 cos(\omega t - \frac{2\pi}{3}) \\
i_C &= \sqrt{2} i_1 cos(\omega t - \frac{4\pi}{3}) \qquad \text{(A.11)} \\
& \qquad \text{(A.12)}
\end{aligned}
$$

where $\omega t$ is the electrical frequency.

The MMF of one phase is proportional to the current in that phase, as $F_A(\theta, t) \propto i_A$, and the MMF for the phases can be expressed as [1]

$$
\begin{aligned}
F_A &\propto \sum_v cos(\omega t) cos(v\theta) \\
&= \sum_v cos\left[(\omega t \mp v\theta) \pm 0(v \mp 1)\frac{2\pi}{3}\right] \\
F_B &\propto \sum_v cos(\omega t - \frac{2\pi}{3}) cos(vp\theta)) \\
&= \sum_v cos\left[(\omega t \mp v\theta) \pm 1(v \mp 1)\frac{2\pi}{3}\right] \\
F_C &\propto \sum_v cos(\omega t - \frac{4\pi}{3}) cos(vp\theta)) \\
&= \sum_v cos\left[(\omega t \mp v\theta) \pm 2(v \mp 1)\frac{2\pi}{3}\right] \qquad \text{(A.13)} \\
& \qquad \text{(A.14)}
\end{aligned}
$$

Considering the second term in the equation above, $(v \mp 1)\frac{2\pi}{3}$, for $v = 3, 9, 15, ...$ the resultant wave of the three phases equals zero. Expressing $v$ as $v = 3k = 3, 9, 15, ...$ the following holds

$$(v \mp 1)\frac{2\pi}{3} = (3k \mp 1)\frac{2\pi}{3} = 2\pi k \mp \frac{2\pi}{3} = 120^\circ \qquad \text{(A.15)}$$

which is summarized to zero for the three phases assuming that they are internally phase shifted 120°. For the harmonics $v = 6k \pm 1$, where $k = 1, 2, 3, ...$, the two cases that does not sum up to zero when the contribution from the three phases are summarized are

$$(6k+1-1)\frac{2\pi}{3} = 4k\pi = 0^\circ \tag{A.16}$$

$$(6k+1+1)\frac{2\pi}{3} = 2k\pi + 4\pi/3 = 240^\circ \tag{A.17}$$

$$(6k-1-1)\frac{2\pi}{3} = 4k\pi - 4\pi/3 = 120^\circ \tag{A.18}$$

$$(6k-1+1)\frac{2\pi}{3} = 2k\pi = 0^\circ \tag{A.19}$$

hence harmonics number 1,7,13,19,... rotates forward and 5,11,17,23,... rotates backwards [1]. The MMF for the $k^{th}$ phase can be simplified and expressed as

$$F_k \propto \sum_v cos\left[(\omega t \mp v\theta) \pm (k-1)(v \mp 1)\frac{2\pi}{3}\right]. \tag{A.20}$$

Equation (A.20) represents the MMF excited by the $k^{th}$ phase. The total MMF is the sum of all MMFs excited by each of the phases. Expanding (A.20), by the use of the trigonometric equality $cos(\alpha \pm \beta) = cos(\alpha)cos(\beta) \mp sin(\alpha)sin(\beta)$ the following is obtained

$$\begin{aligned} F_k \propto & \sum_v cos\left[(\omega t - v\theta) + (k-1)(v-1)\frac{2\pi}{3}\right] + \\ & \sum_v cos\left[(\omega t + v\theta) - (k-1)(v+1)\frac{2\pi}{3}\right] \\ = & \sum_v cos\left(\omega t - v\theta\right) cos\left((k-1)(v-1)\frac{2\pi}{3}\right) + \\ & \sum_v cos\left(\omega t + v\theta\right) cos\left((k-1)(v+1)\frac{2\pi}{3}\right) - \\ & \sum_v sin\left(\omega t - v\theta\right) sin\left((k-1)(v-1)\frac{2\pi}{3}\right) - \\ & \sum_v sin\left(\omega t + v\theta\right) sin\left((k-1)(v+1)\frac{2\pi}{3}\right). \end{aligned} \tag{A.21}$$

Summarizing all three phases, $F = \sum_{k=1,2,3} F_k$, the following is obtained

$$
\begin{aligned}
F \quad \propto \quad & \sum_v cos\left(p\omega t + v\theta\right) \times \\
& \left[1 + cos\left[(v-1)\frac{2\pi}{3}\right] + cos\left[2(v-1)\frac{2\pi}{3}\right]\right] + \\
& \sum_v cos\left(\omega t - v\theta\right) \times \\
& \left[1 + cos\left[(v+1)\frac{2\pi}{3}\right] + cos\left[2(v+1)\frac{2\pi}{3}\right]\right] - \\
& \sum_v sin\left(\omega t - v\theta\right) \times \\
& \left[0 + sin\left[(v-1)\frac{2\pi}{3}\right] + sin\left[2(v-1)\frac{2\pi}{3}\right]\right] + \\
& \sum_v sin\left(\omega t + v\theta\right) \times \\
& \left[0 + sin\left[(v+1)\frac{2\pi}{3}\right] + sin\left[2(v+1)\frac{2\pi}{3}\right]\right]. \qquad \text{(A.22)}
\end{aligned}
$$

With the use of the sum of trigonometric terms cosine and sine,

$$
\begin{aligned}
\sum_{k=0}^{n} cos(kx) &= \frac{cos\left(\frac{nx}{2}\right) sin\left(\frac{(n+1)x}{2}\right)}{sin\left(\frac{x}{2}\right)} \\
\sum_{k=0}^{n} sin(kx) &= \frac{sin\left(\frac{nx}{2}\right) sin\left(\frac{(n+1)x}{2}\right)}{sin\left(\frac{x}{2}\right)} \qquad \text{(A.23)} \\
& \qquad \text{(A.24)}
\end{aligned}
$$

the following simplification can be made,

$$
\begin{aligned}
& 1 + cos\left[(v \mp 1)\frac{2\pi}{3}\right] + cos\left[2(v \mp 1)\frac{2\pi}{3}\right] = \\
& \frac{sin\left((v \mp 1)\pi\right)}{sin\left(\frac{(v \mp 1)\pi}{3}\right)} cos\left(2\frac{(v \mp 1)2\pi}{3}\right) \qquad \text{(A.25)}
\end{aligned}
$$

$$
\begin{aligned}
& 0 + sin\left[(v \mp 1)\frac{2\pi}{3}\right] + sin\left[2(v \mp 1)\frac{2\pi}{3}\right] = \\
& \frac{sin\left((v \mp 1)\pi\right)}{sin\left(\frac{(v \mp 1)\pi}{3}\right)} sin\left(2\frac{(v \mp 1)2\pi}{3}\right) \qquad \text{(A.26)}
\end{aligned}
$$

Studying the cosine and sine terms in the end of the two expressions one clearly sees that

$$2\frac{(v\mp 1)2\pi}{3} = 2\frac{((6k\pm 1)\mp 1)2\pi}{3} = 4k\pi = 0^{\circ}, \tag{A.27}$$

hence the expression of the total MMF can be further simplified as

$$F \propto \sum_{v} \frac{sin\left((v\mp 1)\pi\right)}{sin\left(\frac{(v\mp 1)\pi}{3}\right)} cos(\omega t \mp v\theta) \tag{A.28}$$

$$= \sum_{v} K_{pv} cos(\omega t \mp v\theta) \tag{A.29}$$

where $K_{pv}$ is the so called band-factor [1] or phase-belt factor [2], expressed as

$$K_{pv} = \frac{sin\left((v\mp 1)\pi\right)}{sin\left(\frac{(v\mp 1)\pi}{3}\right)}. \tag{A.30}$$

The above expression is non-zero if and only if $v = 3m \pm 1$ where $m = 1, 2, 3, ...$, when it equals $K_{pv} = 3$. Lastly, the expression can once again be simplified to

$$F \propto \sum_{v=6m\pm 1} K_{pv} cos\left(\omega t \mp v\theta\right). \tag{A.31}$$

In order to consider stator slots, the permeance can be expressed as a cosine function with a periodicity defined by the an integer multiplier of the number of slots as [1]

$$\Lambda = \Lambda_{g0}\left[1 + \sum_{k=1,2,3} A_k cos(kN_s\theta)\right] \simeq \sum_{k=0,1,2} A cos(kN_s\theta). \tag{A.32}$$

The flux density is the MMF multiplied with the permeance. Using the simplified Maxwell Stress Tensor, the force density in radial direction can be written as

$$f \propto \left[\sum_{v,k} cos\left(p\omega t \mp v\theta \pm kN_s\theta\right)\right]^2. \tag{A.33}$$

However, neglecting the influence of the stator slots, the expression for the force density can be expressed as

$$f \propto \sum_{v=6m\pm1} \left[1 + cos\left(2\omega t \mp 2v\theta\right)\right]. \tag{A.34}$$

Note that this simplification only holds for harmonics of the same order [1]. The frequency and orders of the contribution from the stator alone can be summarized as

$$\left[2pf_1,\ 2vp\right]. \tag{A.35}$$

where $v = 1, 5, 7, 11, ...$, which is in alignment with [2]. In addition to the contributions from the same harmonics, space harmonics that are functions of the sum of different harmonics will also be present.

## A.3 Force density originating from interaction

The force density component from the interaction between the flux density from the permanent magnets and the stator excitation can be expressed as

$$f_n = \frac{1}{2\mu_0}\left(2B_{nm}B_{ns}\right) \tag{A.36}$$

motivating the following expression,

$$\begin{aligned} f_n \quad \propto \quad & \sum_u \sum_k cos\left[up\omega_r t - \left(up \mp kN_s\right)\theta\right] \times \\ & \sum_{v=3m\pm1} cos\left(p\omega_r t \mp vp\theta\right) \end{aligned} \tag{A.37}$$

where the two terms are discussed in the previous sections. The equation can be simplified as

$$f_n \propto \sum_v \sum_u \sum_k cos\left[(u \pm 1)p\omega_r t - \left(up \pm vp \pm kN_s\right)\theta\right] \tag{A.38}$$

where $v = 6m \pm 1$. Note that the sign $\pm$ occurs three times. If for example two components originating from the permanent magnets are interacting with one from the stator, this will generate in total 12 cosine functions. The two components from the permanent magnets, indexed $[u,\ k] = [1,\ 0]$ and $[3,\ 1]$, would interact with

for example the fundamental of the stator excitation, $v = 1$, yields the following simplified structure

$$[cos\,(a) + cos\,(a \pm b)]\,cos\,(c \mp d) \tag{A.39}$$

which in total can be expanded to 12 cosine function by using the trigonometric functions $cos(\alpha)cos(\beta) = 0.5cos(\alpha + \beta)cos(\alpha - \beta)$ and $cos(\alpha \pm \beta) = cos(\alpha + \beta) + cos(\alpha - \beta)$.

Consequently, the frequency and orders of the force density originating from this interaction can be summarized as

$$[(u \pm 1)pf_1,\ -(up \pm vp \pm kN_s)]\,. \tag{A.40}$$

which is in correlation with [2]. From the derivation of the flux density originating from the permanent magnets, $u = 2n \pm 1 = 0, 1, 3, 5, ....$ From the derivation of the contribution from the stator excitation, $v = 6m \pm 1$. For the frequency component, $u \pm 1$, only even integers will be present; $0, 2, 4, ....$ Hence the following substitution can be made, $u \pm 1 = 2n$, where $n = 0, 1, 2, ....$ The first part of the mode numbers, $-(up \pm vp)$, can be expressed as

$$-(up \pm vp) = -up \mp (6m \pm 1)p = 2np \mp 6mp. \tag{A.41}$$

Consequently, the expression for the frequency and orders can be expressed as

$$[2npf_1,\ -2np \pm 6mp \pm kN_s)]\,. \tag{A.42}$$

where $n, m, k = 0, 1, 2, ....$

# References

[1] Chong Wang Jacek F. Gieras and Joseph Cho Lai. *Noise of Polyphase Electric Motors*. CRC Press, 2005.

[2] Haodong Yang and Yangsheng Chen. Influence of radial force harmonics with low mode number on electromagnetic vibration of pmsm. *IEEE Transactions on Energy Conversion*, 29(1):38–45, March 2014.

[3] D. Zarko, D. Ban, and T.A. Lipo. Analytical calculation of magnetic field distribution in the slotted air gap of a surface permanent-magnet motor using complex relative air-gap permeance. *IEEE Transactions on Magnetics*, 42(7):1828–1837, July 2006.